The Astrophysical Journal Supplement Series, 258:8 (44pp), 2022 January https://doi.org/10.3847/1538-4365/ac2ee2

First Results on RR Lyrae Stars with the TESS Space Telescope: Untangling the Connections between Mode Content, Colors, and Distances

L. Molnár[1,2,3], A. Bódi[1,2,3], A. Pál[1,3,4], A. Bhardwaj[5], F–J. Hambsch[6,7], J. M. Benkő[1,2], A. Derekas[8,9,10], M. Ebadi[11], M. Joyce[12,13,14], A. Hasanzadeh[11], K. Kolenberg[15,16,17], M. B. Lund[18], J. M. Nemec[19], H. Netzel[1,2,20], C. –C. Ngeow[21], J. Pepper[22], E. Plachy[1,2], Z. Prudil[23], R. J. Siverd[24], M. Skarka[25,26], R. Smolec[20], Á. Sódor[1], S. Sylla[16,27], P. Szabó[1,2,28], R. Szabó[1,2,3], H. Kjeldsen[29,30], J. Christensen-Dalsgaard[29], and G. R. Ricker[4]

[1] Konkoly Observatory, Research Centre for Astronomy and Earth Sciences, Eötvös Loránd Research Network (ELKH), Konkoly Thege Miklós út 15–17, H-1121 Budapest, Hungary; lmolnar@konkoly.hu, lacalaca85@gmail.com
[2] MTA CSFK Lendület Near-Field Cosmology Research Group, 1121, Budapest, Konkoly Thege Miklós út 15-17, Hungary
[3] ELTE Eötvös Loránd University, Institute of Physics, 1117, Pázmány Péter sétány 1/A, Budapest, Hungary
[4] MIT Kavli Institute for Astrophysics and Space Research, 70 Vassar St., Cambridge, MA 02109, USA
[5] Korea Astronomy and Space Science Institute, Daedeokdae-ro 776, Yuseong-gu, Daejeon 34055, Republic of Korea
[6] Vereniging Voor Sterrenkunde (VVS), Oostmeers 122 C, B-8000 Brugge, Belgium
[7] Bundesdeutsche Arbeitsgemeinschaft für Veränderliche Sterne e.V. (BAV), Munsterdamm 90, D-12169 Berlin, Germany
[8] ELTE Eötvös Loránd University, Gothard Astrophysical Observatory, Szent Imre h.u. 112, 9700, Szombathely, Hungary
[9] MTA-ELTE Exoplanet Research Group, Szent Imre h.u. 112, 9700 Szombathely, Hungary
[10] Konkoly Observatory, Research Centre for Astronomy and Earth Sciences, Eötvös Loránd Research Network (ELKH), Konkoly Thege Miklós út 15–17, H-1121 Budapest, Hungary
[11] Institute of Geophysics, University of Tehran, Tehran, Iran
[12] Space Telescope Science Institute, 3700 San Martin Drive, Baltimore, MD 21218, USA
[13] Research School of Astronomy and Astrophysics, Australian National University, Canberra, ACT 2611, Australia
[14] ARC Centre of Excellence for All Sky Astrophysics in 3 Dimensions (ASTRO 3D), Australia
[15] Institute of Astronomy, KU Leuven, Celestijnenlaan 200D, B-3001 Heverlee, Belgium
[16] Physics Department, University of Antwerp, Groenenborgerlaan 171, B-2020 Antwerpen, Belgium
[17] Physics and Astronomy Department, Vrije Universiteit Brussel (VUB), Pleinlaan 2, 1050 Brussel, Belgium
[18] Caltech/IPAC, 1200 E. California Blvd., Pasadena, CA 91125, USA
[19] Department of Physics & Astronomy, Camosun College, Victoria, BC, Canada
[20] Nicolaus Copernicus Astronomical Center, Polish Academy of Sciences, Bartycka 18, PL-00-716 Warsaw, Poland
[21] Graduate Institute of Astronomy, National Central University, Jhongli 32001, Taiwan
[22] Department of Physics, Lehigh University, 16 Memorial Drive East, Bethlehem, PA 18015, USA
[23] Astronomisches Rechen-Institut, Zentrum für Astronomie der Univërsitat Heidelberg, Mönchhofstr. 12–14, D-69120 Heidelberg, Germany
[24] Gemini Observatory/NSF's NOIRLab, 670 N. A'ohoku Place, Hilo, HI, 96720, USA
[25] Department of Theoretical Physics and Astrophysics, Masaryk University, Kotlářská 2, 61137 Brno, Czech Republic
[26] Astronomical Institute, Czech Academy of Sciences, Fričova 298, 25165, Ondřejov, Czech Republic
[27] Universitè Cheikh Anta Diop Dakar-Fann, Senegal
[28] Magdalene College, University of Cambridge, CB3 0AG, Cambridge, UK
[29] Stellar Astrophysics Centre, Department of Physics and Astronomy, Aarhus University, Ny Munkegade 120, DK-8000 Aarhus C, Denmark
[30] Astronomical Observatory, Institute of Theoretical Physics and Astronomy, Vilnius University, Saulėtekio av. 3, 10257, Vilnius, Lithuania
Received 2021 June 19; revised 2021 September 14; accepted 2021 September 14; published 2021 December 22

Abstract

The Transiting Exoplanet Survey Satellite (TESS) space telescope is collecting continuous, high-precision optical photometry of stars throughout the sky, including thousands of RR Lyrae stars. In this paper, we present results for an initial sample of 118 nearby RR Lyrae stars observed in TESS Sectors 1 and 2. We use differential image photometry to generate light curves and analyze their mode content and modulation properties. We combine accurate light-curve parameters from TESS with parallax and color information from the Gaia mission to create a comprehensive classification scheme. We build a clean sample, preserving RR Lyrae stars with unusual light-curve shapes, while separating other types of pulsating stars. We find that a large fraction of RR Lyrae stars exhibit various low-amplitude modes, but the distribution of those modes is markedly different from those of the bulge stars. This suggests that differences in physical parameters have an observable effect on the excitation of extra modes, potentially offering a way to uncover the origins of these signals. However, mode identification is hindered by uncertainties when identifying the true pulsation frequencies of the extra modes. We compare mode amplitude ratios in classical double-mode stars to stars with extra modes at low amplitudes and find that they separate into two distinct groups. Finally, we find a high percentage of modulated stars among the fundamental mode pulsators, but also find that at least 28% of them do not exhibit modulation, confirming that a significant fraction of stars lack the Blazhko effect.

Unified Astronomy Thesaurus concepts: Pulsating variable stars (1307); RR Lyrae variable stars (1410); Stellar photometry (1620)

Supporting material: machine-readable tables

1. Introduction

RR Lyrae variable stars are old, low-mass stars in the core He-burning phase and thus they occupy the horizontal branch of the Hertzsprung–Russell diagram. They pulsate radially with

large amplitudes and short periods (typically between 0.25–1.0 days). They can be found in large numbers throughout the Milky Way, in the bulge, thick disk, halo, globular clusters, and in various dwarf galaxies and stellar streams in and around our Galaxy.

The study of RR Lyrae stars began over a century ago (Kapteyn 1890; Bailey 1902; Pickering 1901). Initially, they were considered a homogeneous group of bright variable stars that are abundant in the Milky Way and found to be useful as distance and population indicators. However, as Preston (1964) remarked in his review of the group, intriguing differences soon emerged. These included the Oosterhoff dichotomy, which separates the stars (or, at first, the globular clusters they populate) into two groups in the period–amplitude plane (Oosterhoff 1939). The dichotomy has since been explained through detailed evolutionary calculations and spectroscopic measurements of metal-rich and metal-poor RR Lyrae stars that reside in various clusters and other structures in the Milky Way (see, e.g., Sollima et al. 2014; Fabrizio et al. 2019; Prudil et al. 2019).

Short-period pulsators, below 0.2 days, were recognized to be different types of stars, today known as δ Sct and SX Phe variables (Smith 1955; Woltjer 1956). The long variations observed in some stars, first described by Blažko (1907), were proving difficult to explain, especially the 41 day variation in the star RR Lyr itself. This slow modulation of the pulsation is known today as the Blazhko effect, named after its discoverer. Later, the first double-mode stars were identified and used to constrain the masses of RR Lyrae stars (Cox et al. 1980).

With increasing computing power, pulsation models improved (see, e.g., Bono & Stellingwerf 1994; Kolláth et al. 2002), and large-scale and/or dedicated surveys were initiated (Minniti et al. 1999; Soszynski et al. 2003; Jurcsik et al. 2009). The newest generation of large photometric, astrometric, and spectroscopic surveys massively expanded the number of known, observed, and classified RR Lyrae stars, which now measures in the hundreds of thousands (Sesar et al. 2017; Holl et al. 2018; Clementini et al. 2019; Soszyński et al. 2019; Liu et al. 2020). Mining these large data sets led to new discoveries in numerous areas, from the structure and collisional history of the Miky Way (Moretti et al. 2014; Hernitschek et al. 2017; Iorio & Belokurov 2019; Prudil et al. 2021) to chemical evolution (Crestani et al. 2021a) to the detection of shock waves and associated emission lines in overtone and double-mode stars (Duan et al. 2021a, 2021b).

While great advances were made, some aspects of RR Lyrae stars have still remained poorly understood. Despite numerous hypotheses, the Blazhko effect has not been explained satisfactorily. Mass determinations remained controversial thanks to uncertainties in the pulsation models and the nearly complete lack of confirmed RR Lyrae binaries (Hajdu et al. 2015; Liška et al. 2016; Skarka et al. 2018). Long-term photometric and spectroscopic monitoring and high-precision astrometry have recently begun to also reveal RR Lyrae stars with companions (Sódor et al. 2017; Kervella et al. 2019a; Barnes et al. 2021; Hajdu et al. 2021), but the first candidate RR Lyrae-type variable in an eclipsing binary system for which mass could be determined was ultimately identified as a low-mass binary pulsator rather than a bona fide RR Lyrae star (Pietrzyński et al. 2012).

Upon entering the era of photometric space missions, the very first observation of the prototype double-mode star, AQ Leo, with the MOST space telescope delivered the first discovery of low-amplitude additional modes in RR Lyrae stars (Gruberbauer et al. 2007). The CoRoT and Kepler light curves showed how diverse the appearances of the Blazhko effect can be, with a multitude of varying and multiperiodic modulations detected (Guggenberger et al. 2011, 2012; Benkő et al. 2014). These observations revealed further dynamical effects in the pulsation, including period doubling (PD) of the fundamental mode and various additional modes in many stars (Chadid et al. 2010; Szabó et al. 2010, 2014).

One drawback of the Kepler and K2 observations, however, is that nearly all of the observed stars (1) were pre-selected based on earlier observations and surveys, (2) were limited to small areas on the sky, and (3) were mostly faint and distant targets (Howell et al. 2014; Borucki 2016). While this made it possible to reach the edge of the Galactic halo and nearby dwarf galaxies, it also meant that spectroscopic follow-up and the calibration of the photometric [Fe/H] relation for the Kepler passband required the largest ground-based telescopes (Nemec et al. 2013; Molnár et al. 2015a).

In contrast, the Transiting Exoplanet Survey Satellite (TESS) space telescope follows a different strategy (Ricker et al. 2015). It uses four small cameras that provide an enormous, $24° \times 96°$ field of view at the cost of lower resolution and depth than those of Kepler. Benefits and limitations of TESS concerning RR Lyrae and Cepheid stars were summarized by Plachy (2020). Briefly, the observing strategy of the mission will cover nearly the entire sky, including the brightest RR Lyrae stars. This will make it possible to combine the detailed photometric analysis with extensive spectroscopic observations and precise geometric parallax and proper motion data from the European Gaia mission (Gaia Collaboration et al. 2016). We expect the faint limit of TESS to be around 16–17 mag, depending on the crowding and the required level of precision. The number density of RR Lyrae stars within the Galaxy peaks around this brightness, although most of them are fainter (Plachy 2020). Nevertheless, we expect that TESS will be able to characterize a few tens of thousands of stars with varying degrees of accuracy.

TESS confers the ability to characterize the short-term variability of a large sample of nearby RR Lyrae stars, including precise light-curve shape, (sub)millimagnitude-level additional modes, and short-period modulations. Furthermore, the densely sampled light curves allow us to test classifications based on sparse photometry and to create a cleaner sample of nearby RR Lyrae stars, which can in turn be used to construct a more precise period–luminosity (PL) relation when combined with Gaia parallaxes. Precise PL (and period–luminosity–metallicity) relations can then be used as a separate distance scale anchor that relies on Population II stars (Beaton et al. 2016; Neeley et al. 2019).

This paper presents the first results obtained for RR Lyrae stars with TESS. A companion paper details the first results on various Cepheid-type stars (Plachy et al. 2021). The paper is structured as follows: we describe our photometry method in Section 2. Results, including classification, detailed light-curve analysis, and mode contents, are described in Section 3. We compare our first results to ground-based photometry and pulsation models in Section 4. Finally, we discuss the future prospects of RR Lyrae research with TESS and draw our conclusions in Sections 5 and 6.

2. Data and Methods

Data used in this paper come from the TESS and Gaia space missions. We introduced TESS in the preceding section and present the data reduction step below. The other source, the Gaia

mission, is collecting high-precision astrometric and sparse photometric observations throughout the entire sky (Gaia Collaboration et al. 2016). Processed Gaia data are released in batches: the most recent one, Early Data Release 3, contains astrometry and three-band average photometry for over 1.8 billion stars (Gaia Collaboration et al. 2021). The previous release, DR2, also included, among other products, radial velocity (RV) measurements and variable candidate classifications (Gaia Collaboration et al. 2018a).

2.1. TESS Observations

TESS observations are separated into so-called *sectors*. During each sector, the spacecraft pointing is kept constant with respect to the celestial reference frame. Each sector is made up from two consecutive *orbits* when the spacecraft orbits Earth with a period of half of one sidereal month ($P_{\rm TESS} \approx 13.7$ days). Observations are gathered continuously for one orbit, and the collected data are downloaded at perigee. Sectors 1 and 2 lasted for 27.9 and 27.4 days, with 1.13 and 1.44 day long mid-sector gaps, respectively. During each sector, the entire field of view is recorded as full-frame images (FFI) at a 30 minute cadence, while selected targets are measured with 2 minute cadence.

As TESS is orbiting Earth, it is affected by scattered or direct light entering the cameras both from Earth and the Moon. Most of Sector 1 was affected by diffuse light from Earth that was modulated by the planet's rotation. Glinting from the Moon affected the last few cadences in Camera 1. Mars was outside but close to the field of view of Camera 1, and so it also affected some observations in Sector 1. Moreover, a 2 day long segment was affected by excess jitter in the spacecraft pointing[31].

Sector 2 was much less eventful, with scattered light from Earth only entering the cameras toward the ends of each orbit. Scattered light manifests itself as a large, diffuse, slow-moving patch of excess light over the background in the images, raising the local background level.

2.2. Targets and Data Reduction

In Sectors 1 and 2, three targets were observed as 2 minute cadence targets, part of the TESS Asteroseismic Science Consortium (TASC) target list (ST Pic in both sectors, BV Aqr in S1, and RU Scl in S2). The rest of the RR Lyrae stars were FFI targets. We searched the SIMBAD database and the Gaia DR2 variable star candidate catalogs of Clementini et al. (2019) and Holl et al. (2018) for RR Lyrae stars. We limited the sample to stars brighter than approximately 12.5 mag in the TESS passband for Cameras 1–3 and brighter than 14.0 mag in Camera 4. We discarded a few targets that showed severe instrumental noise and/or contamination in their light curves.

2.2.1. 2 minute Targets

TESS 2 minute cadence targets are observed in dedicated postage-stamp images and both the corrected target pixel files and reduced light curves are released by the Science Processing Operations Center (SPOC). The same target pixel files have been reduced by TASOC (TESS Asteroseismic Science Operations Center[32]) as well. However, their initial release utilized an older pipeline that was developed for solar-like oscillators observed by the Kepler mission and hence does not handle large-amplitude variables well. We investigated both sets of light curves and decided to create our own photometry based on custom pixel apertures with the LIGHTKURVE tool, and, in particular, its interactive pixel selection option (Barentsen et al. 2019). This approach provided full control over selecting the pixel apertures, and yielded good-quality light curves for use in the frequency analysis.

2.2.2. Full-frame Image Targets

We processed the FFI targets with the FITSH software package (Pál 2012). The description here is largely identical to that in the Cepheid first light paper (Plachy et al. 2021), and the same method has been employed in other works as well (e.g., Borkovits et al. 2020; Szegedi-Elek et al. 2020; Merc et al. 2021; Nagy et al. 2021; Ripepi et al. 2021; Szabó et al. 2021).

The data reduction process has been split into two distinct procedures in our pipeline. First, we compute the plate solution for the calibrated FFIs, and we perform astrometric cross-matching using the Gaia DR2 catalog as well as various tasks (`fistar`, `grmatch`, `grtrans`) of the FITSH package. In this step, we also derive the flux zero-point. This is calculated with respect to the Gaia $G_{\rm RP}$ magnitudes as the throughput of TESS (see Figure 1 in Ricker et al. 2015) is very similar to the $G_{\rm RP}$ passband of the Gaia photometric system (see Figure 3 in Jordi et al. 2010). This flux zero-point level is obtained for various TESS fields from Sector 1 and Sector 2. We find an rms residual of 0.015 mag, which indicates high accuracy.

We note that the plate solution model applied in this work is more sophisticated than what the WCS-related FITS keywords would enable. Namely, besides the application of the gnomonic (tangential) projection, we apply a third-order Brown–Conrady model (Brown 1971) with respect to the optical axis of the images (which do not fall on silicon due to the focal plane design of the TESS cameras). A third-order polynomial correction is then applied afterward in order to account for all other optical aberrations and the differential velocity aberration throughout a sector.

The steps described above are performed completely independently for all calibrated full-frame images for each of 4 CCD units in each of 4 cameras. The total number of available cadences was 1282 and 1245 for TESS Sectors 1 and 2, respectively, while 15 and 17 frames were flagged as low-quality ones due to the presence of TESS reaction wheel momentum dumps, respectively.

In the second step, we cut out small images centered on the target stars and perform differential image analysis only on those sub-frames, as shown in Figure 1. With the astrometric solution at hand, we can simply query for the presence of any given object at any given instance. Any type of differential image analysis requires a reference frame, from which the deviations of the individual images are (expected to be) minimal and which itself has a good signal-to-noise ratio. In our analysis, we use the median average of 9 or 11 individual subsequent sub-frames with a size of 64×64 pixels to create this reference frame. The individual frames were selected around the mid-times of the observation series (i.e., at the very end of the first orbit or at the very beginning of the second orbit) in order to minimize the differential velocity aberration and also at a point when Earth was below the horizon of TESS.

[31] TESS Data Release Notes are available at https://archive.stsci.edu/tess/tess_drn.html.
[32] https://tasoc.dk

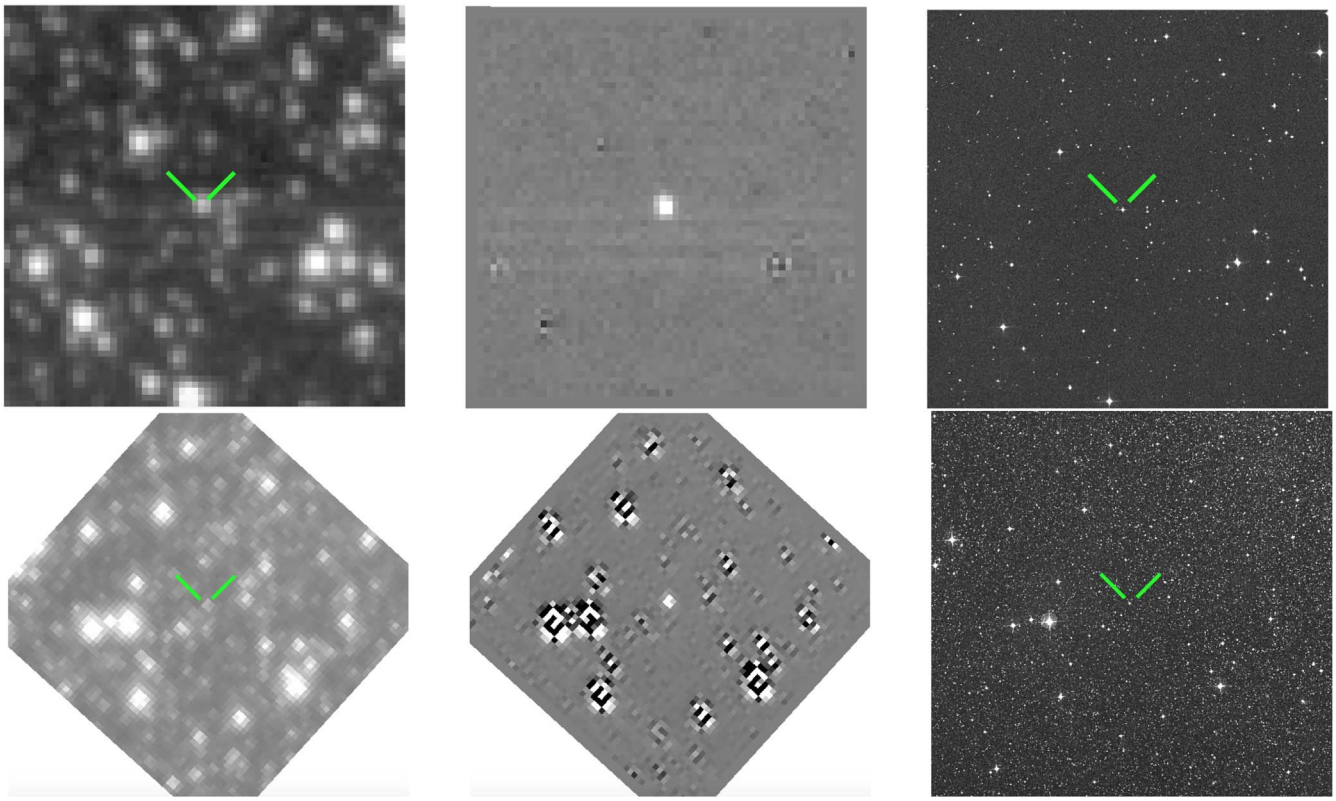

Figure 1. Images of two RR Lyrae stars, marked with green lines in the images. Upper panels: RV Hor, a star located in a relatively sparse stellar field. Bottom panels: OGLE–LMC–RRLYR–23457, at the outskirts of the LMC. Left panels: a single TESS cadence from Sector 1. Middle panels: a single differential frame. The images of RV Hor are affected by reflections from the stripes of CCD electronics but otherwise almost entirely clean. The LMC image shows many residuals after image subtraction but the variable is clearly visible in the center. Right panels: corresponding DSS images. All images are oriented to celestial directions (north is up; east is to the left). The TESS cutouts are 64 × 64 px or $22\farcm4 \times 22\farcm4$ large.

We can then use the reference frame to obtain both the image convolution coefficients and a set of reference fluxes (using the FITSH task `fiphot`, and see Pál 2009, 2012). Image convolution can correct many of the instrumental and/or intrinsic differences between the target frames and the reference frame, including the slight drift caused by the differential velocity aberration, spacecraft jitter, and background and stray light variations. In addition, convolution can help to eliminate or significantly decrease the effects caused by the momentum wheel dumps. We then determine the differential flux values on the convolved and subtracted images by simple aperture photometry. Two examples for the effectiveness of image subtraction are shown in Figure 1, one for a sparse stellar field and one at the outskirts of the LMC.

Since reference fluxes are hard to accurately obtain even for moderately confused stellar fields with TESS (due to the large pixel size of $21''\,\mathrm{px}^{-1}$), we instead elected to use the Gaia GDR2 G_{RP} (`phot_rp_mean_mag`) magnitudes of the targets. We note that the Gaia EDR3 definitions of the Gaia passbands are slightly different from the DR2 ones, but differences are minimal, in most cases below 0.05 mag (Gaia Collaboration et al. 2021; Riello et al. 2021). The final fluxes (i.e., the sums of the reference fluxes and the respective differential fluxes) still needed to be adjusted, as the reference frame we subtract is not averaged out over the variation of the star but rather contains a prior unknown segment of the light curve only. At the final step, we rescaled the average flux and associated errors to the G_{RP} value. For targets observed in both sectors, we also applied further corrections (10^{-3}–10^{-2} relative flux level shifts and percent-level scalings) when necessary in order to stitch the light-curve segments together. A sample of the data file containing measurements of all FFI targets is shown in the Appendix.

The light curves were then analyzed by several co-authors separately, using predominantly the PERIOD04 software (Lenz & Breger 2005) to identify pulsation periods, harmonics, and various other frequency components in the data. Temporal variations in the Fourier amplitudes and phases were also investigated.

2.3. Comparison with ELEANOR Photometry

The ELEANOR open-source software tool was developed by Feinstein et al. (2019) to produce light curves from the TESS FFI data. The software is capable of doing pixel aperture and PSF photometry and decorrelating systematics and co-trending signals from the light curves. We tested the performance of ELEANOR on a small selection of RR Lyrae stars. Classical correction methods, such as regressing the photometry against position changes, are difficult to apply to RR Lyrae stars since the high amplitude and rapidly changing signal often overwhelms the comparatively smaller systematics. We found that the simple pixel-photometry light curves, corrected for pixel-position-related changes (the CORR_FLUX photometry), are of inferior quality compared to our results, as shown in Figure 2. This result was not unexpected as multiple correction methods developed for general use in the K2 mission fared even worse when applied to RR Lyrae stars (Plachy et al. 2019).

In contrast, the PSF photometry produced by ELEANOR, which fits a two-dimensional Gaussian function as a PSF model to each frame, usually resulted in light curves that matched the

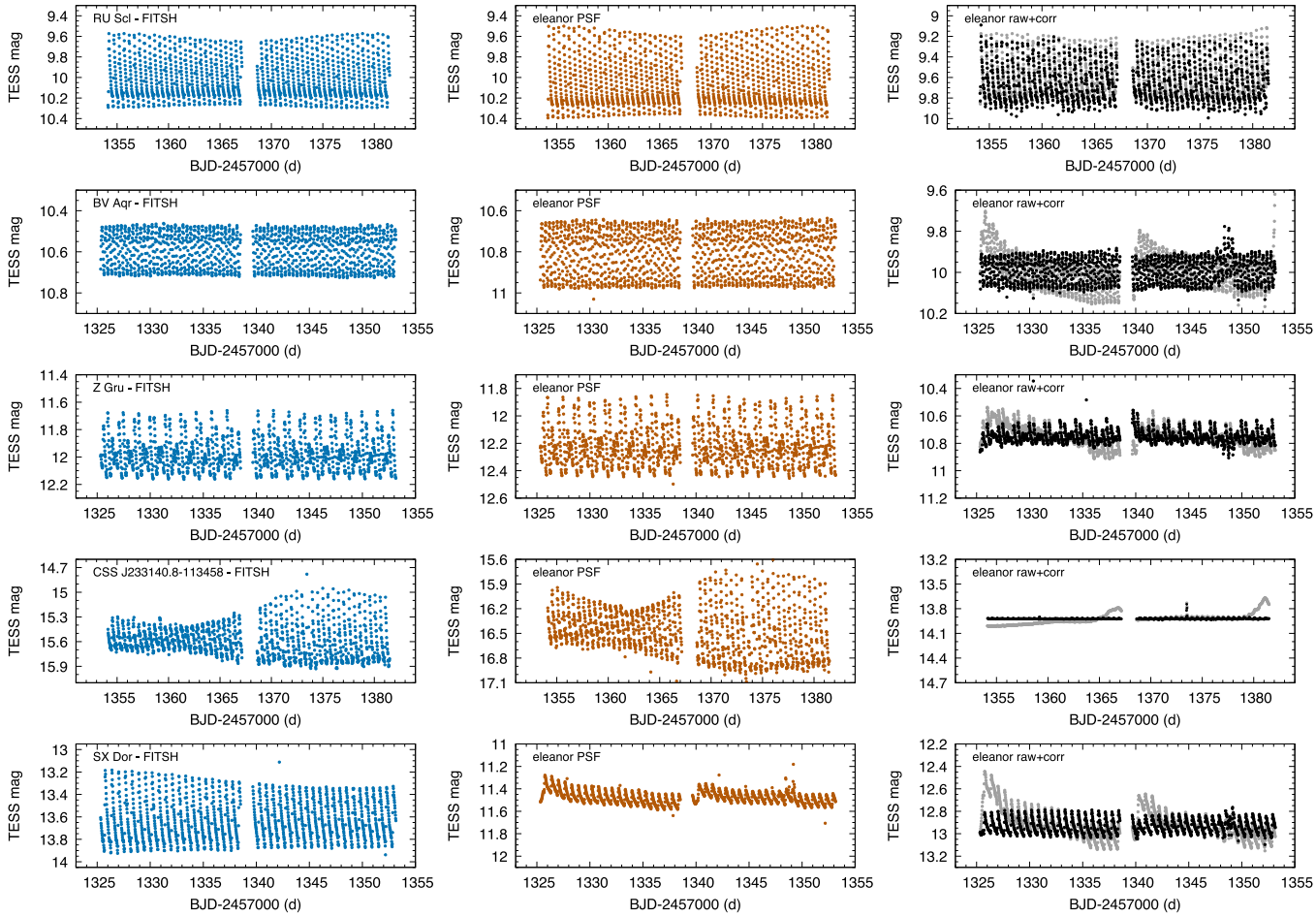

Figure 2. Comparison of the FITSH differential-imaging aperture photometry (left row) with the ELEANOR photometries. Center: PSF fitting. Right: raw (gray) and corrected (black) pixel aperture photometry. From top to bottom, three relatively bright stars from each subclass (RRab, RRc, RRd) and a faint RR Lyrae star, SX Dor, from a crowded region near the Large Magellanic Cloud (LMC). Plots are on the same scale in each row.

quality of our data. This was true even for faint targets—down to 16 mag stars—as long as the star was well separated. One example is CSS J233140.8–113458, shown in the fourth row of Figure 2. Blending and nearby stars, however, can confuse the algorithm and may result in a poor light curve: this happened to SX Dor, which is in front of the outskirts of the LMC (last row of Figure 2). We concluded that limiting the size of the image cut-out to exclude other sources can be beneficial but the code requires a minimum size of 9×9 px image for a reliable fit. We also observed differences between the average brightness and pulsation amplitude values produced by ELEANOR and our code: the ELEANOR light curves are usually, but not always, fainter by up to 0.3 mag, or 33% in mean flux. Lower mean flux suggests that the background level may be overestimated in the PSF photometry. This again highlights the difficulties caused by crowding and blending in the TESS images.

3. Results

In this section we present various results obtained from the TESS light curves and Gaia measurements. First we study the kinematics of the targets, and classify the stars based on their absolute brightness, color, and light-curve shape information to create a clean RR Lyrae sample. We then study how accurately can we identify the Blazhko effect in the relatively short TESS light curves. We also evaluate the mode content of each light curve and compare those results to earlier findings.

3.1. Kinematics

We searched for available radial velocities (RVs) for the selected RR Lyrae stars and found data for 57 targets in Gaia EDR3, in the Radial Velocity Experiment (RAVE; Steinmetz et al. 2020), in the Galactic Archaeology with HERMES Survey (GALAH DR3; Buder et al. 2021), and in the observations by Layden (1994). The Gaia, GALAH, and RAVE surveys do not take into account stellar pulsation in their radial velocity measurements, hence their values can be off by up to $\approx$75 km s^{-1} based on Equation (1) in Liu (1991) and a projection factor of 1.37 (the ratio between intrinsic pulsation velocities and disk-averaged RVs; value from Sesar 2012). However, RVs derived by Layden (1994) take into account stellar pulsation and they report errors of order 15 km s^{-1}. Multiple stars in our sample have RVs both in the Gaia EDR3 and in the Layden (1994) catalogs and the difference between the two ranges from 10 to 30 km s^{-1}. Therefore, we assumed a conservative error of 75 km s^{-1} on the Gaia, GALAH, and RAVE RVs. We did not attempt to phase RV values for stars that are present in multiple databases; although this could, in principle, help us to determine the systemic velocity of the star more accurately, the phasing of multiple RV measurements may not be a trivial task. The

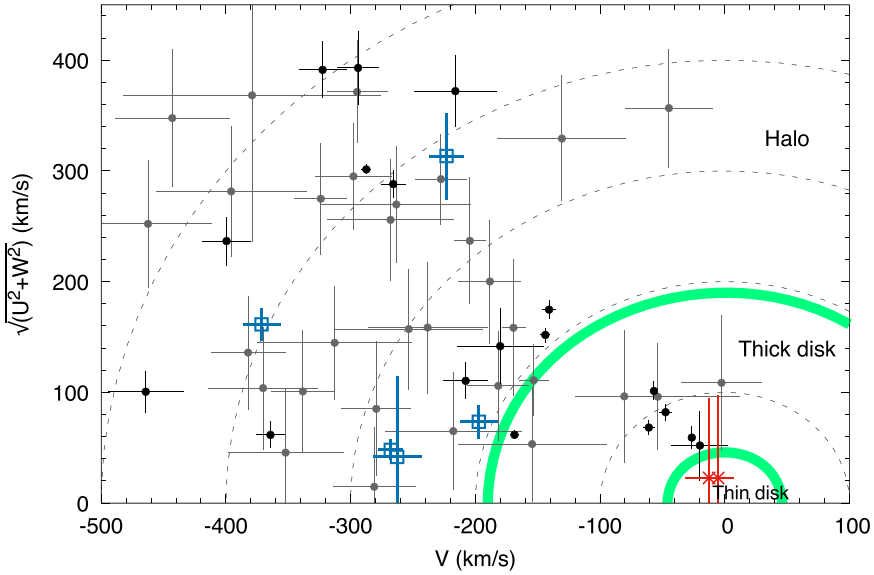

Figure 3. Toomre diagram of 42 stars from our sample. Black dots are halo RR Lyrae stars; blue squares are variables that may be members of Gaia–Enceladus structure according to Prudil et al. (2020). Dashed lines mark constant total space velocities while green lines show the approximate thin–thick disk and disk–halo boundaries. The red crosses are two non-pulsating stars we identify in Section 3.2.

alignment of these data would be affected not only by unknown phase shifts and possible modulation present in the pulsation, but also by the fact that different surveys use different spectral lines that sample regions with different kinematics in the atmosphere (Braga et al. 2021). Further, some databases do not provide precise times of measurement.

We used the GAIADR3_ZERO-POINT software to correct for the zero-point offset present in the Gaia EDR3 parallaxes (Lindegren et al. 2021a, 2021b). We note that almost all RVs in Gaia DR2 are propagated into EDR3 unchanged, with the exception of the most discrepant values in DR2, which were removed from the new catalog (Soubiran et al. 2018).

We then computed the full 6D orbital solution of the stars using the Gaia EDR3 proper motions and parallaxes in concert with collected RVs using the GALPY library (Bovy 2015). The whole calculation was performed through a Monte Carlo error analysis varying the proper motions, parallaxes, and RVs within their errors. Uncertainties and covariances among all parameters were taken into account in calculating the velocity uncertainties. The final values and their errors were taken as the medians and absolute median deviations from the generated distributions. We corrected for solar motion with respect to the local standard of rest with the velocities $(U_\odot, V_\odot, W_\odot) = (11.1, 12.24, 7.25)$ km s^{-1}, where the U component is defined pointing toward the anticenter direction (Schönrich et al. 2010; Schönrich 2012). We used $z_\odot = 20.8 \pm 0.3$ pc and $r_\odot = 8.122 \pm 0.031$ kpc for the solar position above the plane and the distance to the Galactic center, respectively (Bennett & Bovy 2019; Gravity Collaboration et al. 2018). The resulting velocity components U, V, and W are the rectangular heliocentric velocity components.

Stars spread out in Figure 3 which effectively shows orbital energy and angular momentum compared to the local standard of rest. Stars with high total velocities, above 180–200 km s^{-1} are halo members. Stars with velocities below that are part of the disk, with the thin–thick boundary being at around 46 km s^{-1} (Bensby et al. 2003; Buder et al. 2019). While most of the stars in the sample are either part of the halo or the thick disk, two objects, marked red, are close to zero, i.e., they clearly belong to the thin disk and follow galactic orbits similar to that of the Sun. We later show that these stars are in fact not pulsating stars.

We cross matched our list of objects with the 314 objects studied by Prudil et al. (2020). Since Sectors 1–2 are far from the Galactic Plane, we found no objects that were identified as possible thin-disk RR Lyrae stars. However, four of our targets (UW Gru, VW Scl, YY Tuc, and XZ Mic) are potentially members of the Gaia–Enceladus structure, also known as the Gaia Sausage, the remnant of a galaxy merged into the Milky Way (Helmi et al. 2018). This sample is currently too small to analyze separately but highlights the fact that we will be able to use TESS to study different RR Lyrae populations.

3.2. Classification

The stars selected for this study have been classified as RR Lyrae at least once already by prior studies. However, these classifications are sometimes based on observations of limited quality and/or quantity. We therefore verified the classifications based on the TESS light curves, complemented by Gaia EDR3 brightness and parallax data (Gaia Collaboration et al. 2021).

3.2.1. Absolute Magnitudes and Distances

We computed the absolute magnitudes in the Gaia EDR3 G, $G_{\rm BP}$, and $G_{\rm RP}$ bands using the geometric Gaia EDR3 distances calculated by Bailer-Jones et al. (2021), and correcting for extinction with the MWDUST code (Bovy et al. 2016). We used the combined maps created by Bovy et al. (2016). This method provided good separation between the intrinsically fainter rotational variables and binaries and the brighter, evolved HB stars where we expect RR Lyrae variables to appear. The calculated absolute brightness values are plotted in Figure 4 along with the distribution of the absorption coefficients in the sky. We also calculated absolute magnitudes in the V, J, H, and K bands, based on the brightness values listed in the SIMBAD database for each star (Wenger et al. 2000). Geometric Gaia distances for RR Lyrae stars have been verified previously for the DR2 data by Hernitschek et al. (2019). They found that

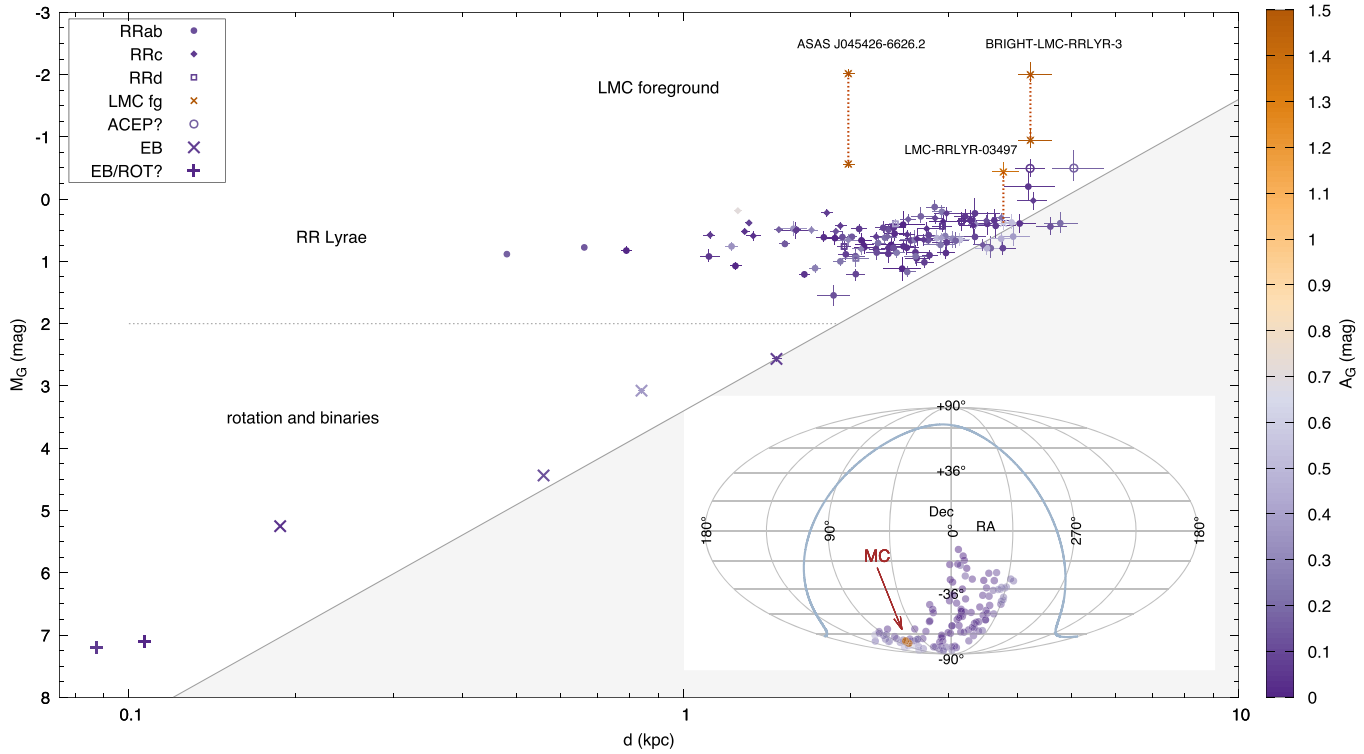

Figure 4. Main: the Gaia EDR3 M_G absolute magnitudes and distances of the sample, color-coded with the A_G absorption coefficients calculated with MWDUST. The diagonal line and light-gray area below it mark the approximate brightness cut of the sample. Large crosses mark eclipsing stars that we were able to classify based on light-curve shapes. The large pluses at the bottom are two stars where the light-curve shape was not decisive but their positions clearly rule them out. Different extinction corrections for the three LMC foreground stars are connected with the dashed lines. Insert: map of the targets with and the A_G absorption coefficients in the EDR3 G band. The position of the Magellanic Clouds is marked with the arrow.

they are accurate to about 5 kpc, but lose accuracy beyond about 10 kpc, at which point they become dominated by the distance prior used by Bailer-Jones et al. (2018). We can therefore expect the EDR3 distances for our sample, which only extends to 5 kpc, to be accurate as well.

The M_G brightness of most of the stars is between 1.5 and 0.0 mag, where we expect horizontal branch stars to cluster (Gaia Collaboration et al. 2018b). Six stars fall clearly below this range. The variations of the two faintest (marked with blue plus signs), ASAS J212045–5649.2 and ASAS J225559–2709.9, look superficially like RR Lyrae-type pulsation: these are likely rotational and/or ellipsoidal variables. Four more are cataloged as RR Lyrae stars but the TESS light curves make it clear that these are eclipsing binaries (blue cross signs). These are, in decreasing absolute brightness: CRTS J215543.7-500050, AZ Pic, UW Dor, and UY Scl. We note that UY Scl has been listed previously as a possible binary RR Lyrae based on its large proper motion anomaly in DR2 (Kervella et al. 2019b). We calculated velocity components for two of these six targets in Section 3.1. ASAS J212045–5649.2 and UY Scl are the two red crosses in Figure 3, closest to zero, indicating that they are part of the thin disk.

Three other stars stand out due to high absorption coefficient values ($A_G = 1.4$, 2.6 and 3.0 mag, for OGLE LMC–RRLYR–03497 (also known as SW Dor), OGLE BRIGHT–LMC–RRLYR–3 and ASAS J045426–6626.2, respectively): all three lie in the direction of the LMC, as the sky map in Figure 4 indicates. OGLE BRIGHT–LMC–RRLYR–3 was newly identified in the OGLE–III LMC Shallow Survey as a Galactic RR Lyrae: it is known as OGLE LMC–RRLYR–28980 in their main catalog (Ulaczyk et al. 2013). Since all three stars are clearly nearby stars that are in the foreground of the LMC, these extinction corrections appear to be excessive. To test this we then calculated the interstellar absorption using the SFD dust maps instead (Schlafly & Finkbeiner 2011): for these three stars the SFD map gave about 0.7–1.5 mag smaller absorption but two of the three still remained overluminuos.

3.2.2. Period–Luminosity Relations and Colors

With the pulsation periods from the TESS light curves in hand, we created the period–luminosity plot of our TESS first light sample in M_G and M_K bands, as shown in the left panels of Figure 5. With this sample size the slopes of the PL relations are not entirely apparent, especially for the RRc stars, but the increase in brightness with the period can be seen. K-band brightness is much less sensitive to interstellar extinction than shorter wavelengths, limiting the spread of the PL relation, although for RR Lyrae stars the spread of the PL relation is largely driven by metallicity (Catelan et al. 2004; Layden et al. 2019; Bhardwaj et al. 2021; Gilligan et al. 2021). Furthermore, not all stars have their K brightness measured (here, 32 of the 118 targets are missing from the lower plots), and even when they do, single-epoch measurements may not represent mean brightness values.

For RRd stars both of their periods are indicated by the black empty squares. Two of the three overcorrected stars, ASAS J045426–6626.2 and BRIGHT–LMC–RRLYR–3, stand out with either correction methods, but the third, LMC–RRLYR–03497, moves into the RRab locus with the lower, SFD-based correction.

We also calculated the extinction-corrected EDR3 $G_{\rm BP} - G_{\rm RP}$ and $J - K$ colors for every star. In the color–magnitude diagrams (CMDs, right panels of Figure 5) the three stars that are in front of the LMC are clearly shifted blueward (black crosses), confirming that they are overcorrected for interstellar extinction. Tracing them

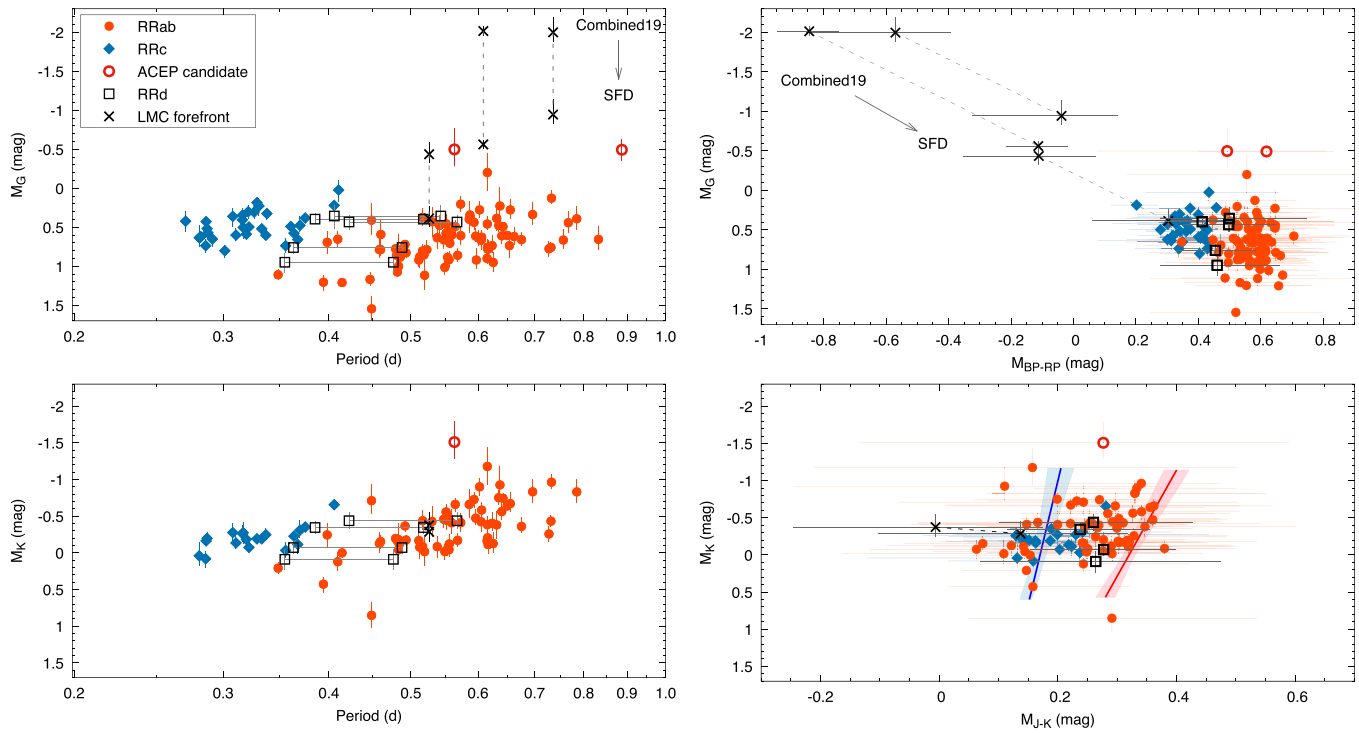

Figure 5. Left: period–luminosity relation of the sample. Brightness is in M_G (top) and M_K (bottom) absolute magnitudes. RRab and RRc stars are represented with blue diamonds and red dots, respectively. For RRd stars (black empty rectangles) we marked both periods. The two anomalous Cepheid (ACEP) candidates are marked with empty circles. Stars with erroneous extinction correction are marked with black crosses. Right: distribution of the sample in the absolute Gaia and J–K (bottom) color–magnitude planes: here we marked the blue and red edges of the instability strip, as calculated by Marconi et al. (2015), with the blue and red solid lines. Differences between the two extinction corrections are indicated with dashed lines for the three LMC foreground stars.

back along the reddening vector to the expected colors indicates that they would be part of the RR Lyrae group. We note that the star LMC–RRLYR–03497—which apparently falls into the RRc group with the SFD correction is in fact an RRab pulsator, as indicated by its period and light-curve shape. We therefore conclude that both the Combined19 dust map of Bovy et al. (2016) and the SFD map overestimate the required extinction for stars that are directly in front of the LMC. In the near-infrared CMD (lower right panel of Figure 5), we were able to overlay the theoretical blue and red edges of the instability strip, as calculated by Marconi et al. (2015). In this CMD the RRab and RRc stars appear to be mixed in color, likely because neither magnitudes represent the mean brightness. However, multiple stars fall outside of the first overtone blue edge, but almost none are redder than the fundamental mode red edge.

We identified two stars that have the expected colors but still appear to be more luminous than the bulk of the sample: ASAS J221052–5508.0 ($P = 0.887$ days) and SX PsA ($P = 0.563$ days) are both above the RR Lyrae locus, although only marginally in the latter case. K brightness is only available for the latter, but this also appears to exceed the brightnesses of the rest of the stars. We consider the possibility that these are anomalous Cepheids (ACEPs) in Section 3.2.4. The intrinsically faintest RR Lyrae star in the sample is XZ Mic.

The color–magnitude diagram also shows that the RRc and RRab subclasses (as determined in the next section) clearly cluster toward the blue and red sides of the group in the Gaia passbands, with the RRd stars falling in the middle. The apparent color values themselves are typically precise to less than 0.05 mag, which would make color-based classification possible, but extinction correction imparts further uncertainties typically in the range of 0.1–0.3 mag. This means that although the RRc and RRab data points clearly separate in the Gaia CMD (but not in the near-infrared one), their uncertainty ranges overlap, which prevents us from using color as a primary classification metric.

3.2.3. Relative Fourier Parameters

With the Fourier parameters of the main pulsation periods and harmonics fitted, we can compute the relative Fourier parameters $R_{i1} = A_i/A_1$ and $\phi_{i1} = \phi_i - i\,\phi_1$ to classify the stars based on their light-curve shapes (Simon & Teays 1982). We use sine-based Fourier series in the form of $m = m_0 + \sum_i A_i \sin(2\pi\, if_0 t + \phi_i)$, where m_0 is the average brightness, f_0 is the dominant pulsation frequency, A_i and ϕ_i are the amplitudes and phases of each harmonic, and i is the harmonic order. This method does not necessarily separate non-pulsating stars from pulsating stars if their variations look similar but it is capable of differentiating between pulsation modes among the RR Lyrae stars. We compared the TESS results to those of the OGLE stars as a reference, as shown in Figure 6. Since the TESS passband is centered on the I band, we expect only minor differences in the distribution of the Fourier parameters of the OGLE I and TESS measurements. The R parameters indeed show very good agreement for both the RRab and RRc loci, but we see differences in the ϕ parameters, with the TESS data clustering at slightly lower values than the OGLE data. A systematic shift between the ϕ_{31} parameters in the I band and TESS passband light curves indicate that the we cannot adopt existing relations to calculate the photometric metallicities (Skowron et al. 2016). We estimate the shifts in phase difference to be $\phi_{21,I} - \phi_{21,\mathrm{TESS}} \approx 0.15$ and $\phi_{31,I} - \phi_{31,\mathrm{TESS}} \approx 0.25$ rad. Calibration of photometric [Fe/H]

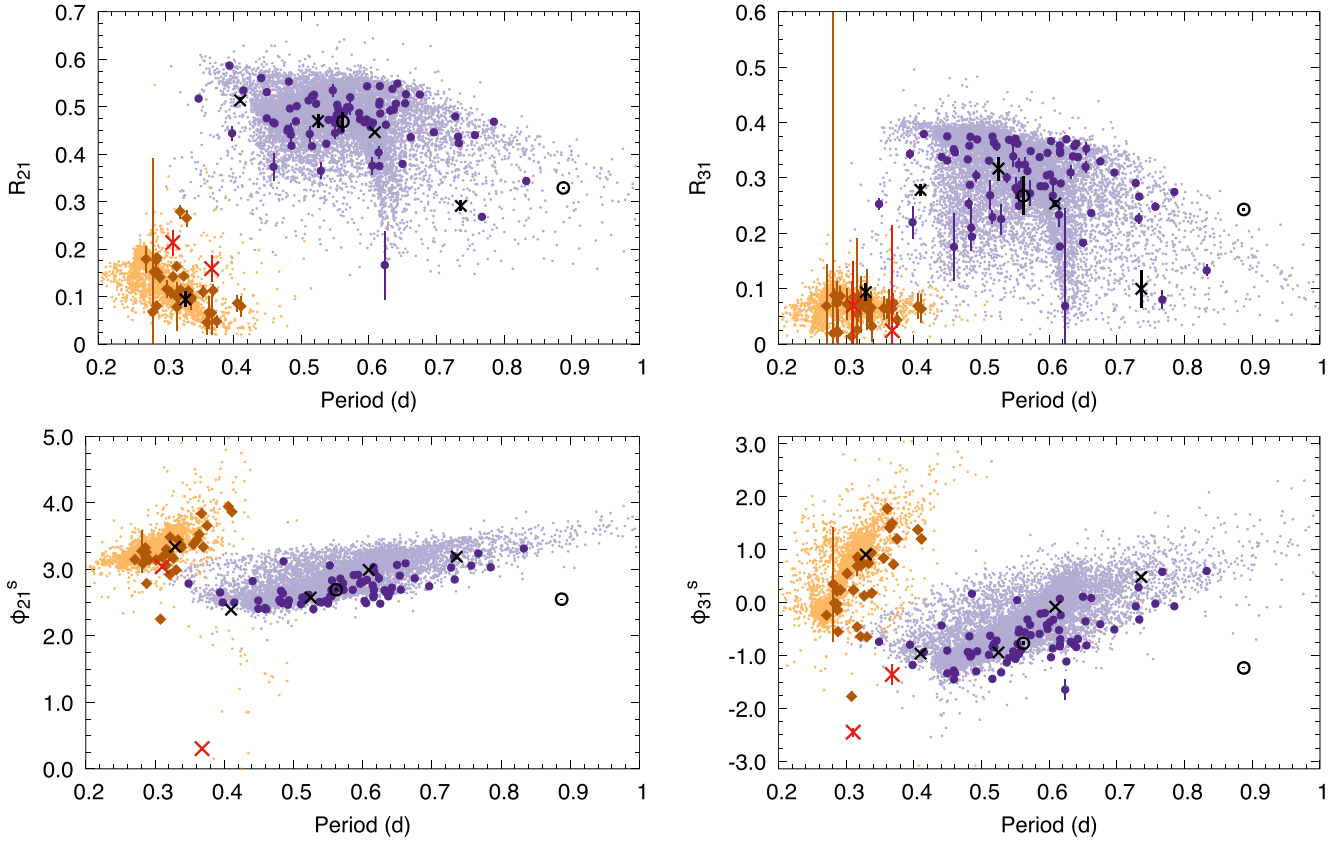

Figure 6. Relative Fourier parameters R_{i1} and ϕ_{i1} of the TESS first light sample (large symbols), overlaid on the OGLE *I*-band values (dots). Orange and purple points mark RRc and RRab stars. The two empty circles are the ACEP candidates; the three black crosses in the RRab group are the three LMC foreground stars. The two red crosses in the RRc group are two false-positive, non-pulsating stars.

indices for the TESS passband will be discussed in a separate paper.

We indicated the three LMC foreground stars with black crosses. Each appears within the RRab loci of each parameter, confirming that these are RRab stars and that their intrinsic luminosities and colors must be lower than what we computed with the `mwdust` code. We also indicate the ACEP candidates with black circles.

Although we removed obvious eclipsing binary and rotational variable light curves from the sample prior to classification, the distance–luminosity and period–luminosity plots in Figure 4 revealed two further dwarf stars in the sample (blue plus signs in Figure 4). Their Fourier parameters are at least in marginal agreement with the distribution of RRc stars: the R_{i1} parameters agree, the ϕ_{21} is inconclusive since at longer overtone periods bona fide RRc stars span the whole range, and only the ϕ_{31} value appears to be discrepant. Therefore, classification of these two stars would have remained ambiguous from the light-curve shapes alone, and the accurate parallax data were necessary to exclude them from the sample.

Based on the absolute brightness, light-curve shape, and period ratio information, we identified 82 RRab, 31 RRc, and 5 RRd stars among the selected stars. This amounts to 118 RR Lyrae targets in total.

Finally, we compared the pulsation periods we obtained with those in the Gaia DR2 catalog (specifically, the RR Lyrae and Cepheid periods calculated by Clementini et al. 2019). Of the $118+2$ stars, 21 have not been identified as either type of variable; in those cases, we queried the International Variable Star Index (VSX). As Figure 7 shows, almost all Gaia or VSX periods agree with those we derived from the TESS light curves. The most distant point is V360 Aqr, an RRab that was classified as a Type II Cepheid (T2CEP) by the Gaia algorithm. A smaller but clear difference is observed for LMC–RRLYR–23457. The rest of the stars show only small differences, although in multiple cases, such differences exceed the uncertainties of both the TESS and Gaia periods. Most of the stars have been correctly classified in Gaia: aside from V360 Aqr, only four more stars are erroneous. SU Hyi, the shortest-period RRab star, and a double-mode star, Gaia DR2 6529889228241771264 were classified as RRC stars, whereas two RRab stars, AE Tuc and ASAS J215601–6129.2, were classified as RRD stars in the Gaia notation. These statistics agree with earlier validation tests based on Kepler data, which found that class mismatches in the Gaia classification are rare among the bright RR Lyrae stars (Molnár et al. 2018).

3.2.4. Anomalous Cepheid Candidates

In addition to the 118 RR Lyrae stars, we also found 2 overluminous outliers, SX PsA and ASAS J221052-5508.0, both at $M_G = -0.5$ mag. The higher absolute brightness and long period ($P = 0.887$ days) suggest that ASAS J221052-5508.0 is an ACEP star rather than an RR Lyrae. The classification of SX PsA is more uncertain, given its shorter period. We compared the two stars' Fourier parameters to those of the OGLE ACEPs in Figure 8 and they both fit into the fundamental mode ACEP locus, although the latter is at the short-period end of the distribution. At the shortest periods, however, the distribution of RR Lyrae and ACEP Fourier

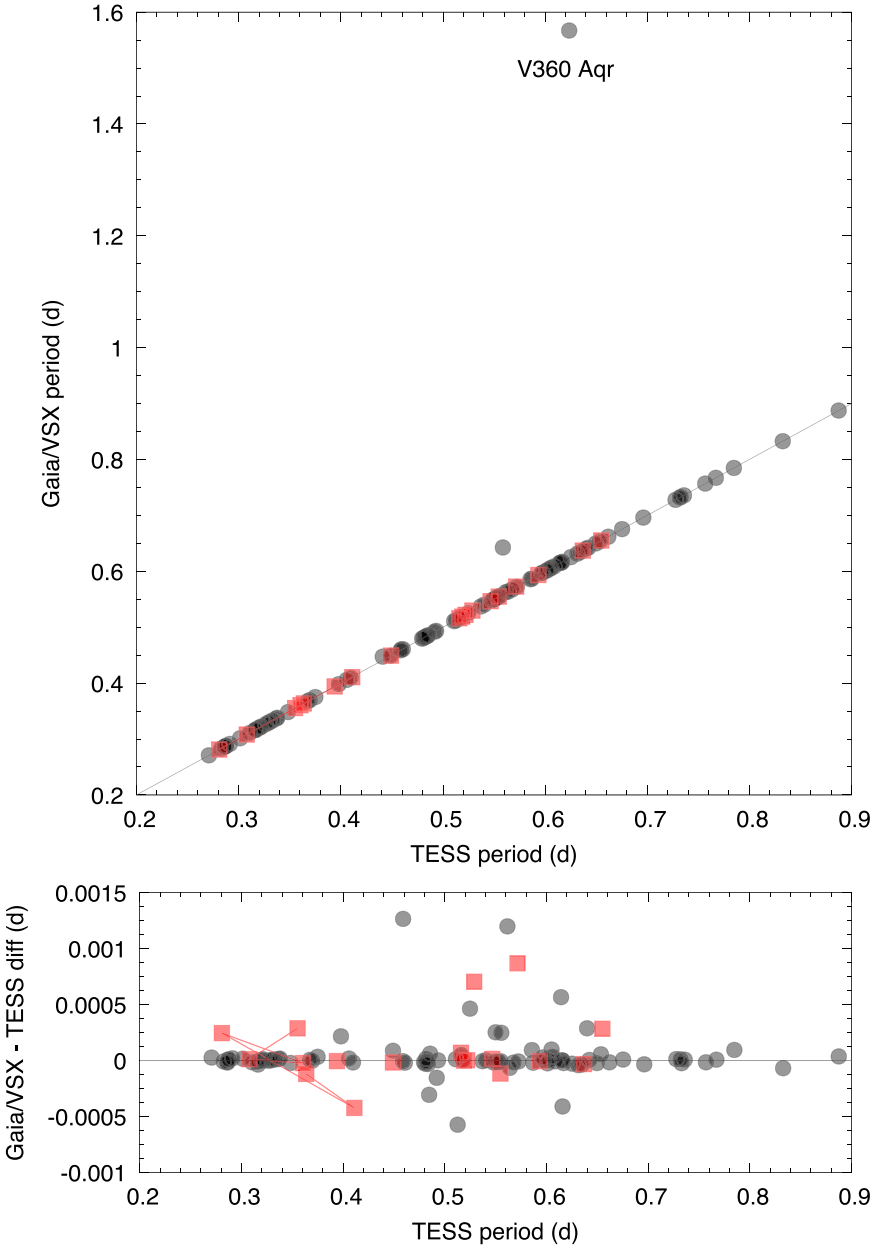

Figure 7. Comparison of the pulsation periods we derived from the TESS light curves and those calculated from the Gaia DR2 epoch photometry (gray) or present in VSX (red). Stars where two periods were identified only by either TESS or Gaia are connected with lines. The lower panel shows the difference values. Uncertainties are smaller than the symbols.

parameters strongly overlap, and as Figure 6 shows, SX PsA fits into the RRab locus as well.

We propose that the more luminous one, ASAS J221052–5508.0, is indeed a newly identified Galactic ACEP. The classification of SX PsA is less certain, and we consider it an ACEP candidate. As SX PsA also displays strong amplitude modulation, this would be another ACEP star showing the Blazhko effect, after the identification of the first modulated ACEP candidate in the K2 observations by Plachy et al. (2019). Although we prefer the ACEP classification, SX PsA could possibly be an unusually luminous RR Lyrae star, too.

Unfortunately, most ACEPs identified in Gaia DR2 are too far away to have accurate geometric parallaxes. We therefore do not yet have a well-calibrated PL relation for Galactic ACEP stars, and too few have been studied so far with TESS (Clementini et al. 2019; Plachy et al. 2021). The importance of distance determination was also highlighted by Braga et al. (2020), who showed that short-period ACEP and Type II Cepheids can overlap in period with long-period RR Lyrae stars. Period itself is therefore not a unique classifier and a reliable separation of Galactic short-period ACEP stars from long-period RR Lyrae stars will require accurate light-curve shape information, distances, and colors. Once we can separate these with confidence, we will be able to construct a PL relation for Galactic ACEP stars, too.

3.3. The Blazhko Effect

Modulation has been detected in all subtypes of RR Lyrae stars, even in RRd stars (see, e.g., Smolec et al. 2015; Plachy et al. 2017b; Carrell et al. 2021). Amplitude and phase modulation in RR Lyrae stars happen over periods extending

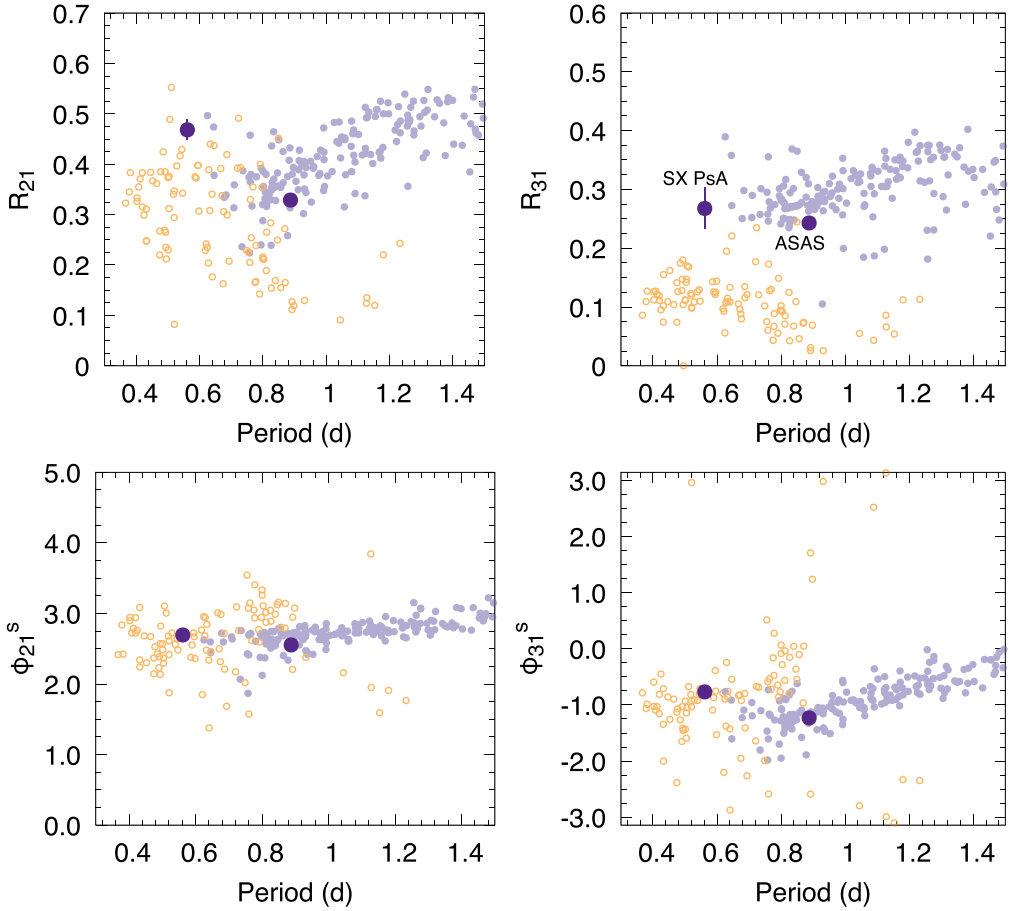

Figure 8. Relative Fourier parameters of the two ACEP candidates, compared to the OGLE ACEP samples (Soszyński et al. 2015, 2020).

from a few days to years, therefore one or two sectors' worth of data are not well suited to studying the Blazhko effect. Nevertheless, we were able to identify the signs of amplitude and phase changes in several stars. Although we cannot rule out the possibility of non-cyclic amplitude and phase shifts in RR Lyrae stars over short timescales, evidence for such events is scant in long-term observations. We therefore consider contamination from non-Blazhko objects to be negligible and classify all targets with smooth changes to the pulsation properties as Blazhko stars.

Currently, the best hypothesis for the Blazhko effect is the nonlinear mode resonances model (Buchler & Kolláth 2011; Kolláth 2018). It agrees best with observations; however, the model is based on amplitude equation calculations, and the accurate reproduction of modulated light curves in hydrodynamic simulations is still in its infancy (see, e.g., Smolec & Moskalik 2012; Molnár et al. 2012a; Goldberg et al. 2020; Joyce et al. 2020).

3.3.1. What is the Blazhko Effect—for an Observer?

Since we do not have a universally accepted model for the Blazhko effect, we have no a priori constraints on the distributions and limits of the modulation periods and amplitudes. With the precision achieveable with Kepler and TESS, we can now detect millimagnitude-level modulations: however, we must ask whether we should label all quasi-periodic modulations as the Blazhko effect. Moskalik et al. (2015), for example, stated that the small amplitude and phase fluctuations in the Kepler RRc stars do not resemble the classical picture of the (semi)coherent modulations we know as the Blazhko effect. Similarly, Benkő et al. (2019) found that cycle-to-cycle variations in Kepler RRab stars can cause small side peaks, but the true incidence rate of quasi-periodic modulation is 51%–55%. In contrast, the idea that all RR Lyrae stars are modulated was recently suggested by Kovács (2018), based on his processing of K2 data. It is therefore important to test whether this hypothesis can be confirmed with the TESS sample.

The classical Blazhko effect manifests itself as side peaks around the pulsation frequency and its harmonics in frequency space. In principle, searching for significant side peaks is a straightforward exercise. However, contamination from stellar or instrumental sources, as well as systematics introduced by the photometric and post-processing pipelines can inject variations mimicking small modulations. Slow changes in the average flux, for example, can be caused both by changes in the amount of captured flux (e.g., intra- and interpixel sensitivity changes) or by contamination from a separate source, or both, but they affect the flux amplitude differently. Choices to correct these via scaling and/or subtracting flux can be a degenerate problem. Improper handling of systematics and contamination may either introduce artificial amplitude changes that appear as side peaks in the frequency spectra, or remove slow variations intrinsic to the star. The same issues were found to affect some of the K2 light curves as well (Plachy et al. 2017a, 2019). In the TESS data we found that systematics tend to generate side peaks surrounding only the pulsation frequency or very few harmonics, whereas Blazhko stars have a clear series of side peaks along the harmonics.

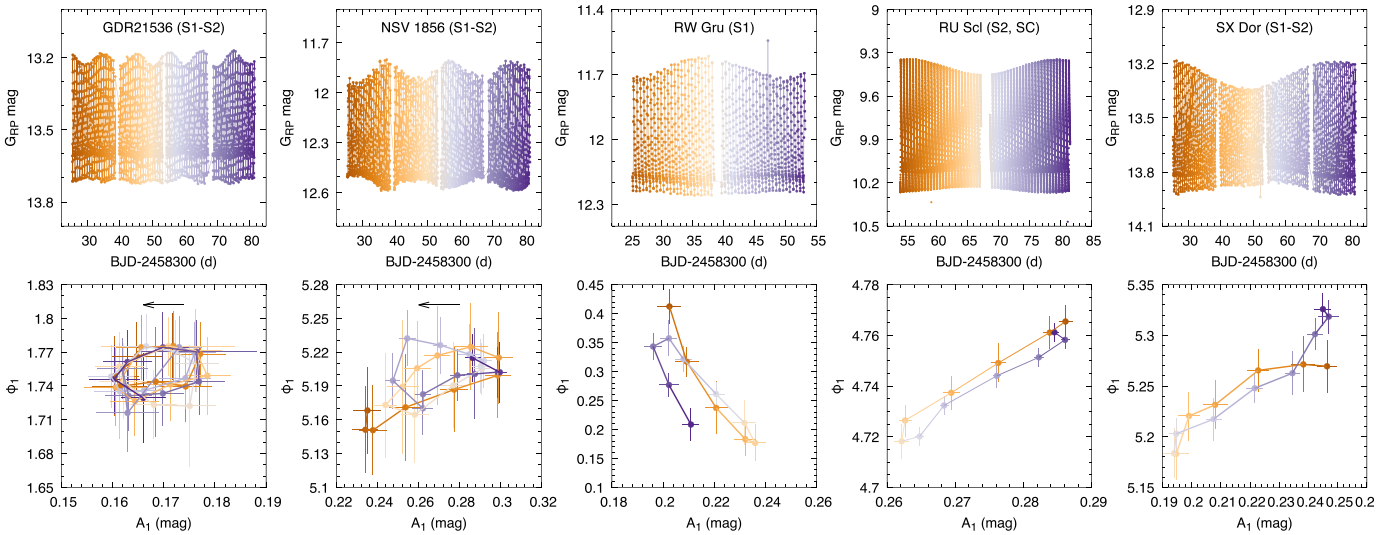

Figure 9. Five examples of modulated RRab stars. Upper row: light curves. Bottom row: loop diagrams of the A_1 and ϕ_1 Fourier terms. Arrows mark the direction of progression, where applicable, and color follows progression in time.

Furthermore, the Kepler data demonstrated that stars where no coherent amplitude and phase variation were detected still showed irregular amplitude and phase fluctuations, similar to those seen in Cepheids (Benkő et al. 2019). While over long timescales this manifests as red noise around the main harmonic series, over the much shorter TESS observations, stochastic variations can conceivably appear as a single or a few significant frequency components in some cases.

Another problem we encountered stems from the fact that the amplitude of the main frequency peak is several orders of magnitude larger than the photometric noise level. This can cause some algorithms to be able to reach sufficiently small pre-set residual levels even with a slightly offset frequency fit. This results in an apparent phase shift between the data and the fit which can be mistaken for intrinsic modulation. We noticed this behavior when fitting RRc stars in PERIOD04. We therefore double-checked all stars where an apparent linear phase shift was observed without any counterpart in the pulsation amplitude and then adjusted the pulsation frequency manually to minimize the phase shift over the length of the data. Here we also note that nearly linear phase shifts in short data sets can be caused by a very long modulation cycle as well, but we cannot separate those based on the TESS data alone, if no significant amplitude change is detectable alongside with them.

Therefore we refrain from claiming that any star that shows side peaks to the main pulsation frequency and its harmonics must automatically be a Blazhko star and set more strict rules. However, in lieu of a detailed model, reasons either for or against such distinction are based on phenomenological and methodological considerations alone.

3.3.2. Blazhko RRab Stars

Uncertainties in the amplitude and phase variations can be mitigated by requiring the simultaneous detection of both. This approach worked well for the original Kepler data (Benkő & Szabó 2015). We followed the same technique in our study, but did not limit the modulation periods, i.e., we classified clear but non-repeating amplitude and phase changes as likely long-period Blazhko stars.

Of the 82 RRab stars, we were able to identify Blazhko cycles or amplitude and phase changes compatible with partial cycles in 39 cases. In nine more stars, we detect some temporal changes but cannot say conclusively whether those variations are generated by intrinsic modulation or contamination from blending and/or stray light. In a further nine cases, contamination is present, or the calculated amplitude drops similarly throughout the sector with the phase not changing; therefore, we cannot rule out that low-level modulation is present. This provides an occurrence rate of at least 47.5% (39/82) and, at most, 70.7% (58/82) which agrees with results from multiple different surveys (see, e.g., Jurcsik et al. 2009; Benkő et al. 2014). The results are summarized in Appendix Table 7. Most of the detections are only partial modulation cycles, making it impossible to determine the modulation period(s). We were able to determine or estimate the Blazhko periods in five stars. The shortest one is SU Hyi, with a period of $P_{\rm BL} = 5.55$ days, which is among the shortest values ever recorded (Skarka et al. 2020). We investigate the light curve of SU Hyi in more detail in Section 3.8. In two more cases we identify new, shorter modulation periods in known Blazhko stars.

The Blazhko effect comes in many shapes and forms. Recenty, Skarka et al. (2020) separated the modulated OGLE stars into six morphological groups. Our TESS light curves are unfortunately too short for similar exercises, but we can still examine how the amplitudes and phases vary over time. We calculated the temporal variations both by fitting a template light curve to the segments of the data and by just fitting the A_1 and ϕ_1 parameters in each segment. The results of the two methods agreed with each other. We present five examples in Figure 9. The loop diagrams show a variety of $A_1 - \phi_1$ relations, with the two parameters changing in a correlated, anticorrelated or circular pattern.

3.3.3. Blazhko RRc Stars

Among the RRc stars we found four modulated stars, giving us an occurrence rate of approximately 13%. This is more than double than the 5.6% rate found by Netzel et al. (2018) among the overtone stars in the bulge, and closer to the results of targeted studies of globular clusters (Jurcsik et al. 2014; Smolec et al. 2017). It is, however, based on a very small sample size.

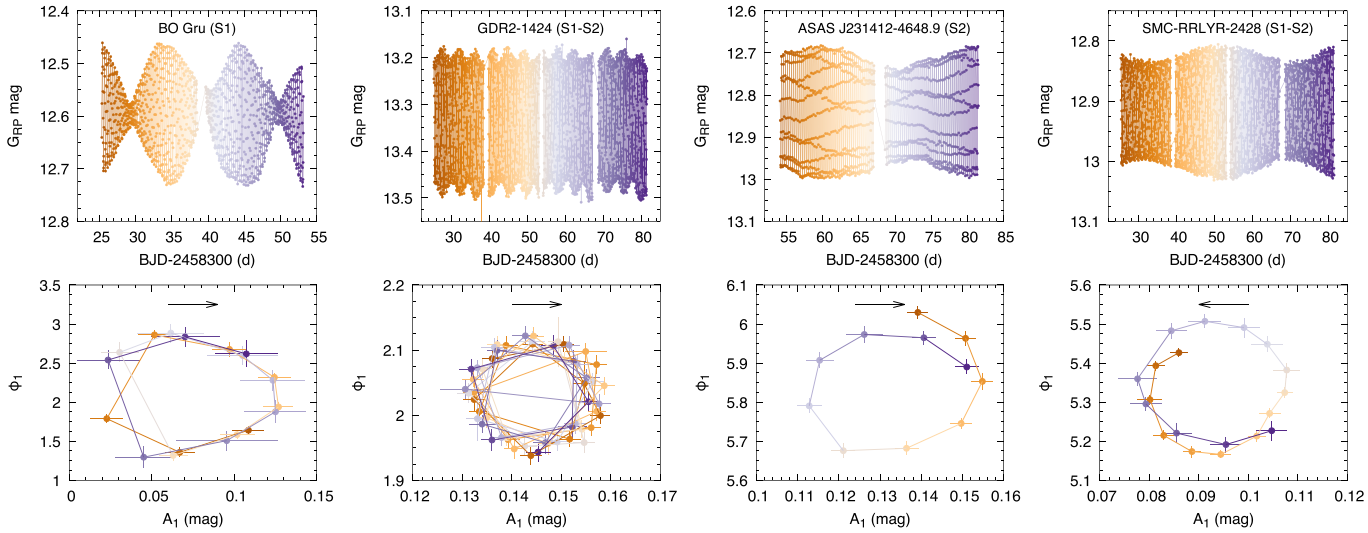

Figure 10. Same as Figure 9 but for modulated RRc stars.

We note that a fifth star, IY Eri, also shows low-level amplitude variation and side peaks but we did not detect unambiguous phase variations. This suggests that the star is more likely to suffer from contamination than being modulated.

These four stars paint a complex picture of Blazhko morphology among RRc stars. ASAS J231412–4648.9 and OGLE–SMC–RRLYR–2428 are archetypal modulated stars with moderate amplitude changes and roughly month-long cycles (22.2 ± 0.7 d and 38 ± 3 d, respectively). Gaia DR2 5495625579691991424 (hereafter GDR2–1424) has a modulation period of only 4.340 ± 0.010 days, which is among the fastest Blazhko cycles known: only a handful of stars are known with periods below 5 days, and all were recently found in the OGLE bulge collection (Netzel et al. 2018). The last one, BO Gru, has a nearly sinusoidal light curve with extreme amplitude changes and with a period of 10.07 ± 0.08 days, based on the TESS data in themselves. We initially classified this as a false-positive detection, but its luminosity places this star among the RR Lyrae variables.

We observe large differences in the amplitudes of the modulation side peaks in three out of four cases. In BO Gru, the two side peaks have amplitudes of 55.5 and 1.0 mmag, respectively. The asymmetry parameter, Q, defined as the ratio of the difference and sum of the side-peak amplitudes by Alcock et al. (2003), is –0.97 for BO Gru, and 0.88 for SMC-RRLYR-2428. We find only one side peak in GDR2–1424, but a detection limit of 0.5 mmag suggests a lower limit of $Q < -0.93$. The fourth star, ASAS J231412-4648.9, has more symmetric peaks with $Q = -0.13$. These findings are in agreement with that of Netzel et al. (2018), who measured strong side-peak asymmetries in many OGLE RRc stars. If we compare these results to the phase diagrams in Figure 10, we observe that the stars with negative Q values have $A_1 - \phi_1$ loop diagrams with clockwise progression, whereas positive Q pairs with counter-clockwise progression. This correlation between the side-peak asymmetry and the loop direction is in agreement with the analytical modulation formalism presented by Benkő et al. (2011).

3.3.4. Clearly Nonmodulated Stars

We identified 22 RRab stars whose frequency spectra do not show any significant side peaks (signal-to-noise ratio (S/N) > 4 against the smoothed spectra) near the main peak or its harmonics. This indicates a lower limit of 28.2% for non-modulated stars at the photometric precision of TESS. Four examples are shown in Figure 11. Red dashed lines mark the fitted and subtracted main peaks, plotted over the residual frequency spectra. Blue lines show the $S/N = 4$ levels. These four stars are clearly not modulated, with an upper limit of 0.5–0.6 mmag for any side peaks in the spectra. While even these stars can conceivably experience modulation below the sensitivity or over considerably longer periods than the length of one or two Sectors, the result indicates that after rigorous processing, RRab stars without side peaks can be identified in the sample.

3.4. Additional Modes and Asteroseismology

Extensive, high-quality data revealed an abundance of additional low-amplitude modes in RR Lyrae stars over the last decade. Interestingly, in RRab stars these almost always coincide with the presence of the Blazhko effect, whereas nonmodulated stars seem to be pulsating purely in the fundamental mode. Additional modes were also detected in some RRab OGLE stars. A preliminary analysis of the K2 observations of RRab stars, however, indicated a surprising dichotomy between the OGLE bulge sample and the field stars observed by space telescopes (Molnár et al. 2017). Additional modes were found only in distinct segments of the Petersen diagram in the OGLE light curves: a larger group at the shortest periods (0.28–0.45 days) (Prudil et al. 2017), from which three stars were then observed by K2 as well (Nemec & Moskalik 2021), a few similar, but long-period (>0.65 days) stars (Smolec et al. 2016), and the group of anomalous RRd (aRRd) stars, offset in period ratio from the normal RRd stars, between 0.45–0.55 days (Soszyński et al. 2016). In contrast, virtually all of the CoRoT, Kepler, and K2 detections group in the middle (0.42–0.7 days). The only exceptions are the field stars V1127 Aql and V1125 Sgr, observed by CoRoT and K2, respectively, which fall into the short-period group (Chadid et al. 2010; Nemec & Moskalik 2021). If this discrepancy is real, it could signal physical differences between the bulge and halo/field populations that manifest themselves in the asteroseismology of RR Lyrae stars as well. We note that the analysis of the OGLE sample by Prudil et al. (2017) focused

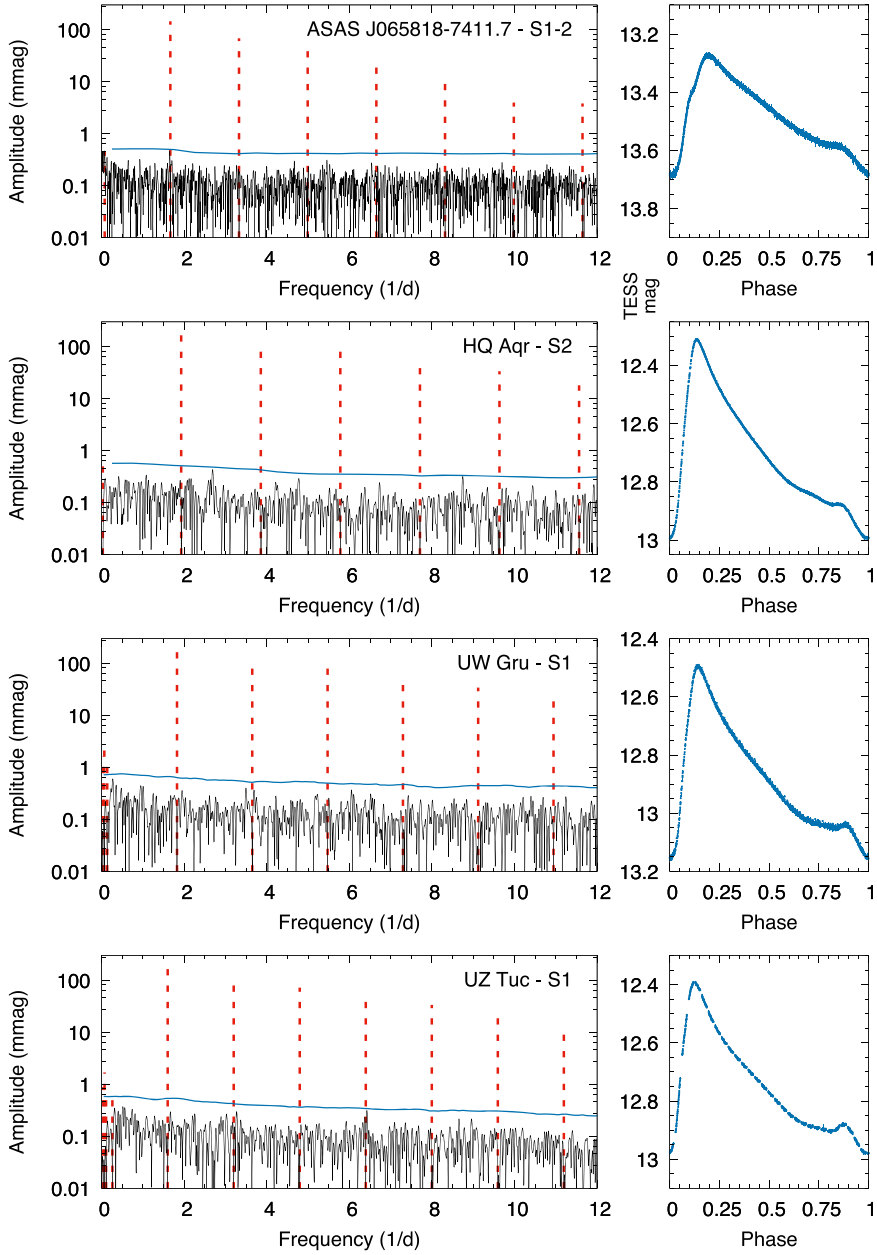

Figure 11. Non-Blazhko RRab stars. Left: residual spectra with the positions of the pulsation peak and its harmonics (red dashed lines) and the 4.0 S/N level (blue line) marked. Right: folded light curves.

primarily on strong extra modes in the short-period, non-Blazhko stars, whereas that of Smolec et al. (2016) looked exclusively at long-period stars. The mid-period range was not searched thoroughly, so the modulated stars in this range could still hide bulge stars with additional modes in them (Z. Prudil & R. Smolec 2019, private communication).

Detailed analysis of RRc and RRd stars via space-based photometry has been scant so far. About a dozen stars have been published, based on data from a variety of missions, ranging from MOST, CoRoT, and Kepler to K2, respectively (Gruberbauer et al. 2007; Szabó et al. 2014; Moskalik et al. 2015; Molnár et al. 2015b; Kurtz et al. 2016; Sódor et al. 2017). Many more were identified in the K2 campaigns by Molnár et al. (2018) and Plachy et al. (2019) but they still await closer inspection. However, the RRc population in the Galactic bulge has been thoroughly studied in the OGLE-III and IV surveys (Netzel et al. 2015a, 2015b), as well as the members of the globular clusters M3 and NGC 6362 (Jurcsik et al. 2015; Smolec et al. 2017). A recurring theme of these works has been the presence of the 0.61-type or f_X modes that seem to have a strong association with the first radial overtone in RRc and RRd stars both. In contrast, so far there is no indication of the modes associated with RRab stars appearing in double-mode stars.

3.4.1. Additional Modes in RRab Stars

We detected additional modes in 29 RRab stars, which represents 35% of the sample. The majority of these are also modulated or possibly modulated, with only two stars falling into the contaminated, and hence uncertain category, and another into the nonmodulated group. This result agrees with findings based on Kepler and CoRoT data, where additional modes were also identified almost exclusively in Blazhko RRab stars, suggesting a

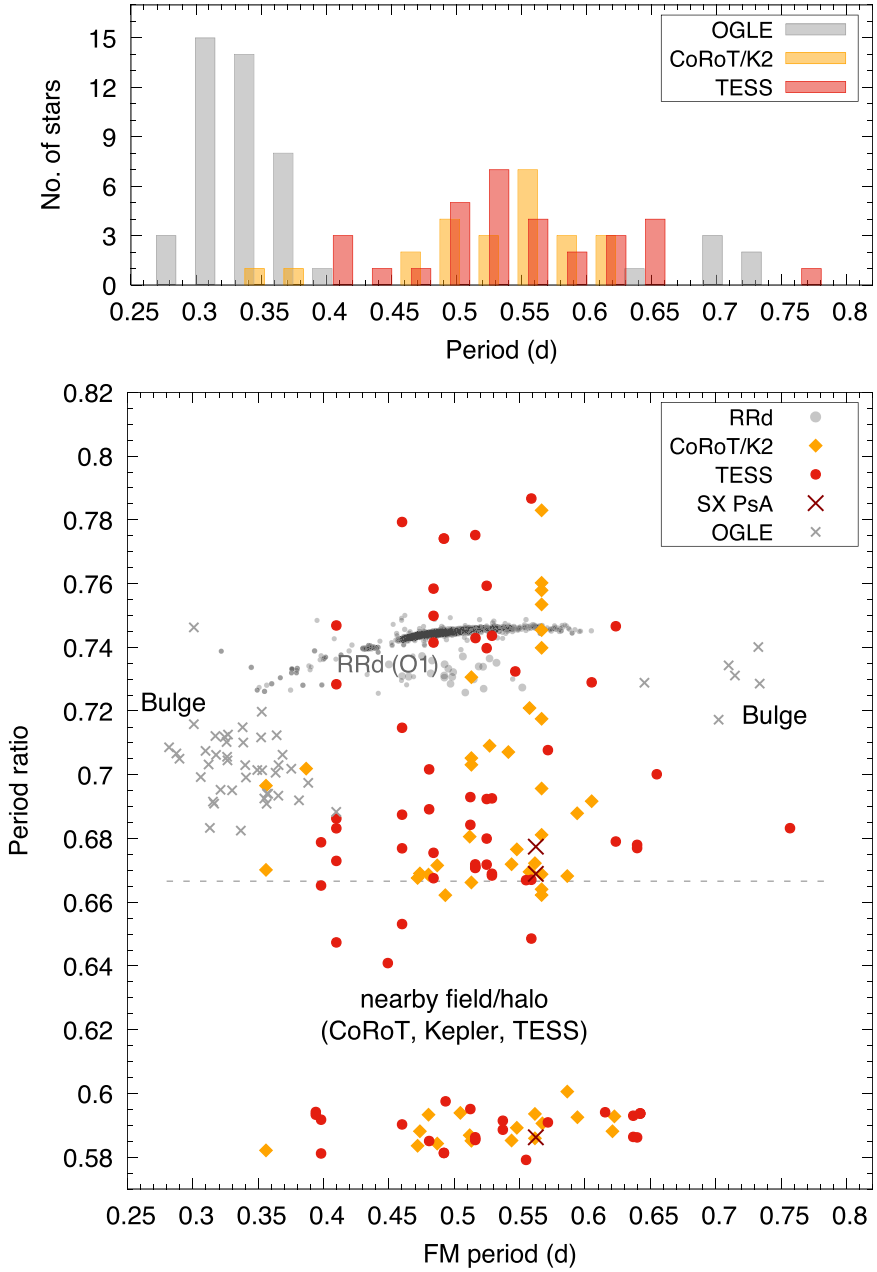

Figure 12. Top: period distribution of individual RRab stars in which additional modes were detected: OGLE (gray), CoRoT/Kepler/K2 (orange), and TESS (red). Bottom: Petersen diagram for the RRab stars. Gray crosses are the OGLE bulge results, orange diamonds are from CoRoT, Kepler, and the K2-E2 engineering test run, and red points are the TESS observations. Small gray dots mark the distribution of the RRd stars and thus the position of the first overtone. The dashed line indicates the position of the half-integer frequency indicating period doubling. Large red crosses mark the ACEP candidate SX PsA. Note that stars may have multiple additional signals detected in them.

connection between modulation and excitation (Benkő et al. 2010; Szabó et al. 2014; Molnár et al. 2017).

According to the recent results, additional modes in RRab stars appear in three broad regions as we show in Figure 12 (Molnár et al. 2017). Each of the three types of signals may appear alone, in pairs, or together in the stars. One is near the expected value of the second radial overtone between $P_2/P_0 \approx 0.58$–0.60. These signals, usually labeled as f_2–type modes, form the most well-defined group in the Petersen diagram. Another set of peaks, near $P/P_0 \simeq 2/3$ or, $f/f_0 \simeq 1.5$, is the potential sign of PD (Szabó et al. 2010; Kolláth et al. 2011). However, the peaks here do not form a well-defined line around the half-integer frequencies as one would expect from the presence of PD only. Instead they spread out to lower frequencies, up to ratios $P_2/P_0 \approx 0.7$. While some spread in the observed frequencies can be expected from the variable nature of PD, the peaks clearly group at $P/P_0 \geqslant 2/3$ ratios instead of around the $2/3$ value. This suggests that we do, in fact, see nonradial modes in this range, which makes differentiating bona fide period-doubled RRab stars from stars with nearby nonradial modes very difficult.

The third group, the f_1-type modes, is loosely connected to the second, between $P_2/P_0 \approx 0.71$–0.78, encompassing the RRd ridge and the aRRd stars. Some of these may potentially be the appearance of the first overtone, and model calculations offer two ways in which the mode can become excited through mode resonances outside the normal RRd regime. When the

fundamental mode goes through a period-doubling bifurcation, hydrodynamic models can become unstable against the first overtone too (Molnár et al. 2012b). Alternatively, linear model calculations suggest that a parametric resonance between the fundamental, first, and second overtones could potentially excite the first overtone in aRRd stars, if their metallicity is high enough (Soszyński et al. 2016). However, some of our stars are too far away from the RRd and aRRd groups to accommodate a radial mode and must be exciting non-radial modes near the first overtone instead. Linear calculations of non-radial-mode RR Lyrae models done by Dziembowski & Cassisi (1999) indicate that $\ell = 1$ modes have the highest linear growth rates near the frequencies of the radial modes ($\ell = 0$), such as the fundamental mode or the first overtone. Therefore, it is plausible that the peaks we detect near the first overtone position are various $\ell = 1$ modes.

Our findings are generally in good agreement with the preliminary results obtained from the K2 sample (and the few CoRoT stars). While our first collection of TESS stars with additional signals covers a wider period range than that of K2 (0.39–0.7 day instead of 0.42–0.65 days), the discrepancies with the OGLE bulge sample are still present. Extending the TESS sample with further sectors and fainter stars will be crucial to understanding the difference between the bulge population and those in the vicinity of the Sun. TESS will also enable us to compare the distribution of modes between other populations, such as the halo and disk stars.

We also detect three signals in the ACEP candidate SX PsA. These fit right into the distribution of additional modes of the RRab stars. This could mean either that SX PsA is also an RRab star, or that ACEP stars have very similar additional modes excited. An example of the latter has been observed in the ACEP prototype XZ Cet, a first overtone star, in which the f_X-type modes were found in the TESS data. The signals in XZ Cet line up perfectly with the modes detected in RRc and first overtone classical Cepheids (Plachy et al. 2021).

3.4.2. Additional Modes in RRc/RRd Stars

As mentioned previously, a common phenomenon among RRc stars is the presence of peculiar additional modes. One class of modes appears between period ratios $P/P_{O1} \in (0.6, 0.64)$, forming two distinct loci at ratios $\approx$0.615 and $\approx$0.63, as shown in Figure 13. These modes, called either f_X or 0.61-type modes in previous works, appear to have a very strong connection to the first radial overtone. They appear in RRd stars and in classical Cepheids (Moskalik & Kołaczkowski 2009; Molnár et al. 2017), and have been recently identified in an overtone ACEP star as well, as described in the companion paper (Plachy et al. 2021). We now know that the mode detected in AQ Leo, the first additional mode observed in an RR Lyrae star, also belongs to this group (Gruberbauer et al. 2007). The other distinct group is less frequent and has a period longer than the first overtone, at $P_{O1}/P \approx 0.686$ (or, $P/P_{O1} \approx 1.458$). The latter mode is, notably, longer than the expected fundamental period of a normal RR Lyrae star that would have a period ratio of $P_{O1}/P_{FM} > 0.725$ (Netzel et al. 2015a).

The origins of these modes are not yet settled. One possibility presented by Dziembowski (2016) connects the short-period, 0.615 and 0.63 ratio signals to $\ell = 8$ and 9 modes. However, in that scenario, the true mode frequency is the $1/2f_X$ subharmonic, and the f_X and $3/2f_X$ peaks we detect are harmonics: its only the viewing geometry and cancellation effects that make the f_X peak the strongest. The long-period mode is even harder to explain: if we assume that these stars are RR Lyrae variables, the signal would belong to a heavily damped $\ell = 1$ mode. Excitation of such a mode without any other, much less damped neighbors is very hard to explain. Alternatively, it could be the fundamental mode of a binary evolution pulsator: a low-mass, stripped core of a red giant that could accommodate such a low P_{O1}/P_{FM} period ratio. These are known to exist but are very rare (Pietrzyński et al. 2012). Furthermore, some stars show both types of extra modes, and the low-mass models cannot accommodate the high-ℓf_X modes since those would also fall to different period ratios than in normal RR Lyrae stars.

After the analysis of the 31 TESS stars, we concluded that although additional modes are frequent in RRc stars, they are not universal. We identified six stars (19%) among the group to be pure overtone pulsators, down to the millimagnitude level. We found the incidence rate of the f_X and 0.68-type modes to be 65% and 16% (20/31 and 5/31), respectively, and one more marginal case that might be a 0.68-type mode, but the period ratio is somewhat higher at $P/P_0 = 0.699$ (Figure 14). These numbers are clearly much higher than the 8.3% and 1.3% incidence rates found by Netzel & Smolec (2019), based on the full OGLE bulge data that were limited by data quality. The incidence rate of the f_X was found to be 27% and 63% in high-cadence OGLE fields and in the globular cluster NGC 6362, respectively; the latter matches our result (Netzel et al. 2015b; Smolec et al. 2017). Both types of modes were identified simultaneously in two stars (6%) within the TESS RRc sample, in ASAS J213826-3945.0 and NSVS 14632323. The detection rate of the 0.68-type mode is $\approx$5% in the overall RR Lyrae sample, which is considerably higher than the estimated 0.8% contamination from binary evolution pulsators calculated by Karczmarek et al. (2017), suggesting that this mode must have a different origin.

One peculiar star in the RRc group is BV Aqr. Beside the f_X peaks it also shows two more signals at $f/f_1 = 0.709$ and 0.741 frequency ratios. These are both clearly outside the regimes where the 0.68-type mode and the subharmonics of the f_X modes would exist. The latter component, however, could conceivably be the fundamental mode: this value is slightly below the canonical regime at the corresponding period of 0.491 days, but well within the extended region of aRRd stars (gray crosses in Figure 12). However, an important difference between BV Aqr and aRRd stars is that in aRRd stars the amplitude of the fundamental mode is almost always higher than, or at least the same order of magnitude as, that of the first overtone, whereas in BV Aqr the ratio is very low, only $A_1/A_0 = 0.016$. This suggests that BV Aqr is not an aRRd star, or not yet, but it is rare example of an RRd star with either an emergent or an unusually low-amplitude fundamental mode component instead. Interestingly, this possibility was already raised by Jerzykiewicz (1995), who identified a single secondary signal at the 0.717 ratio, i.e., between the two we identified. A further candidate for this type of mode content is NSV 1432, but there the detection of a signal with 0.740 period ratio to the first overtone remains marginal.

We identified the f_X modes in all five RRd stars. The 1/2 and 3/2 f_X peaks were also found in all cases but with lower amplitudes. We then searched the RRd stars for further extra modes. Neither the 0.68 mode nor any modes related to the fundamental mode were visible, although in RRd stars the $2f_{O1} - f_{FM}$ combination peak overlaps with the expected position of the f_2 group. Notably, we identified $f_X/2$ frequencies—

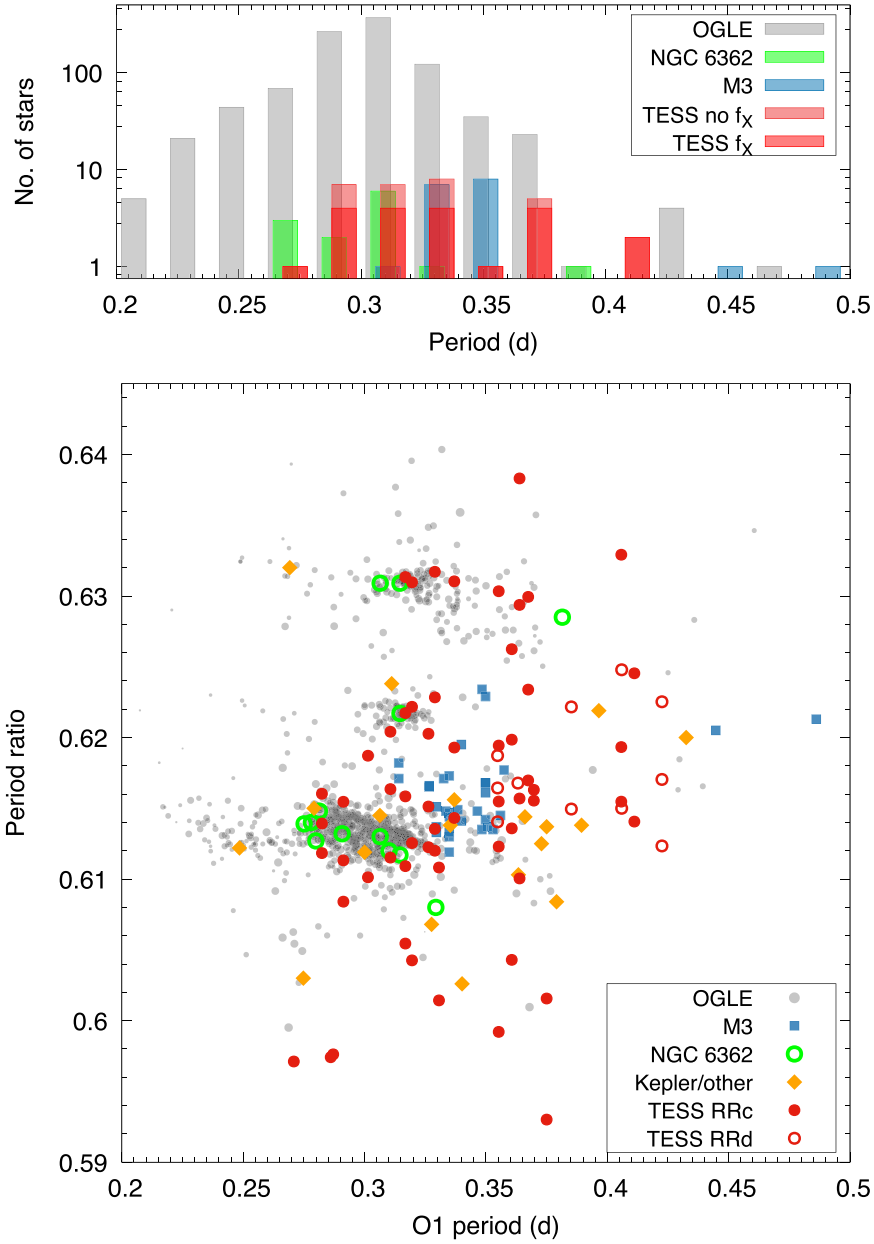

Figure 13. Same as Figure 12 but for the f_X modes in RRc and RRd stars. Top: period distribution for OGLE (gray), TESS (red), and from two globular clusters, M3 (blue) and NGC 6362 (green). The light red extensions mark the TESS RRc stars where the modes are absent. Bottom: Petersen diagram of the f_X or 0.61 type modes. Gray points are the OGLE detections by Netzel & Smolec (2019), orange diamonds are various stars collected by Moskalik et al. (2015) that include other space-based data, blue squares are the M3 stars by Jurcsik et al. (2015), green circles are the NGC 6362 stars (Smolec et al. 2017), and filled and empty red circles are the TESS RRc and RRd detections.

proposed to be the true pulsation frequencies by Dziembowski (2016)—in 9 RRc and 2 RRd stars, i.e., in about half of the stars where the f_X modes could be detected.

We then compared the distribution of the f_X modes to those of other RRc populations. The upper panel of Figure 13 presents the period distribution of the OGLE and TESS stars, plus the RRc stars from the globular cluster M3 that was surveyed by Jurcsik et al. (2015). The TESS sample is currently too small to draw strong conclusions from this histogram alone, except for the lack of short-period RRc stars in the TESS and M3 groups.

The lower panel of Figure 13 is a Petersen diagram where we included not only the recent OGLE results but also the additional modes found in the globular cluster M3 and various detections from Kepler, CoRoT, MOST, and other sources (Jurcsik et al. 2015; Moskalik et al. 2015; Netzel & Smolec 2019). It is immediately clear from this plot that the field stars seen by TESS are distributed much more evenly and do not form the clear ridges the bulge population does. Although the detections peak more or less at the same period range (0.28–0.32 days), the bulge stars extend farther out to shorter periods, whereas the field stars populate the longer side more evenly. The M3 group (blue squares) forms a rather tight clump that does not line up with the ridge of bulge stars.

All these differences suggest again that the mode content of RR Lyrae stars is dependent on the physical parameters, probably on the metallicity and age (evolutionary stage) as well. The existence of such dependencies has already been established for the radial modes in RRd stars, from both theoretical and observational approaches (see, e.g., Szabó et al. 2004; Coppola et al. 2015).

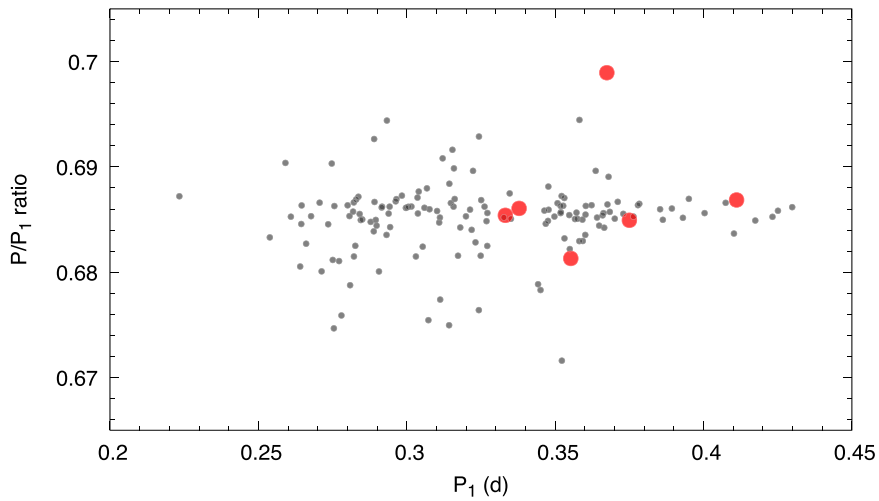

Figure 14. The 0.68-type modes: small black circles are the OGLE stars from Netzel & Smolec (2019); large red circles are the TESS detections.

Similarly, the models presented by Dziembowski (2016) show that higher masses and lower Z values may shift the proposed f_X modes to higher period ratios. We also know that the [Fe/H] abundances for RRc stars span a wide range, from [Fe/H] ≈ -2.5 up to the recently confirmed, metal-rich end: around –0.5 dex (Sneden et al. 2018). Unfortunately, most RRc stars in the TESS sample do not have [Fe/H] measurements of sufficient accuracy to test these theoretical predictions. Only 10 of them have photometric [Fe/H] values in Gaia DR2, and all have large uncertainties ($\pm$0.24 dex). Further, we identified only 15 RRab and 3 RRc stars among the recent spectroscopic and photometric [Fe/H] measurements published by Crestani et al. (2021a, 2021b) and by Mullen et al. (2021). Only 4 and 2 of those, respectively, feature extra modes, which prevents us from conducting a detailed analysis.

However, we know that the bulge population clusters around [Fe/H] $= -1.02 \pm 0.18$ dex, whereas a considerably lower value of [Fe/H] $= -1.43 \pm 0.07$ dex was found for the M3 RR Lyraes (Cacciari et al. 2005; Pietrukowicz et al. 2012). Furthermore, a recent, homogeneous study of a large sample of field RR Lyrae stars showed that their [Fe/H] values peak at -1.5 dex (Marengo et al. 2020). Spectroscopic [Fe/H] measurements for the two RRc stars with extra modes in the sample—AO Tuc (-1.69 ± 0.20) and BV Aqr (-1.61 ± 0.011)—match the average halo metallicity (Crestani et al. 2021b). It is thus evident that differences in chemical composition—and the changes those impart on the stellar structure—govern, in part, mode selection and mode frequencies in RR Lyrae stars, with our results suggesting that this holds for new modes as well.

We also compared the positions of the 0.68-type modes to those identified from the OGLE survey by Netzel & Smolec (2019). These cluster toward the long-period half of the distribution, just like the other modes do. Five stars are within the spread of the OGLE points, but one star, ASAS J212331-3025.0 lies outside, at a period ratio of nearly 0.70: we treat this sixth signal as a tentative detection.

3.4.3. Degeneracies and RRab Échelle Diagrams

In most cases additional modes in RRab stars appear clearly between the main pulsation frequency and its first harmonic (between f_0 and $2f_0$), along with lower-amplitude combination peaks at $f \pm nf_0$. We list these identifications, along with some peculiar signals, in the Appendix. However, there are exceptions to this pattern, where the highest-amplitude peak falls elsewhere. One example in the K2–E2 sample was already described by Molnár et al. (2015b), where the signal was tentatively identified as a low-frequency g mode, but the $f_g + f_0$ combination was suspiciously close to the 0.6 period ratio, the position of the second overtone-like peaks. We found similar examples in the present TESS sample as well. We identified multiple stars for which the highest-amplitude peak in the $f_{\rm addtl} + nf_0$ combination series is apparently below f_0 or above $2f_0$, yet these series have a component that coincides with the positions of the additional mode groups described above. These findings are shown in Figure 12.

In order to compare the various signal distributions in frequency and amplitude, we generated échelle-type diagrams for selected stars. Échelle diagrams are a key tool for investigating solar-like oscillations that create (quasi)repetitive patterns in the frequency spectrum or power-density distribution. Data are split into segments at the repetition frequency (for solar-like oscillations, the large frequency separation), and the amplitudes are mapped onto a frequency versus modulo frequency plane. Signals, such as consecutive oscillation modes, form vertical ridges in these plots (Bedding & Kjeldsen 2010). This type of visualization was already used for RR Lyrae stars and Cepheids to plot the distribution of modulation side peaks (see, e.g., Sódor et al. 2011; Guggenberger et al. 2012; Molnár & Szabados 2014).

Here, we are using échelle diagrams to study the additional modes in a new way. We utilize the repetitions in frequency spectrum caused by the coupling to the large-amplitude, strongly nonlinear radial mode. We created the frequency spectra and échelle diagrams in Figure 15 by first removing the main peak and its harmonics, plus the modulation triplets if necessary: these would otherwise obscure the low-amplitude signals. We then folded the residual spectra into échelle diagrams using the pulsation frequency (f_0). Unlike in normal échelle diagrams, however, the vertical ridges of Figure 15 represent the $f + nf_0$ combination series of the same mode instead of consecutive modes.

Four stars are shown as examples in Figure 15. The residual spectra and échelle diagrams show that:

1. Ridges generally appear at distinct modulus values, even though the position of the strongest peak in the series is

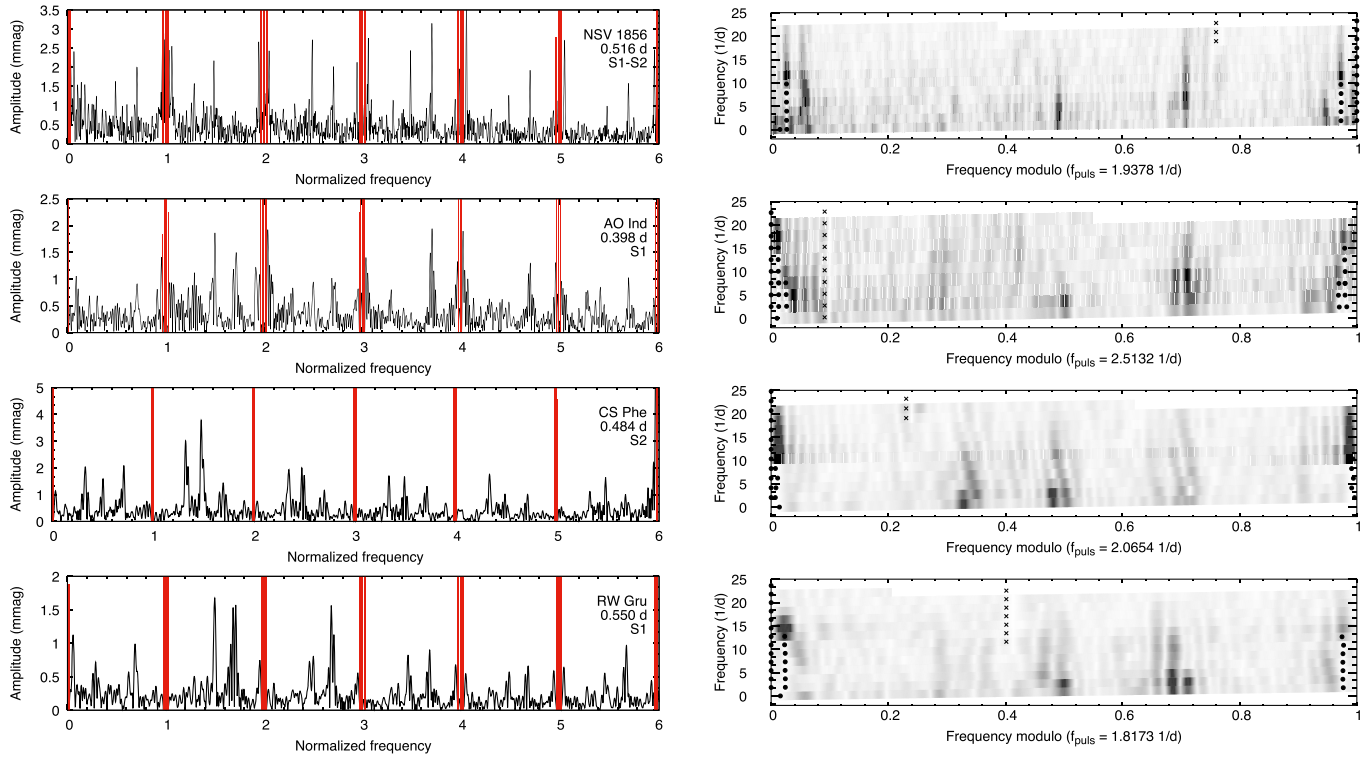

Figure 15. Fourier spectra (left) and échelle diagrams (right) of selected RRab stars. In the frequency spectra, pulsation and modulation peaks that have been removed are marked with red lines. In the échelle diagrams, the locations of these peaks are marked with black dots. Black crosses mark the locations of those pulsation harmonics that are reflected back from the Nyquist frequency.

not always between f_0 and $2f_0$. In NSV 1856, for example, the highest peaks for the two ridges appear between $2f_0$ to $3f_0$ and $3f_0$ to $4f_0$, respectively.

2. The length of the ridges, indicative of the coupling between the fundamental mode and the additional mode, can be very different: in both NSV 1856 and AO Ind, for example, the one corresponding to PD, around $\sim(0.5+n)f_0$ is rather short, whereas the f_2 one at $\sim(0.7+n)f_0$ spans almost the full frequency range. (The $\sim$0.6 period ratio translates to $\sim$1.7 frequency ratio.)
3. Some ridges have multipeaked structures that may also change as the frequency increases. In some other cases (CS Phe, DR Dor, SX PsA) we observe skewed ridges, as if the combination peaks were formed with a frequency different from the main peak and its harmonic series.
4. Some Blazhko stars, like NSV 14009, are devoid of any additional modes down to 0.3–0.4 mmag amplitudes.

The plots clearly show that additional signals in RRab stars are still limited to certain frequency modulus values. The variations in the amplitude distribution of the peaks, however, make it even harder to disentangle the mode identifications. It is unclear whether we are seeing the same few modes already described by the Petersen diagram, where other effects (e.g., nonlinear interaction with the fundamental mode or stellar inclination and viewing angles) may change the nature of the strongest frequency component. This scenario would be reminiscent of the proposed nature of the f_X mode in RRc stars, with the first harmonic of the pulsation frequency having higher amplitude.

Remarkably, the échelle plots also display a variety of structures, even though we would expect that the series of peaks are simply $f+n\,f_0$ combinations. The skewed ridges, in particular, would suggest that these additional frequency components in the star respond to a slightly detuned fundamental mode that we observe. A simple explanation would be that if we only observe a segment of the Blazhko cycle the pulsation frequency we measure is not modulation-averaged. However, using a fundamental mode frequency determined from more extended ground-based data has very little effect on the plots. We calculated the frequency shifts necessary to straighten the ridges to be –0.0078 days^{-1} (CS Phe), 0.0085 days^{-1} (DR Dor) and 0.0057 days^{-1} (SX PsA). This amounts to, in relative terms, 0.32%–0.38% of the corresponding pulsation frequencies.

Clearly, there is much to learn about the additional modes in these stars. This may appear challenging, as the Fourier amplitudes of these modes are in the millimagnitude to submillimagnitude level. TESS, however, can help to identify bright targets with stronger extra modes that can then be easily followed up from the ground. One such example is CZ Ind, in which the presence of an O1-type mode is immediately obvious from the beating pattern in the light-curve maxima. In Figure 16 we show the frequency spectrum, full light-curve and échelle diagram of the star (top row), as well as the disentangled pulsation modes: the fundamental mode that also shows the Blazhko effect, and the extra mode (bottom row). The latter reaches 0.01–0.02 mag peak-to-peak amplitude, a signal that is within reach of even moderate-sized ground-based telescopes.

3.5. RRd Stars

Of the five RRd stars, four were identified as such earlier, based on their All-Sky Automated Survey (ASAS) light curves by independent authors (Wils & Otero 2005; Bernhard & Wils 2006; Wils 2006; Szczygieł & Fabrycky 2007a). The last one, Gaia DR2 6529889228241771264 (shortened to GDR2

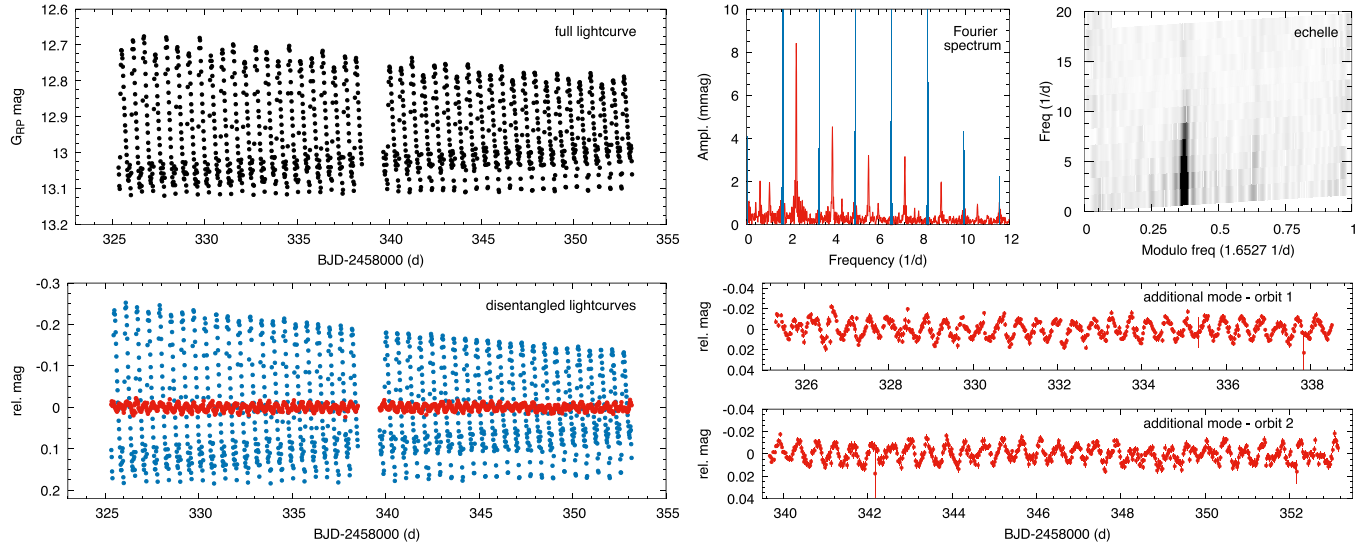

Figure 16. CZ Ind, an RRab star with a strong extra mode. Top row, from left to right: original light curve, frequency spectrum in red, with the prewhitened FM frequency components in blue, and échelle diagram. Bottom row: disentangled light curves of the fundamental mode (blue) and the extra mode (red), and only the disentangled extra mode, as seen in each of the two orbits during the sector.

71264 from here on), was cataloged as an RRc star both in the Catalina Sky Survey and in Gaia DR2 (Drake et al. 2017; Clementini et al. 2019).

Double-mode stars are valuable targets as they provide simultaneous period constraints for multiple modes that can help us determine their physical properties much more accurately than those of single-mode pulsating stars (see, e.g., Molnár et al. 2015b, 2019; Joyce et al. 2020). If we place these five stars onto the Petersen diagram, four of them fall into the main locus of RRd stars where the other Galactic RRd stars reside (Figure 17). GDR2 71264, however, lies above the main group at a period ratio of $P_{O1}/P_{FM} = 0.7486$, along with a handful of stars that belong to the Magellanic Clouds. A comparison with the nonlinear model calculations done by Szabó et al. (2004) suggests that this star is potentially a low-metallicity, high-mass, and high-luminosity RR Lyrae. An order-of-magnitude estimate for its physical parameters suggests $M \approx 0.8$–$0.9\,M_{\odot}$, L $\sim 60\,L_{\odot}$ and $Z \sim 10^{-4}$ (the latter being equivalent to $[\mathrm{Fe/H}] \approx -2.2$, assuming that $[\alpha/\mathrm{Fe}] = 0$). Parameters for the rest of the stars in the main group are more ambiguous as the mass and metallicity parameter ranges overlap, and these objects would require more detailed modeling. This can be done, but the selection and calculation of stable double-mode nonlinear models is very time-consuming (Molnár et al. 2015b); therefore, we refrained from it in this work. We also note that the physical validity of the double-mode models is not entirely settled yet (Smolec & Moskalik 2008).

3.6. Distribution of the Additional Modes in the CMD

Next, we looked at where the additional modes occur within the RR Lyrae instability strip. We plotted the stars in the Gaia CMD and marked those that feature extra modes, focusing on the main mode groups. Upon closer inspection we find two outliers, XX Dor and T Men: the first is blueward of the RRc group, whereas the latter, an RRab star, is blueward of the RRab group. Both stars are near the LMC, hence we suspect that the dust map overestimated the interstellar extinction for these stars as well, just to a lesser extent than the three other cases we have shown earlier.

The middle and right panels of Figure 18 highlight RRab stars where the f_1-type (center), f_2-type, and PD or other nearby peaks (right) appear. The sample sizes are rather low, so we cannot draw strong conclusions, but RRab stars with extra modes seem to appear more frequently at the blue part of the RRab cluster: the f_2 and PD/other modes clearly favor the RRc/RRab boundary. We marked BV Aqr, the overtone star which is potentially an aRRd star: this star is also close to the boundary and its position is similar to the normal RRd stars in the sample.

In the left panel of Figure 18 we plot the occurrence of the f_X and $f_{0.68}$ modes in the RRc and RRd stars. Here it is much more evident that the f_X modes also favor the RRc/RRab boundary. The reddest star where the mode is not detected being at $M_{\mathrm{BP-RP}} = 0.36$, from there on such extra signals show up in all RRc/RRd stars we analyzed. The f_X mode has been detected from the ground in a few globular clusters as well. We can therefore compare the distribution of the modes in the CMDs of the clusters with our results. Both in NGC 6362 and M3, the f_X modes were found to cluster toward the redder RRc and the RRd stars (Jurcsik et al. 2015; Smolec et al. 2017). This is in complete agreement with our findings and indicates that the f_X modes are not excited in the hottest and bluest RRc stars.

As we discussed before, all five RRd stars in the sample show various f_X modes but apparently none of the additional modes exhibited by RRab stars, associated with the fundamental mode.

3.7. RRd Stars and the Bailey Groups

The first phenomenological classification of RR Lyrae stars dates back to Bailey (1902), who created the groups a, b, and c, based on the asymmetry and period of the light curves, as subclasses to the much broader group of short-period variables (Class IV in the early variable classification scheme proposed by Pickering 1881). This was later transformed into the Bailey classes RRab, RRc, and RRd, based on physical arguments, referring to fundamental mode, first overtone, and double-mode pulsators.

However, the discovery of additional modes in a large portion of RR Lyrae stars, some of which may apparently be the first overtone in an otherwise RRab-type light curve, potentially complicates this scheme. Therefore, it is timely to

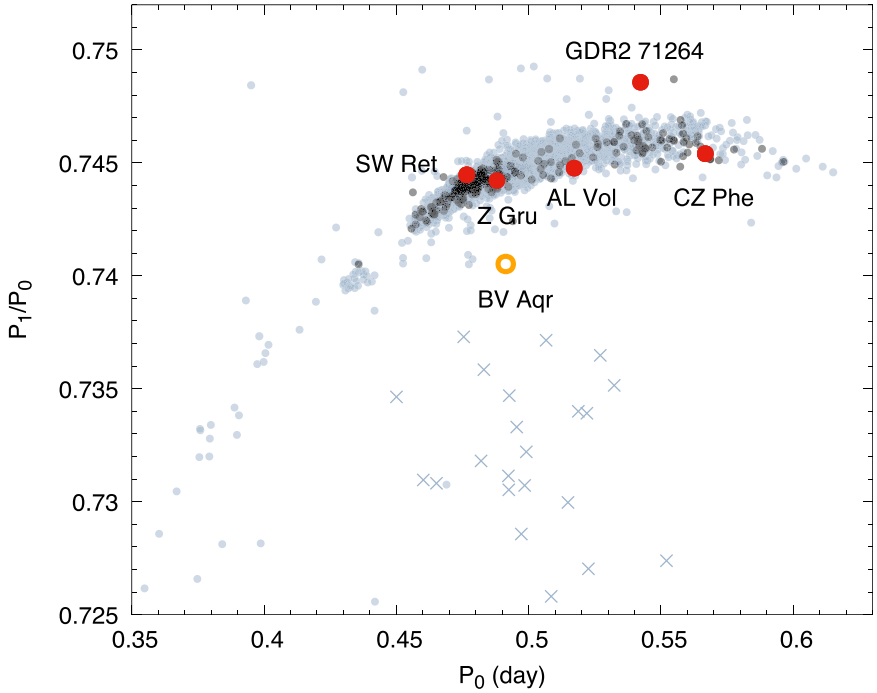

Figure 17. Petersen diagram of the five RRd stars we analyzed (red). Black dots are various field RRd stars, gray ones are OGLE stars from the bulge and the Magellanic Clouds. Sources are the same as the RRd stars collected in Molnár et al. (2015b). Crosses are anomalous RRd stars found in the Clouds (Soszyński et al. 2016).

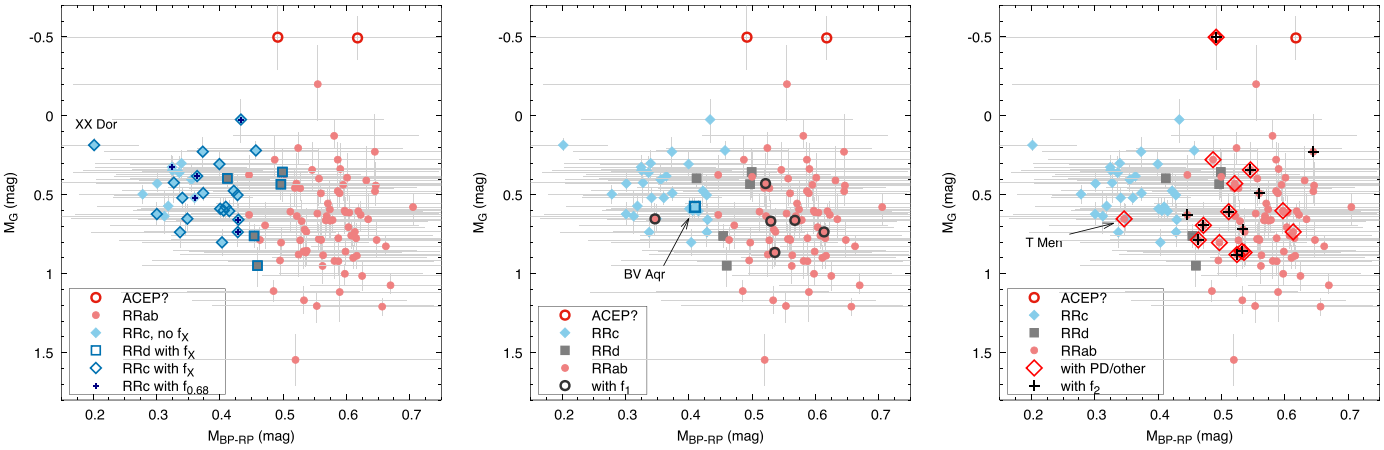

Figure 18. Distribution of the stars with additional modes within the RR Lyrae instability strip. Left: the f_X and $f_{0.68}$ modes in RRc and RRd stars. Center: the f_1-type modes in RRab stars. Right: the f_2 and PD or other type of modes in RRab stars. Two stars marked (XX Dor and T Men) had their interstellar extinction values overestimated and hence appear too blue and too bright. The third star, BV Aqr, is the extreme RRd candidate.

revisit the classical Bailey-type definitions and to reevaluate, how strict the boundaries of the different groups should be. One can argue, for example, that the RRab and RRc classes should refer to pure radial pulsators; this, however, would require the creation of subgroups or the expansion of the double-mode group, the RRd stars, to include all objects that show multiple pulsation modes. We must also consider then that this would make the RRd group very inhomogeneous. Another possibility is that the RRab and RRc groups should refer to stars that are dominated by, but not strictly limited to, the fundamental and first overtone modes, respectively. Then the RRd group should refer to stars where these two modes are both present, with amplitudes in the same order of magnitude, dominating over other, much smaller signals.

In order to test whether a criterion can be devised to separate stars dominated by one or two modes, we calculated the amplitude ratios of the various independent frequency components in our sample and normalized them by the amplitude of the strongest frequency peak. While the RRd sample size in S1 and S2 is rather small, a clear picture emerged: the five RRd stars' amplitude ratios between 30%–90%, whereas all the small additional modes are below 10%, as shown in the lower panel of Figure 19. The amplitude ratios steadily decrease toward the longer main pulsation periods, except for a single outlier, but that is also below the 10% limit. Even if we do not normalize, the separation remains, as the additional modes do not exceed 10 mmag (upper panel of Figure 19). Based on this initial sample, we are hopeful that the classical RRab, RRc, and RRd definitions can be upheld,

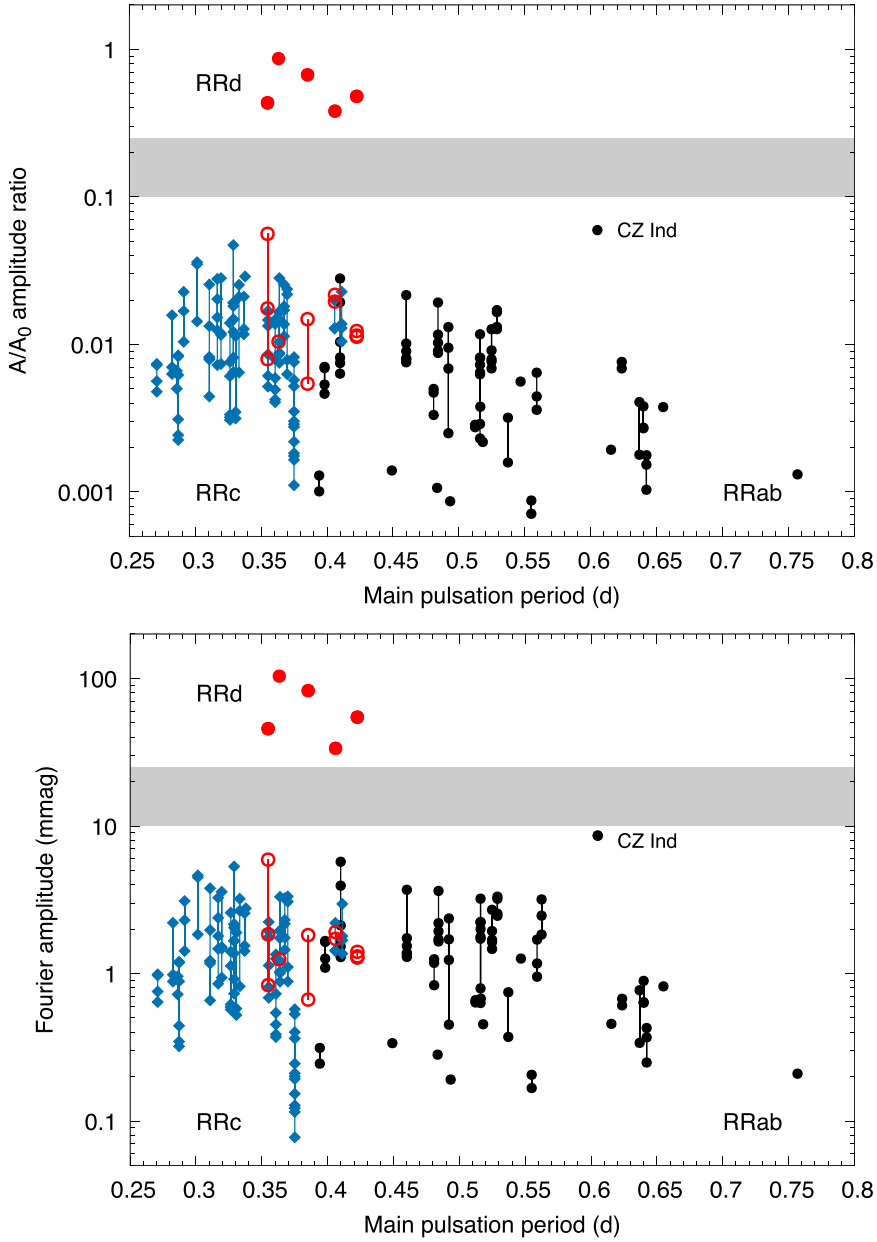

Figure 19. Amplitudes of the independent frequency components we found (bottom) and their ratios compared to the amplitude of the strongest frequency peak (top). The gray band is between 10–25 mmag and $A/A_0 = 0.10$–0.25, respectively. Black small circles are additional components in RRab stars; blue diamonds are additional components in RRc stars; red full and empty circles are the ratios between the main peaks of the two radial modes and the additional peaks and the strongest peak in RRd stars, respectively.

as this approach would also be backwards compatible with a large body of literature.

3.8. Contamination

One major issue with TESS is the low angular resolution of the images that causes the images of stars to blend or contaminate each other. While differential image photometry can mitigate this, variations of blended sources will still appear in the light curves. We found one prominent example of this effect. The Fourier spectrum of SU Hyi, as shown in Figure 20, revealed a complicated structure of peaks around the third harmonic peak. We do not expect strong additional modes to appear in this frequency range and we could not identify clear combination frequencies with the fundamental mode either. The SIMBAD and Gaia DR2 databases did not contain known variable stars close to our target. We therefore extracted the light curves of the nearby, bright stars for closer examination. We discovered that the bright star HD 10925 ($G_{\rm RP} = 7.488$ mag) is in fact a previously unknown δ Scuti variable star and it is contaminating the light curve of SU Hyi. The two strongest frequency peaks at 7.58919 and 8.03771 days^{-1} (87.838 and 93.029 μHz) are separated by 0.449 days^{-1}. This is close to, but clearly different from the separation of the modulation side peaks ($2f_m = 0.360$ days^{-1}). This indicates that the modulation is intrinsic to the RR Lyrae star, and not caused by the presence of the contaminating source.

4. Comparison with Ground-based Data and Models

TESS provides accurate but short snapshots for RR Lyrae stars. We were interested in comparing the TESS data to other

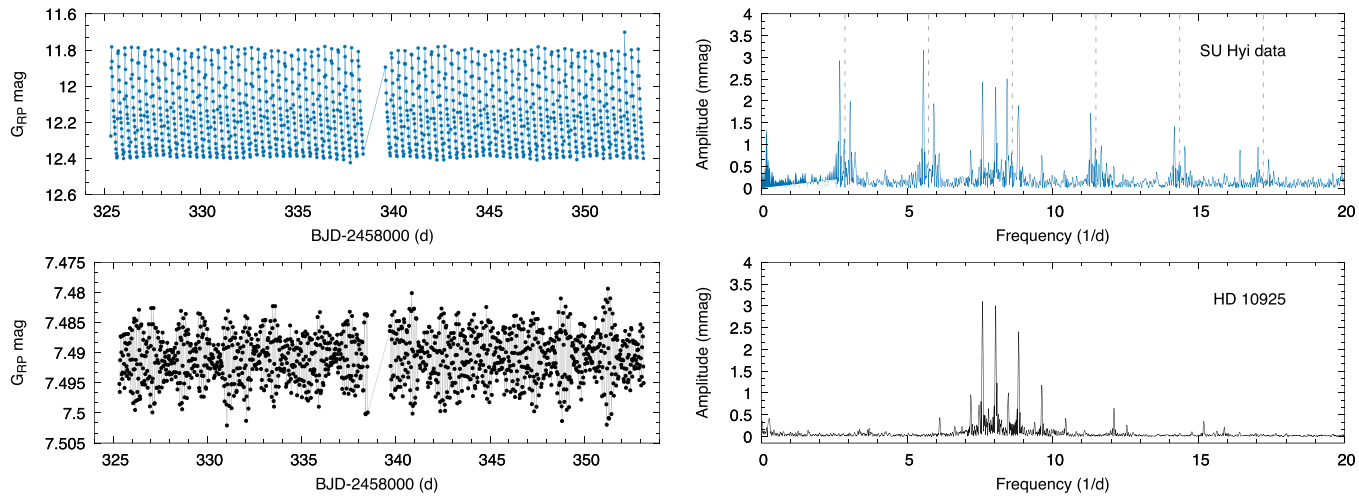

Figure 20. A bright δ Scuti contaminating an RR Lyrae star. Top row: the light-curve and Fourier spectrum of SU Hyi. Dashed lines mark the harmonic series of the pulsation peak that has been removed for clarity. The contamination appears as an extra set of peaks between 6–9 days^{-1}. Bottom row: light-curve and Fourier spectrum of the nearby bright star HD 10925. The frequency content matches the distribution of excess peaks in the spectrum of SU Hyi.

data sources that provide sparser but potentially much more extended light curves. We also compared the light-curve parameters to theoretical calculations.

4.1. KELT and Other Sources

We extracted photometry from the Kilodegree Extremely Little Telescope (KELT) observations for 33 stars from our sample. KELT uses small robotic cameras with telephoto lenses and a broad, red–pass filter to search for transiting exoplanets (Pepper et al. 2007, 2012). For some stars where KELT data were not available, we also used light curves from the public database of another exoplanet survey, SuperWASP (Wide-Angle Search for Planets, Butters et al. 2010; Paunzen et al. 2014).

Of the 33 targets, 20 stars had useful amounts of observation in the KELT database. Seven stars were too faint for KELT and we detected only scatter with no signs of pulsation in the data. We were able to detect the modulation in RV Hor and measured it to be 78.93 days long; this is almost a day shorter than the value found by Szczygieł & Fabrycky (2007b).

One of the 2 minute targets, RU Scl, was observed in 2017 and 2018 from Chile by one of the authors (F.J.H.). During 13 nights we collected more than 800 points in the Johnson–Cousins I_c filter with a 40 cm f/6.8 optimized Dall–Kirkham telescope equipped with an FLI CCD camera with 4k × 4k Kodak 16803 chip (Hambsch 2012).

For RU Scl, we were able to compare five different data sets, bearing in mind that the TESS 2 minute cadence data are not independent of the 30 minute cadence data, only sampled at a higher rate. RU Scl is a known fundamental mode Blazhko star with a modulation period of 23.9 days (Skarka 2014). From the variations of the maximum times, Li et al. (2018) marked this star as a potential binary candidate. In Figure 21, the comparison of the window functions of TESS, SuperWASP, and KELT data of RU Scl are shown. Ground-based data have better resolution, but suffer from many aliases caused by regular (daily and annual) gaps in the observations.

We detected 55 and 21 pulsation harmonics in the 2 and 30 minute data, respectively (see Figure 21), but only 30 and 9 harmonics in the SuperWASP and KELT data, respectively. After removal of the pulsation frequency, f_0, and its harmonics, kf_0, we searched for the peaks corresponding to the Blazhko modulation. We identified the side-lobe peaks up to the 55th harmonic in the 2 minute data. The modulation period corresponds to 24.06(4) days. As only one cycle was observed during the TESS observations, the period is not determined precisely and the formal error is unrealistically small. No PD features (half-integer multiples of f_0) were identified.

We also analyzed observations of the strongly modulated RRc star BO Gru. This star was also observed by F.J.H. from Chile but in the Johnson V band in 2014. We collected 2285 data points on 50 nights over a period of 58 days, giving us very dense coverage. The light curve in Figure 22 shows the same strong modulation that we observed in the TESS data. We also plotted the light curves folded with the pulsation and modulation periods: the width of the phased light curve in the bottom left indicates that both the amplitude and the phase of the pulsation experienced strong modulation. Meanwhile, the right bottom plot suggests differences between the modulation cycles. These properties can also be detected in the TESS light curve. Overall, the modulation properties of the star appear to be unchanged almost four years apart.

The stability of the modulation in BO Gru allowed us to compare the temporal evolution of the A_1 and ϕ_1 Fourier components of the two data sets directly. We determined the modulation period to be 10.2221 days, slightly longer than the TESS-only value. We found that the A_1 Fourier amplitude of the redder TESS data is 62% of the V-band A_1 amplitude, and this ratio did not change throughout the modulation cycle.

4.2. OGLE Stars

Five stars in our sample have been followed by the OGLE project. We analyzed the OGLE-IV survey data of all stars except SMC-RRLYR-0770 which was only observed in OGLE-III. Folded TESS and OGLE light curves are plotted in Figure 23. We did not detect additional mode signals in the OGLE data, so direct comparison for those is not possible. We were, however, able to determine the Blazhko periods for them from the OGLE light curves, where modulation was present.

In LMC-RRLYR-00854, we identified a stable Blazhko cycle with a period of 120.55 ± 0.10 days. LMC-RRLYR-03497, in contrast, shows multiple modulations, with the following periods: $P_{m1} = 30.418 \pm 0.014$ days, $P_{m2} = 81.80 \pm 0.06$ days,

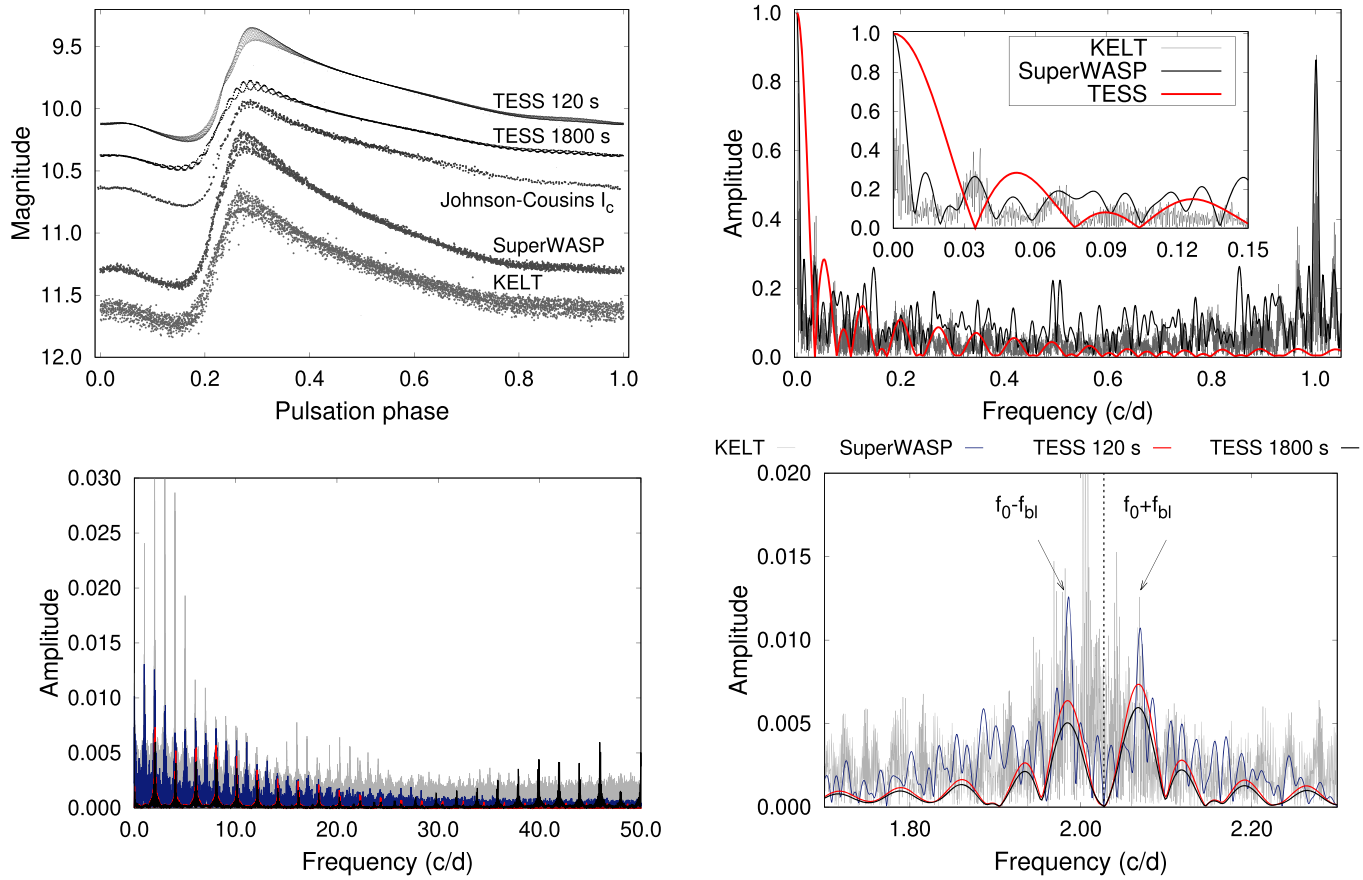

Figure 21. The comparison of the TESS Sector 2 30 minute and 2 minute cadence data to various observations taken from the ground. Light curves (upper left panel), spectral windows (upper right panel), frequency spectra (lower left panel), and the modulation side peaks around the pulsation frequency (lower right panel) in the different data sets of RU Scl are plotted, respectively.

$P_{m3} = 96.52 \pm 0.17$ days. However, we cannot rule out that the third is only a combination in frequency space, $2f_{m3} \simeq f_{m1} - f_{m2}$, and that could indicate interaction or temporal variability between the two other cycles instead of a third modulation. The data for LMC-RRLYR-23457 suggest a non-stationary Blazhko cycle with a period of 174.0 ± 0.3 days. These modulation cycles are longer than our TESS light curves and thus they are not resolved in the TESS data. The OGLE-based findings, however, reinforce that our assumption to include stars with apparently non-cyclic amplitude and phase changes over the span of the TESS data in the Blazhko category is justified. Moreover, the case of LMC-RRLYR-03497 shows that when short-term data suggest different cycle lengths from the amplitude and phase variations, it is likely a sign of multiple modulation periods in the star.

We were able to compare TESS and OGLE data for one first overtone star, SMC-RRLYR-2428. It is a Blazhko RRc star, and one of those stars for which we cannot tell with certainty whether the slow variations are due to beating with a second mode very close to the radial one, or from Blazhko-type modulation but with very asymmetric side-peak amplitudes, where one side is not detectable. Either way, the OGLE data show that the beat or modulation period, 35.401 ± 0.015 days, remained stable over the OGLE-IV observing run.

4.3. Pulsation Models

Light-curve parameters from TESS can be, in principle, compared to theoretical light curves produced with nonlinear pulsation models. One drawback is that models need to be transformed into the TESS passband first, and we cannot rely on existing models that are calculated for, e.g., the Johnson or Sloan photometric systems.

Nevertheless, as a cursory test, we compared the R_{21} and ϕ_{21} Fourier parameters to those calculated for the I band from the models of Marconi et al. (2015) for a fixed composition (Z = 0.004, Y = 0.25). These RR Lyrae models were generated using the one-dimensional nonlinear hydrodynamic model that employs time-dependent convection to iterate the pulsating envelope in time (Bono & Stellingwerf 1994).

Figure 24 displays a comparison of Fourier parameters for RR Lyrae from TESS with those for the model light curves in the I band. The comparison clearly shows the same shift in the ϕ_{21} phase difference that we observed when comparing the TESS data to the OGLE I-band values in Figure 6. However, other differences can be found as well. The calculated R_{21} values spread upward toward long periods, whereas the upper envelope of the observed values goes downward from about $\log P \gtrsim -0.15$ or $P \gtrsim 0.7$ days. Note that theoretical amplitude parameters for classical pulsators are known to be systematically larger than the observed amplitudes (Bhardwaj et al. 2017; Das et al. 2018). Similarly, phase parameters, like ϕ_{21}, display a clear dependence on adopted metal abundances in the I band (see Figure 5, Das et al. 2018). Moreover, the models do not exactly reproduce all light curves in the overlapping long-period RRc and short-period RRab range. Correcting for these shortcomings in the models would require a finer grid with

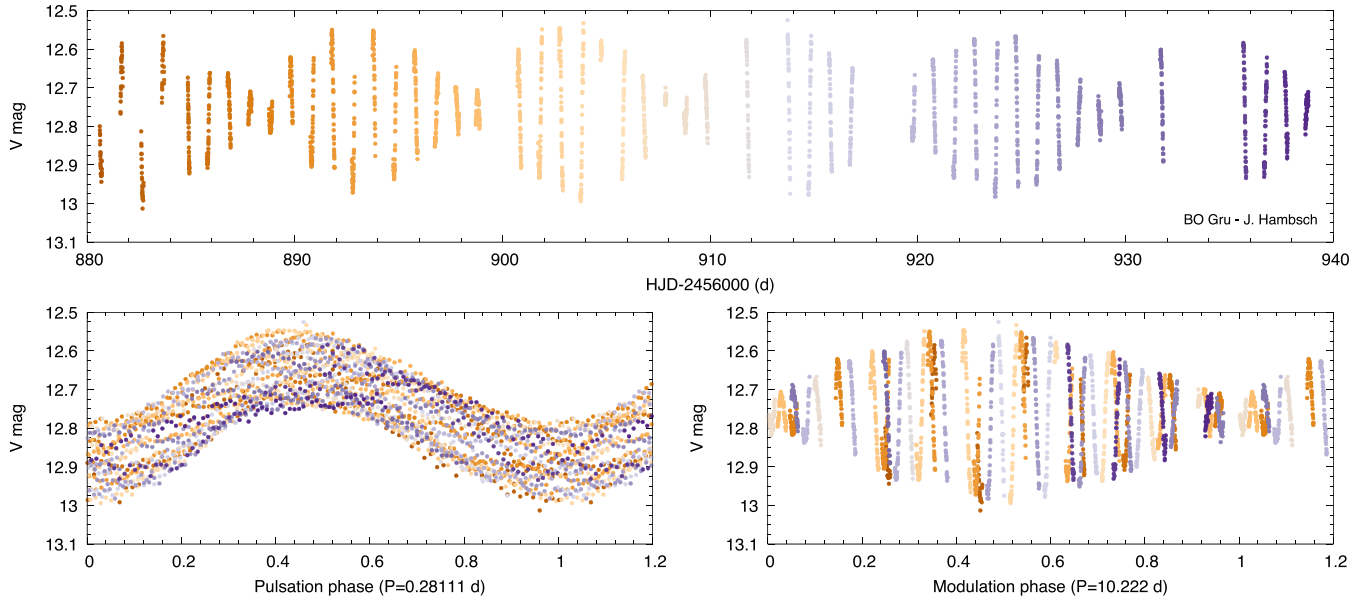

Figure 22. Ground-based observations of BO Gru, the strongly modulated RRc star. Top row: the entire light curve. Bottom row: phase curves, folded both with the pulsation and with the modulation periods. Colors follow time of the observations.

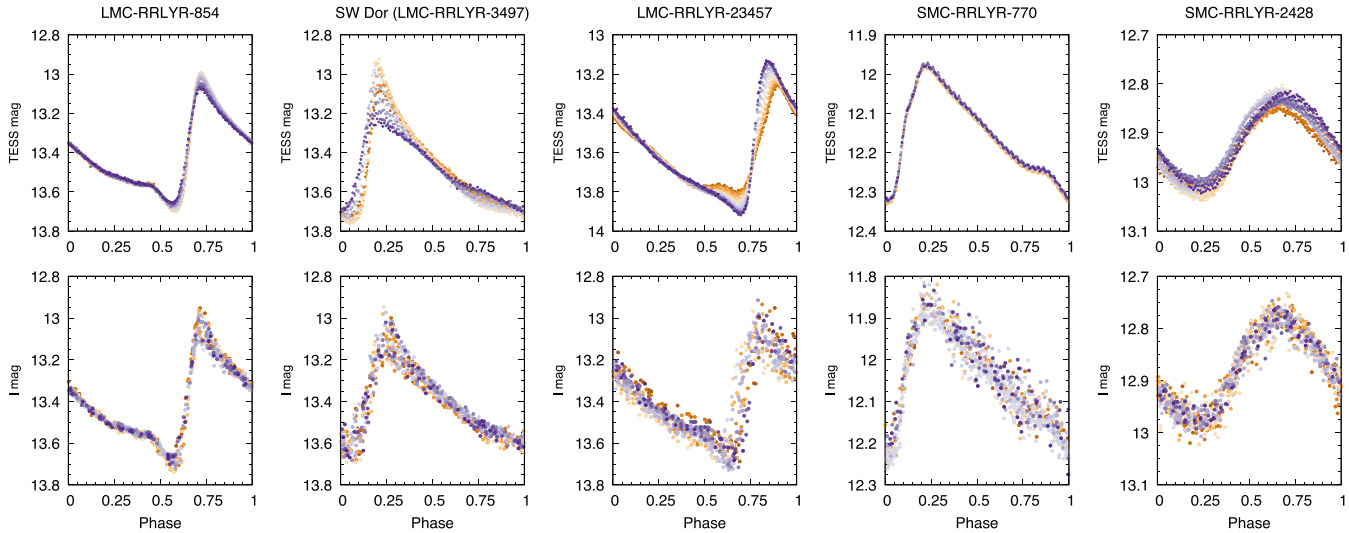

Figure 23. Comparison of the TESS (top panels) and OGLE (bottom panels) light curves for the shared targets. Color scale shows progression of time, going from orange to purple.

further fine-tuning of various input physical and convective parameters, an exercise that is beyond the scope of this study. Nevertheless, these discrepancies highlight the broader problem of reproducing observed pulsation amplitudes numerically (see, e.g., Zhou et al. 2021 for solar-like oscillations).

We must also point out that accurate comparison will indeed require transforming the luminosity curves into the TESS passband since the Fourier parameters of both Cepheid and RR Lyrae also vary with wavelength (Bhardwaj et al. 2015; Das et al. 2018). Nevertheless, the benefits are clear: the availability of precise and continuous light curves for thousands of RR Lyrae stars from TESS provides a new opportunity to constrain Blazhko models, for example. TESS light curves, in combination with data from other passbands, can be utilized very effectively to connect photometric properties to physical parameters, such as mass, metallicity, luminosity, and radius (Bellinger et al. 2020).

5. Future Prospects

By the end of our analysis, TESS has successfully finished its primary mission and has begun the first mission extension. The nearly all-sky data from the first two years constitute an incredibly rich resource for stellar astrophysics. In order to have a better understanding of the capabilities of TESS, we complemented our first light study with two tests: one aimed at assessing the performance at the faint limit of the telescope, and the other a comparison of the new, 10 minute cadence FFI data of the extended mission to the original 30 minute cadence data.

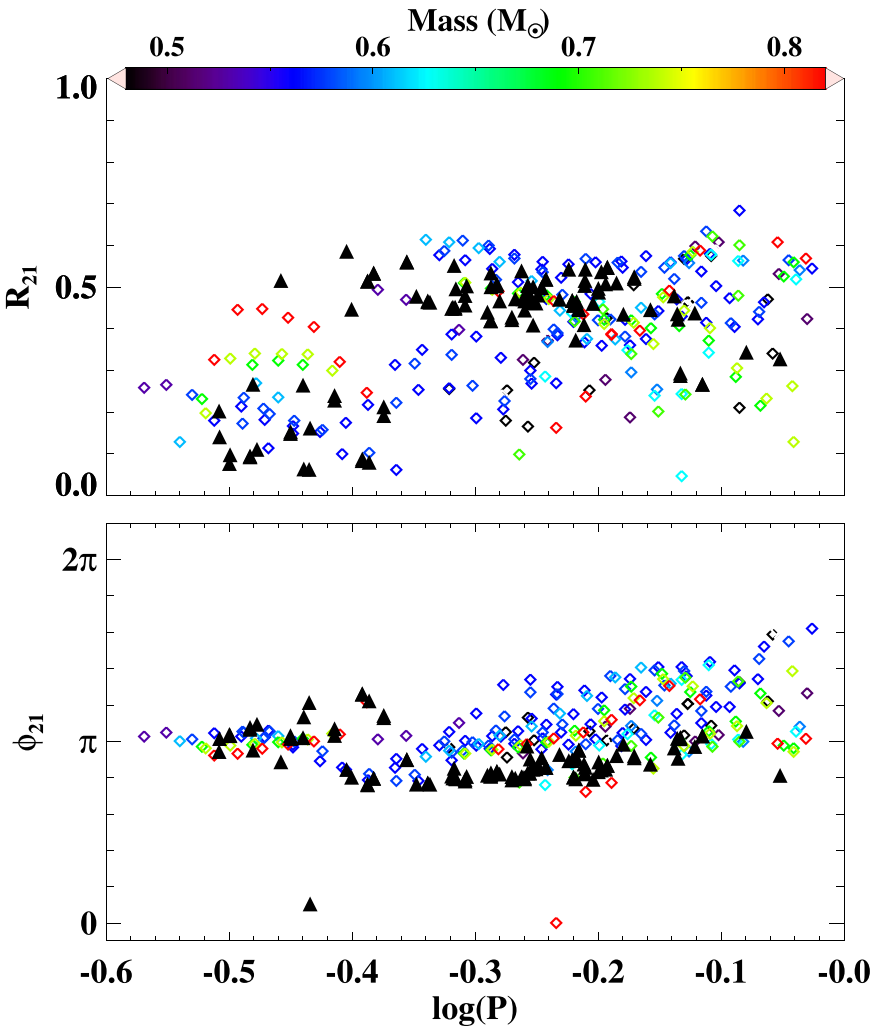

Figure 24. Comparison of lower-order Fourier parameters of TESS light curves (filled triangles) with RR Lyrae pulsation models (open squares) from Marconi et al. (2015) in *I* band. The color bar represents different stellar masses for RR Lyrae models.

5.1. Faint Targets

Kepler was able to collect useable light curves from RR Lyrae stars at the $Kp \sim 21$ mag level (Molnár et al. 2015a). Considering the 100 fold reduction in the light-correction area between the optical systems of Kepler and TESS, we should be able to recover RR Lyrae stars down to 16 magnitudes if the stellar density is low enough in the images to detect the target. Furthermore, RR Lyrae stars have a color index of $[G - G_{\rm RP}] \approx 0.3$–0.4 mag: since the Gaia G and $G_{\rm RP}$ bands closely match the Kepler and TESS passbands, respectively, they are 0.3–0.4 mag brighter in the TESS passband than in the Kepler one, pushing the faint limit further outward.

To test these assumptions, we selected two stars from Sector 2, CSS J233140.8–113458 at $G = 15.55$ mag, which we expect to produce a lower-precision but clearly recognizable light curve, and CRTS J231519.9–282651 $G = 17.26$ mag, to see if large-amplitude variations remain detectable at this level. The light curves in Figure 25 show that this is indeed the case. The former star produced a clean Blazhko RRab light curve, whereas in the latter case, only the existence of a large-amplitude, periodic, asymmetric variation is evident. However, the RRab-type variation is still clearly recognizable in the phase-folded light curve, thus mode classification will still be possible at the 17 mag level. Two short brightenings are also visible in the light curve of CSS J233140.8–113458, the brighter star, which are marked with red dashed lines. These are caused by a fainter and a brighter asteroid crossing the photometric aperture, respectively. Even with the TESS telescopes avoiding the vicinity of the ecliptic, large numbers of asteroids cross the fields of view, especially that of camera #1, closest to the ecliptic (Pál et al. 2018, 2020).

We then calculated the noise levels in the Fourier spectra of these stars to estimate if additional modes are possible to detect them. In the fainter star, the widely used detection signal-to-noise level of 4 is at 18 mmag, whereas in the brighter one it is around 5–6 mmag. Comparing these values to the Fourier amplitudes in Figure 19, we can conclude that at the 15.5 mag level we are just barely able to detect the strongest additional modes. At the 17 mag level, differentiating between RRab, RRc, and RRd stars will be possible. However, these predictions are based on well-behaved targets for which neither strong scattered light nor blending with brighter stars affected the photometry.

5.2. 10 minute Cadence Improvements

In the first mission extension of TESS, the cadence of the FFIs was changed from 30 minutes to 10 minutes. Although the increased sampling lowers the per cadence accuracy, it triples

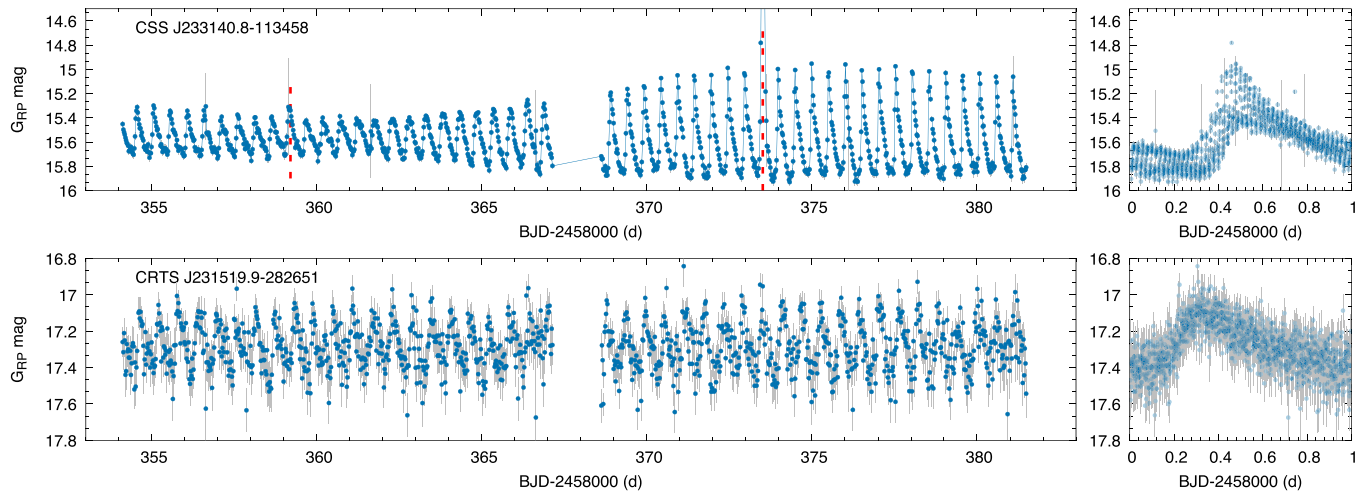

Figure 25. Two faint targets from Sector 2. Left: light curves, Right: phase-folded curves. Red dashed lines indicate flux excesses from asteroids crossing the photometric aperture.

the available frequency range. By the time we finished the various analyses detailed in this paper, TESS had already re-observed the areas of S1 and S2 during S27 and S28. We therefore compared the performance of the faster cadence for a few targets.

For the brighter targets presented, the 10 minutes sampling comes with clear advantages. In some targets, the series of the pulsation harmonics extended beyond the Nyquist frequency ($f_{\rm Ny}$) with the 30 minute cadence and thus the $f_{\rm Ny} - nf_0$ reflections of those above this limit showed up below $f_{\rm Ny}$. Furthermore, longer integration introduces phase smearing that lowers the observed amplitudes. This effect is clearly visible in the middle panel of Figure 21, where the red frequency spectrum of the 2 minute cadence has higher peaks than that of the 30 minute cadence data in black. Moreover, amplitudes are getting attenuated further near the Nyquist frequency. With the 10 minute cadence, we are not facing either of these issues. The benefits will of course start to vanish for fainter targets, where high-frequency components are lost amidst the higher noise level. For sufficiently bright targets, however, amplitudes and relative phases of higher harmonics contain useful information about the precise shape and underlying physics of the light curve beyond the usual first two $R_{\rm i1}$ and $\phi_{\rm i1}$ Fourier coefficients. Differences in the local minimum of the harmonic amplitudes and the steepness of these curves were highlighted both for RR Lyrae and Cepheid stars by Benkő et al. (2016) and Plachy et al. (2021), respectively, but are yet to be utilized further.

Another benefit is that the wider frequency range makes it possible to construct taller échelle diagrams. Finally, fast sampling allows us to track specific features such as the position and depth of the shock-wave features (humps and bumps) more accurately in the light curves themselves.

6. Conclusions

In this paper we studied an initial selection of 126 known or candidate bright RR Lyrae stars within Sectors 1 and 2 of the TESS mission, 118 of which turned out to be real pulsators. We were interested in the capabilities of the mission regarding this abundant and well-known class of high amplitude pulsating stars. A companion paper looking at Cepheid stars was recently published by Plachy et al. (2021). Our results can be summarized as follows:

1. We created differential image photometry for our targets from Sectors 1 and 2 with the FITSH software (Pál 2012). We were able to extract high-precision light curves for stars in the 9–13.5 magnitude range. We tested the limits of the data and showed that depending on the precision requirements, light curves can be recovered down to 15–17 mag brightness where the number density of Galactic RR Lyrae stars peaks (Plachy 2020).
2. Most TESS light curves are short but can be complemented with ground-based observations, especially with the considerably longer but less accurate (on a per data point basis) OGLE survey data. Comparison with nonlinear pulsation models is also promising, but luminosity variations have to be converted into the TESS passband for more detailed studies.
3. Combining very accurate light-curve data from TESS (periods and Fourier parameters) with homogeneous parallax and hence, absolute brightness and color data from Gaia EDR3 offers us the best photometric classification scheme for classical pulsators. This is especially true for the RR Lyrae regime, where the R_{i1} and ϕ_{i1} Fourier parameters of binaries as well as short-period classical and ACEPs might overlap. We identified 118 bona fide RR Lyrae stars, two ACEP candidates and six nonpulsating stars in the sample.
4. Classification based on the combined light-curve shape and parallax information was found to be very effective. This way we are able to confirm stars with unusual light curves (such as BO Gru), and are able to separate short-period ACEP candidates from genuine RR Lyrae stars.
5. We were able to detect modulation and estimate the frequency of the Blazhko effect, which is about 13% in RRc and between 48%–72% for RRab stars. The light curves are generally too short for more detailed studies of the Blazhko effect: this could be remedied by focusing on the stars within continuous viewing zones. We also showed that non-modulated RRab stars exist, but estimating the true fraction of those requires very careful data processing at this photometric accuracy.
6. While low-amplitude extra modes in RR Lyrae stars are possible to detect from the ground (see, e.g., Jurcsik et al. 2015; Netzel & Smolec 2019), space-based photometry is clearly superior in sensitivity. We detected various types

of extra signals in a large fraction of stars. We see clear differences in the distribution of extra modes compared to the bulge sample, which suggests that physical properties —likely the metallicity—are affecting mode selection.

7. In RRab stars, the extra signals can be grouped into three broad categories based on their modulo frequency ratios with the fundamental modes. However, the highest-amplitude peaks of those modes are not confined to the vicinity of the fundamental mode frequency: they may appear at very different positions in the $f_{\rm addtl} + i f_0$ combination series (where $i = -1, 0, 1, 2, 3...$). Whether all these peaks are simply different modes or combination peak amplitudes are also affected by other effects, shifting the position of the highest peak in the spectrum, is a question for future studies.
8. We find that stars with extra modes are more frequent toward the center of the instability strip and the RRab/RRc interface. RRc stars without the f_X mode can be found toward the blue edge of the instability strip, but the mode is present in all of our redder RRc and RRd stars. We describe the distribution in RRab stars for the first time and show that they are more prevalent among bluer, hotter fundamental mode pulsators.
9. So far, RRab and RRc stars with low-amplitude extra modes can be clearly separated from bona fide double-mode stars based on relative mode amplitudes: we detect an empty region between 10%–25% amplitude ratios relative to the main radial mode. We propose to continue to use the classical Bailey scheme, with RRab, RRc, and RRd classes referring to the *dominant* pulsation mode(s) of stars instead of the types of *observed* modes.

While it is not the perfect instrument to study RR Lyrae stars, TESS offers great potential in many respects. We will be able to build up a large and near-homogeneous database of high-precision light curves for thousands of bright RR Lyrae stars for which spectroscopic and/or multicolor photometric data already exist or are relatively easy to obtain (see, e.g., Crestani et al. 2021a, 2021b). Derivation of a well-calibrated photometric metallicity relation, for example, would be very beneficial. This will also undoubtedly help in disentangling the new phenomena we observe, such as the origin and the suspected metallicity dependence of the extra modes. This could also be complemented with data from globular clusters, either via ground-based campaigns, as was done for M3 (Jurcsik et al. 2015), or via processing the globular cluster data obtained in the K2 mission (see, e.g., Plachy et al. 2017c; Wallace et al. 2019).

A larger survey of nearby RR Lyrae stars out to 5–10 kpc, covering most of the sky, and combined with parallaxes would also be a fantastic resource. The synergy between Gaia and TESS will make it possible to build up the cleanest sample, devoid of binaries and rotational variables, but preserving unusual or unique RR Lyrae light curves. Furthermore, a thorough search for ACEPs that may be hiding under different classifications at the moment will provide the opportunity to study these intriguing objects in more detail and to construct the first Galactic period–luminosity relation for them. Finally, an unexpected synergy may be the ability to map the amount of interstellar dust in the Galaxy in directions that are otherwise difficult to probe, such as in front of the Magellanic Clouds, through RR Lyrae stars.

This paper includes data collected by the TESS mission. Funding for the TESS mission is provided by the NASA Science Mission Directorate. This work has made use of data from the European Space Agency (ESA) mission Gaia, processed by the Gaia Data Processing and Analysis Consortium (DPAC). Funding for the DPAC has been provided by national institutions, in particular the institutions participating in the Gaia Multilateral Agreement.

L.M. was supported by the Premium Postdoctoral Research Program of the Hungarian Academy of Sciences. The research leading to these results has received funding from the LP2012-31, LP2014-17 and LP2018-7 Lendület grants of the Hungarian Academy of Sciences and from the "SeismoLab" KKP-137523 Élvonal and NN-129075 grants of the Hungarian Research, Development and Innovation Office (NKFIH). The work reported on in this publication has been partially supported by COST Action CA18104: MW–Gaia.

A.P. acknowledges the MIT Kavli Center and the Kavli Foundation for their hospitality during stays at MIT, and the NASA contract number NNG14FC03C. A.B. acknowledges a Gruber fellowship 2020 grant sponsored by the Gruber Foundation and the International Astronomical Union and is supported by the EACOA Fellowship Program under the umbrella of the East Asia Core Observatories Association, which consists of the Academia Sinica Institute of Astronomy and Astrophysics, the National Astronomical Observatory of Japan, the Korea Astronomy and Space Science Institute, and the National Astronomical Observatories of the Chinese Academy of Sciences. M.J. was supported by the Lasker Data Science Postdoctoral Fellowship of the STScI and by the Research School of Astronomy and Astrophysics at the Australian National University and funding from Australian Research Council grant No. DP150100250. She was likewise supported by generous visitation funding from Konkoly Observatory through the LP2014-17 Lendület grant. C.C.N. thanks the funding from Ministry of Science and Technology (Taiwan) under the contract 109–2112–M–008–014–MY3. E. P. was supported by the János Bolyai Research Scholarship of the Hungarian Academy of Sciences. Z.P. acknowledges support by the Deutsche Forschungsgemeinschaft (DFG, German Research Foundation)—Project-ID 138713538—SFB 881 ("The Milky Way System," subproject A11). R.S. was supported by the National Science Center, Poland, Sonata BIS project 2018/30/E/ST9/00598. M.S. acknowledges the financial support of the Operational Program Research, Development and Education—Project Postdoc@MUNI (No. CZ.02.2.69/0.0/0.0/16_027/0008360) and the MSMT Inter Transfer program LTT20015. Funding for the Stellar Astrophysics Centre is provided by The Danish National Research Foundation (grant agreement no. DNRF106). We gratefully acknowledge the grant from the European Social Fund via the Lithuanian Science Council (LMTLT) grant No. 09.3.3-LMT-K-712-01-0103.

This research has made use of the SIMBAD database, operated at CDS, Strasbourg, France, the International Variable Star Index (VSX) database, operated at AAVSO, Cambridge, Massachusetts, USA, and NASA's Astrophysics Data System (ADS).

Facilities: TESS (Ricker et al. 2015), Gaia (Gaia Collaboration et al. 2016), SIMBAD (Wenger et al. 2000), VSX

Software: fitsh (Pál 2012), lightkurve (Barentsen et al. 2019), Period04 (Lenz & Breger 2005), gnuplot, mwdust (Bovy et al. 2016), galpy (Bovy 2015), echelle_toggler (Joyce 2021), Astropy (Astropy Collaboration et al. 2013, 2018)

Appendix A
List of Targets, Light Curves, and Classification Results

Below we list the stars we identified as RR Lyrae or candidate ACEP stars as well as updated classifications for some of the stars that were identified as RR Lyrae at some point. In Figure 26 we provide a map showing the positions of the RR Lyrae targets in the sky. Since target selection was based largely on the Gaia DR2 catalog, we did not update the naming scheme with EDR3 identifiers. Nevertheless, we checked the `gaiaedr3.dr2_neighbourhood` cross match catalog if the identifiers were carried into the new catalog. The only star in the sample whose identification changed is VW Scl, which is named DR2 49854559940 38393088 and EDR3 4985455998336183168 in the two catalogs, respectively.

The tables in the Appendix contain the following information:

1. the lists of stars identified as RRab, RRc, RRd stars or ACEP candidates (Tables 1, 2, 3 and 4);
2. the list of stars identified as other types of variable stars (Table 5);
3. a sample table of the TESS differential image photometry data (Table 6, this table is available online in its entirety);
4. Blazhko identifications and periods (Table 7);
5. variation periods, distances, calculated absolute magnitudes and insterstellar extinction values (Table 8);
6. RVs and calculated U, V W velocity components (Table 9); and
7. additional modes and signals identified (Table 11).

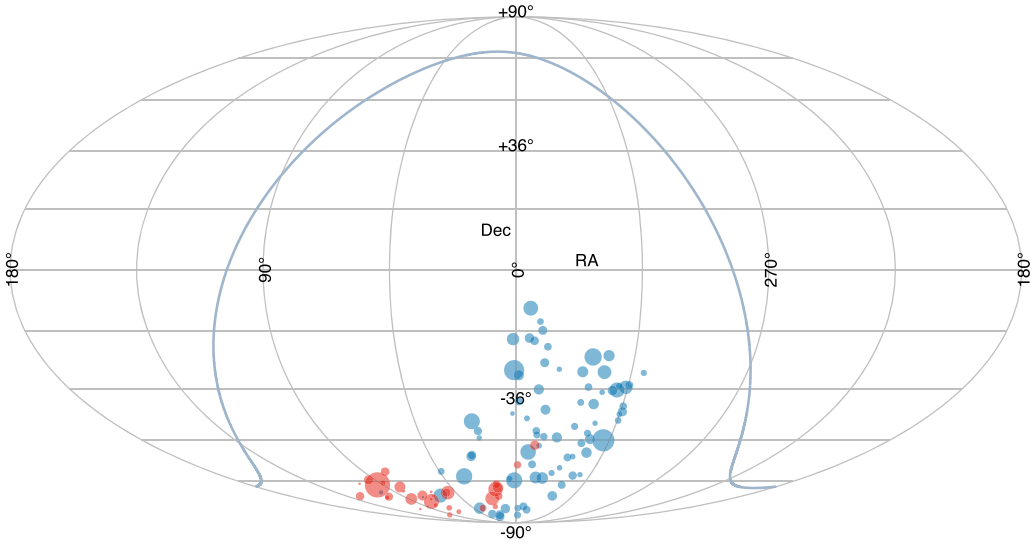

Figure 26. Positions of the RR Lyrae targets in the sky. The blue line is the Galactic plane. Blue dots are single-sector targets, red dots were observed in both S1 and S2. Sizes correspond to brightness.

Table 1
Stars Identified as RRab Type in This Study

Gaia DR2 ID	Name	Sector	R.A.$_{2000}$	Decl.$_{2000}$	G_{RP} (mag)	G (mag)
2309225008197193856	WW Scl	S2	1.50821	−36.90425	13.071	13.475
2313783205448950784	TW Scl	S2	358.67366	−33.48136	12.475	12.836
2329707050101123712	UZ Scl	S2	350.69599	−30.11941	11.993	12.369
2334529752915355520	TX Scl	S2	358.84280	−26.30201	11.986	12.413
2336550174250087936	RU Scl	S2	0.70068	−24.94538	9.991	10.392
2385090584663565696	V356 Aqr	S2	348.95810	−23.00365	12.247	12.612
2394898640700233600	OW Aqr	S2	353.07486	−17.39756	12.276	12.645
2408425936552330880	V360 Aqr	S2	350.12811	−14.79922	12.212	12.586
2409376704872793344	HQ Aqr	S2	351.05487	−12.63230	12.699	13.068
2414817603803476864	UU Cet	S2	1.02150	−16.99767	11.569	11.986
2438710609949867776	BR Aqr	S2	354.63709	−9.31878	11.065	11.538
4630819719774282624	SU Hyi	S1	25.62702	−80.00928	12.137	12.501
4631934555845355136	RW Hyi	S1	22.80129	−78.48571	12.255	12.682
4643606391466365824	TW Hyi	S1–S2	34.87803	−73.56596	12.614	13.014
4650753560652926976	LMC–RRLYR–23457	S1–S2	87.79268	−72.32250	13.588	14.040
4651573315306993920	T Men	S1–S2	77.48499	−71.64462	13.231	13.686
4652488727438230144	SZ Men	S1–S2	70.12580	−73.43823	12.916	13.290
4655243519513497728	BRIGHT–LMC–RRLYR–3	S1–S2	75.75559	−69.15043	13.255	13.712
4656309186747326336	LMC-RRLYR-854	S1–S2	71.58467	−68.42491	13.395	13.801
4660942838001474304	RT Dor	S1–S2	82.43608	−64.28667	13.380	13.797
4661506200297885184	LMC–RRLYR–03497	S1	75.52410	−67.28239	13.466	13.858
4662161543577035136	ASAS J045426–6626.2	S1–S2	73.61060	−66.43694	12.057	12.472
4662259606266850944	SX Dor	S1–S2	75.88367	−65.71618	13.606	13.989

Table 1
(Continued)

Gaia DR2 ID	Name	Sector	R.A.$_{2000}$	Decl.$_{2000}$	G_{RP} (mag)	G (mag)
4668759884616161536	TU Ret	S1–S2	65.39580	−66.66921	13.343	13.719
4672142016741937152	X Ret	S1–S2	51.33413	−65.05508	11.325	11.717
4675881215270421376	⋯	S1–S2	62.93973	−64.67200	13.433	13.877
4685757887726594816	SMC-RRLYR-770	S1	11.23326	−73.88076	12.151	12.587
4705269305654137728	AG Tuc	S1–S2	13.72244	−66.70802	12.491	12.941
4709830423483623808	W Tuc	S1–S2	14.54050	−63.39574	11.093	11.579
4710156463040888192	AE Tuc	S1–S2	12.50263	−62.63541	11.898	12.340
4720955591371097984	RV Hor	S1	42.58549	−64.26136	12.959	13.319
4728532703955609728	⋯	S2	43.94307	−55.93621	12.649	13.019
4758746729436076544	⋯	S1–S2	87.88546	−60.69212	12.945	13.377
4760456779256739968	ASAS J052122-6221.4	S1–S2	80.33938	−62.35685	11.803	12.247
4764459551334687744	NSV 1856	S1–S2	77.16111	−56.04920	12.281	12.623
4918121665731513728	UZ Tuc	S1	3.92580	−58.88359	12.741	13.118
4929368054776557184	DR Dor	S2	22.91941	−49.95530	12.367	12.681
4982010850448460160	CS Phe	S2	17.45619	−44.31485	12.929	13.310
4984655725669340544	TZ Phe	S2	17.49324	−42.12887	12.403	12.797
4985455994038393088*	VW Scl	S2	19.56251	−39.21262	10.833	11.238
5211923198582228224	AV Men	S1–S2	94.78280	−78.58565	12.946	13.370
5262046772597317376	ASAS J065818–7411.7	S1–S2	104.57327	−74.19496	13.480	13.967
5281881584407284352	NSV 3229	S1–S2	101.91481	−66.99758	12.394	12.800
5479480350950961536	⋯	S1–S2	104.05999	−60.94579	13.494	13.952
5481339590753150208	ST Pic	S1–S2	93.50474	−61.47306	9.031	9.405
6353053196895087488	TT Oct	S1	357.63569	−78.68247	12.598	13.045
6378877082899249664	AR Oct	S1	348.06084	−74.57959	⋯	12.892
6380659528686603008	BK Tuc	S1	352.38917	−72.54446	12.417	12.929
6398671998754509056	NSV 14009	S1	331.22482	−66.58247	12.073	12.484
6409071321466282752	ASAS J215601–6129.2	S1	329.00429	−61.48663	12.433	12.803
6458861949615378688	DE Ind	S1	325.23742	−57.57875	12.344	12.699
6459713658809674880	CZ Ind	S1	321.13855	−57.20120	12.927	13.333
6483680332235888896	V Ind	S1	317.87415	−45.07492	9.621	10.049
6492356127518044800	YY Tuc	S1	347.75242	−58.33545	11.639	12.072
6504972134389792128	EP Tuc	S1	338.61161	−56.59037	12.790	13.189
6508563379883711616	UW Gru	S1	335.05459	−54.55809	12.874	13.324
6519995861275291008	RW Gru	S1	340.52903	−44.15357	12.005	12.857
6526559499016401408	RV Phe	S1	352.13134	−47.45368	11.497	11.924
6526839462163012352	NSV 14530	S1–S2	350.69425	−46.69239	12.126	12.520
6535970906228369024	AQ Gru	S2	350.57517	−42.09014	12.481	12.868
6537939405704263936	CN Scl	S2	355.09552	−38.31626	12.834	13.310
6553439603373054720	CV Scl	S2	347.37736	−35.78809	11.987	12.373
6558308790617955584	AO Ind	S1	330.12103	−50.49433	12.811	13.141
6564274294034705664	RT Gru	S1	327.99369	−45.98528	12.447	12.831
6565527904791301504	RR Gru	S1	324.51483	−44.68671	12.035	12.418
6566136523133385344	EG Gru	S1	326.58082	−42.84713	12.630	13.028
6570158089992425984	NSV 14073	S1	333.37160	−40.72565	12.614	13.008
6591208755501548672	NSV 13885	S1	327.33249	−34.20538	11.951	12.347
6611282775511288832	V354 Aqr	S2	343.19796	−24.70381	12.932	13.299
6616811807170380928	AD PsA	S2	330.84827	−29.48122	12.450	12.844
6625215584995450624	AE PsA	S1	333.98230	−25.37725	11.814	12.256
6774717933372604544	XZ Mic	S1	314.72826	−38.94154	12.668	13.050
6775336855339787008	ASAS J210032–3708.3	S1	315.13410	−37.13860	12.835	13.260
6778621508888695296	ASAS J205705–3621.8	S1	314.27104	−36.36336	12.179	12.639
6780267993191790464	⋯	S1	314.60933	−34.82025	12.523	12.992
6785264788206270336	SX PsA	S1	324.93053	−30.89415	12.856	13.199
6787617919184986496	Z Mic	S1	319.09467	−30.28421	11.034	11.497
6788454544456587520	⋯	S1	315.81924	−29.55231	11.333	11.818
6788756669633846016	⋯	S1	318.61906	−29.17779	12.767	13.191
6800126375781155072	ASAS J204034–2540.5	S1	310.14142	−25.67529	12.820	13.274
6805869292514475264	ASAS J205048–2436.4	S1	312.70002	−24.60623	12.250	12.647
6817857748827529344	DL Cap	S1	324.75848	−21.21283	11.746	12.181

Note. Parameters are based on the Gaia DR2 catalog. Gaia source identifiers are identical in EDR3 for all stars except for VW Scl (EDR3 4985455998336183168), marked with asterisk.

(This table is available in machine-readable form.)

Table 2
Stars Identified as RRc type in This Study

Gaia DR2 ID	Name	Sector	R.A.$_{2000}$	Decl.$_{2000}$	G_{RP} (mag)	G (mag)
2394631356295692032	NSVS 14632323	S2	354.96391	−16.74045	12.077	12.354
2399010298791985280	ASAS J231209–1855.4	S2	348.0382	−18.92395	12.474	12.699
4628067852624828672	⋯	S1–S2	69.47026	−76.08053	13.009	13.343
4633341282190404864	SX Hyi	S1	31.91403	−77.81319	12.304	12.614
4643476198121275648	BB Hyi	S2	38.32818	−73.61193	11.745	12.021
4655249601190389632	XX Dor	S1–S2	74.80703	−69.59513	11.01	11.390
4659096066472534272	ASAS J055122–6812.7	S1–S2	87.84083	−68.2122	11.664	11.960
4669338159011904768	NSV 1432	S2	59.55251	−66.49459	11.217	11.523
4687291397189729536	SMC-RRLYR-2428	S1–S2	20.75702	−72.57326	12.927	13.196
4692528057537147136	AM Tuc	S1–S2	19.62798	−67.91817	11.274	11.618
4718233887776006400	IY Eri	S2	31.86723	−57.86955	10.77	11.038
4902647036002699136	⋯	S1–S2	13.12956	−61.17504	12.421	12.650
4917277962356593664	⋯	S2	23.54856	−50.44242	12.107	12.404
4918030715504071296	AO Tuc	S1	1.02651	−59.48524	10.849	11.148
5280964179391935616	⋯	S1–S2	104.97554	−67.4398	13.01	13.345
5285349822037246464	⋯	S1	100.86232	−64.91099	13.068	13.364
5482545510194122112	⋯	S1–S2	94.11186	−59.36168	12.221	12.479
5495625579691991424	⋯	S1–S2	91.33735	−58.00886	13.330	13.597
6379606226611647744	⋯	S1	357.91003	−73.57293	12.688	12.393
6491783148816832256	⋯	S1	343.4942	−58.57467	11.677	11.913
6501050653153411712	EP Gru	S1	350.98926	−53.30305	12.418	12.710
6511489936239739904	ASAS J221039–5049.8	S1	332.66325	−50.82966	12.394	12.673
6523414998837956736	⋯	S1	353.69271	−48.90546	10.964	11.264
6527714432898901248	ASAS J231412–4648.9	S2	348.54831	−46.81549	12.841	13.067
6541769554459131648	BO Gru	S1	346.7444	−43.9108	12.558	12.774
6585414123064537344	ASAS J213826–3945.0	S1	324.60764	−39.74893	12.942	13.252
6611919706276933376	⋯	S1	332.91231	−33.71359	12.645	12.887
6784648718097899520	ASAS J212331–3025.0	S1	320.88066	−30.41588	12.06	12.437
6800564393726439552	⋯	S1	314.68935	−28.9718	12.343	12.697
6811546934337150464	YZ PsA	S1	325.52594	−25.47484	11.28	11.563
6820039248616386688	BV Aqr	S1	330.72498	−21.52568	10.592	10.866

(This table is available in machine-readable form.)

Table 3
Stars Identified as RRd Type in This Study

Gaia DR2 ID	Name	Sector	R.A.$_{2000}$	Decl.$_{2000}$	G_{RP} (mag)	G (mag)
4672117758766686720	SW Ret	S1–S2	52.08425	−64.97716	12.373	12.723
5271444195402177792	AL Vol	S1–S2	124.03922	−66.74651	12.323	12.699
6521271603997336832	CZ Phe	S1–S2	359.09074	−53.48948	12.514	12.851
6529889228241771264	⋯	S2	350.10878	−43.35176	12.578	12.904
6562909314771450368	Z Gru	S1	323.65454	−49.12469	11.966	12.289

(This table is available in machine-readable form.)

Table 4
Stars Identified as ACEP Candidates

Gaia DR2 ID	Name	Sector	R.A.$_{2000}$	Decl.$_{2000}$	G_{RP} (mag)	G (mag)
6508871277499009664	ASAS J221052-5508.0	S1	332.71736	−55.13313	12.279	12.686
6785264788206270336	SX PsA	S1	324.93053	−30.89415	12.856	13.199

(This table is available in machine-readable form.)

Table 5
Stars Erroneously Identified as RR Lyrae Stars in Previous Studies

Gaia DR2 ID	Name	Period (days)	Sector	Type	D (pc)	σD (pc)	M_G	σM_G
4756456588457054848	UW Dor	0.33854	S1	EW	559	$+3.4/-3.2$	4.437	0.023
4767858592749306240	ASAS J055322-5417.9	0.39370	S1-S2	EW/EB	839.4	$+11.0/-11.6$	3.075	0.041
4998159961839894656	UY Scl	0.36436	S2	EW/EB	187.4	$+1.0/-0.9$	5.252	0.023
6459704308665358848	⋯	0.36792	S1	ROT?	87.6	$+0.1/-0.1$	7.205	0.005
6559141705035584768	CRTS J215543.7-500050	30.3/2.4523	S1	ROT/EB	1469.8	$+32.6/-25.6$	2.567	0.045
6609938008366400256	ASAS J225559-2709.9	0.31037	S2	ROT?	106.8	$+0.2/-0.2$	7.097	0.007

(This table is available in machine-readable form.)

Table 6
Sample Table of the FITSH Differential Image Photometry of the FFI Targets

Name	BJD (days)	$G_{\rm RP}$ (mag)	$\delta\, G_{\rm RP}$ (mag)	Flux (e/s)	$\delta\, F$ (e/s)	$\overline{F_{\rm bg}}$ (e/s)	$\delta\, \overline{F_{bg}}$ (e/s)
ad-psa	2458325.323520	12.5119	0.0019	1626.50	2.85	0.18	0.62
ad-psa	2458325.344350	12.5230	0.0019	1609.88	2.82	0.06	0.61
ad-psa	2458325.365180	12.5294	0.0017	1600.49	2.56	0.01	0.55
ad-psa	2458325.386020	12.5389	0.0019	1586.48	2.77	0.01	0.60
ad-psa	2458325.406850	12.5537	0.0021	1564.98	2.99	0.16	0.66
ad-psa	2458325.427680	12.5689	0.0020	1543.29	2.87	0.29	0.63
ad-psa	2458325.448520	12.5863	0.0021	1518.67	2.98	0.31	0.65
ad-psa	2458325.469350	12.6099	0.0024	1486.03	3.24	0.29	0.72

Note. The table contains magnitudes, fluxes and average background fluxes from the sky annulus. The entire table is available online.

(This table is available in its entirety in machine-readable form.)

Table 7
Blazhko Identifications in the RRab Sample, Plus the Two ACEP (Candidate) Stars

ID	Blazhko	Period (days)	ID	Blazhko	Period (days)
DR Dor*	BL (new)	long	AR Oct*	BL?	
RT Dor	BL (new)	long	TX Scl	BL?	
SU Hyi	BL (new)	5.55 days	W Tuc*	BL?	
AO Ind*	BL (new)	>30 d	ASAS J065818–7411.7	BL?	
DE Ind*	BL (new)	long	GDR2 4758746729436076544	BL?	
T Men*	BL (new)	≈19 days	NSV 14530	BL?	
SZ Men*	BL (new)	long	RR Gru	contam	
AD PsA*	BL (new)	long	V Ind	contam	
UZ Scl*	BL (new)	long	TT Oct	contam	
VW Scl	BL (new)	long	AE PsA*	contam	
AE Tuc	BL (new)	long	WW Scl	contam	
BK Tuc	BL (new)	long	AG Tuc	contam	
ASAS J205048-2436.4	BL (new)	long	TW Scl	contam	
GDR2 4728532703955609728*	BL (new)	≈24 days	ASAS J210032–3708.3	contam	
GDR2 5479480350950961536	BL (new)	10.0 days	GDR2 6788756669633846016	contam	
LMC–RRLYR–23457*	BL (new)	long	BRIGHT-LMC-RRLYR–3	contam	
LMC–RRLYR–854*	BL (new)	long	HQ Aqr	⋯	
NSV 13885	BL (new)	long	DL Cap	⋯	
NSV 14009	BL (new)	long	UU Cet	⋯	
NSV 14088	BL (new)	long	UW Gru	⋯	
RW Gru	BL (new per)	24 days	TW Hyi	⋯	
RV Hor*	BL (new per)	78.93 days	AV Men*	⋯	
NSV 1856*	BL (new per)	19.52 days	RV Phe	⋯	
OW Aqr*	BL	(172.5 days)	TZ Phe	⋯	
V354 Aqr*	BL	(181.2 days)	TU Ret	⋯	
V356 Aqr	BL	(41.7 days)	CV Scl	⋯	
V360 Aqr*	BL	(54.4 days)	UZ Tuc	⋯	
RT Gru*	BL	(86.9 days)	YY Tuc	⋯	
RW Hyi	BL	(135.2 days)	ASAS J052122-6221.4	⋯	
CZ Ind*	BL	(133.4 days)	ASAS J045426–6626.2	⋯	
Z Mic	BL	(?)	ASAS J204034–2540.5	⋯	
XZ Mic	BL	(85.7 days)	ASAS J205705–3621.8*	⋯	
CS Phe*	BL	(62.5 days)	ASAS J215601–6129.2	⋯	
ST Pic	BL	(117.9 days)	GDR2 4675881215270421376	⋯	
X Ret*	BL	(160.6 days)	GDR2 6780267993191790464	⋯	
CN Scl	BL	(1271 days)	GDR2 6788454544456587520	⋯	
RU Scl*	BL	(23.9 days)	NSV 3229	⋯	
EP Tuc	BL	(63 days)	NSV 14073	⋯	
LMC–RRLYR–3497*	BL	(80.9 days)	SMC–RRLYR–770	⋯	
BR Aqr	BL?				
AQ Gru*	BL?		SX PsA* (ACEP candidate)	BL (new)	long
EG Gru*	BL?		ASAS J221052-5508.0 (ACEP)	⋯	

Note. Notation: BL indicates a known Blazhko star, with the literature modulation period listed in parentheses. BL (new) indicates newly detected modulation in the TESS light curve. BL (new per) indicates a new modulation period detected in a known Blazhko star. Asterisk indicates presence of low-amplitude extra modes.

(This table is available in machine-readable form.)

Table 8
Periods, Distances, Calculated Absolute Magnitudes and Absorption Coefficients of the Pulsating Star Targets

Gaia DR2 ID	Name	Period (days)	Distance (pc)	σD (pc)	M_G (mag)	σM_G (mag)	M_{BP} (mag)	σM_{BP} (mag)	M_{RP} (mag)	σM_{RP} (mag)	A_g (mag)
2309225008197193856	WW Scl	0.78492	4033	+279/−237	0.392	0.149	0.602	0.179	0.001	0.165	0.042
2313783205448950784	TW Scl	0.61678	2525	+129/−120	0.780	0.119	1.003	0.154	0.444	0.135	0.034
2329707050101123712	UZ Scl	0.44912	2486	+237/−178	0.410	0.199	0.628	0.244	−0.003	0.228	0.000
2334529752915355520	TX Scl	0.72779	2114	+84/−86	0.775	0.097	0.988	0.124	0.373	0.111	0.000
2336550174250087936	RU Scl	0.49336	788	+18/−16	0.826	0.060	1.105	0.081	0.443	0.081	0.000
2385090584663565696	V356 Aqr	0.55459	2040	+82/−66	0.916	0.097	1.084	0.149	0.589	0.122	0.141
2394631356295692032	NSVS 14632323	0.35554	2114	+84/−79	0.737	0.093	0.885	0.117	0.456	0.104	0.000
2394898640700233600	OW Aqr	0.65519	2676	+157/−108	0.278	0.127	0.471	0.181	−0.016	0.152	0.169
2399010298791985280	ASAS J231209-1855.4	0.30794	2935	+138/−164	0.360	0.118	0.476	0.135	0.139	0.127	0.000
2408425936552330880	V360 Aqr	0.62358	2366	+138/−91	0.736	0.113	0.957	0.139	0.343	0.122	0.000
2409376704872793344	HQ Aqr	0.51889	2477	+200/−184	1.116	0.192	1.321	0.262	0.731	0.225	0.000
2414817603803476864	UU Cet	0.60610	1874	+67/−77	0.627	0.093	0.836	0.119	0.213	0.106	0.000
2438710609949867776	BR Aqr	0.48188	1240	+34/−26	1.073	0.062	1.282	0.087	0.612	0.081	0.000
4628067852624828672	⋯	0.31610	3360	+133/−99	0.405	0.082	0.522	0.102	0.166	0.091	0.302
4630819719774282624	SU Hyi	0.34838	1725	+43/−41	1.110	0.067	1.288	0.108	0.803	0.084	0.264
4631934555845355136	RW Hyi	0.55580	2241	+68/−55	0.706	0.070	0.946	0.095	0.343	0.084	0.206
4633341282190404864	SX Hyi	0.31067	2331	+84/−66	0.600	0.078	0.747	0.099	0.341	0.088	0.176
4643476198121275648	BB Hyi	0.28714	1881	+47/−47	0.519	0.062	0.617	0.083	0.276	0.072	0.116
4643606391466365824	TW Hyi	0.67538	2757	+117/−80	0.660	0.089	0.898	0.119	0.320	0.104	0.128
4650753560652926976	LMC-RRLYR-23457	0.55867	3925	+279/−224	0.601	0.154	0.861	0.177	0.264	0.175	0.370
4651573315306993920	T Men	0.40981	3148	+136/−133	0.653	0.102	0.711	0.137	0.364	0.121	0.534
4652488727438230144	SZ Men	0.53712	3050	+161/−170	0.635	0.136	0.854	0.173	0.333	0.154	0.302
4655243519513497728	OGLE BRIGHT-LMC-RRLYR-3	0.73595	4217	+382/−212	−1.999	0.155	−2.230	0.167	−1.660	0.161	2.585/1.531
4655249601190389632	XX Dor	0.32894	1252	+21/−16	0.185	0.039	0.233	0.059	0.031	0.048	0.705
4656309186747326336	LMC-RRLYR-854	0.51629	3899	+207/−158	0.374	0.115	0.554	0.141	0.108	0.132	0.517
4659096066472534272	ASAS J055122-6812.7	0.32178	1700	+40/−40	0.496	0.058	0.575	0.077	0.296	0.067	0.288
4660942838001474304	RT Dor	0.48283	3577	+312/−215	0.787	0.175	1.031	0.210	0.471	0.195	0.175
4661506200297885184	LMC-RRLYR-3497	0.52531	3770	+251/−165	−0.435	0.129	−0.497	0.156	−0.386	0.143	1.379/0.556
4662161543577035136	ASAS J045426-6626.2	0.60884	1980	+51/−45	−2.016	0.058	−2.343	0.073	−1.497	0.065	3.003/1.549
4662259606266850944	SX Dor	0.63146	4773	+361/−314	0.386	0.164	0.567	0.191	0.067	0.176	0.197
4668759884616161536	TU Ret	0.45884	3760	+209/−158	0.787	0.116	1.057	0.132	0.409	0.135	0.085
4669338159011904768	NSV 1432	0.36060	1485	+27/−27	0.490	0.047	0.598	0.066	0.225	0.056	0.154
4672117758766686720	SW Ret	0.47659/0.35481	2044	+109/−115	0.949	0.125	1.126	0.139	0.667	0.131	0.226
4672142016741937152	X Ret	0.49197	1522	+32/−32	0.720	0.055	0.893	0.085	0.359	0.072	0.144
4675881215270421376	⋯	0.76713	4582	+320/−256	0.441	0.139	0.682	0.147	0.036	0.144	0.121
4685757887726594816	SMC-RRLYR-770	0.73290	2834	+122/−93	0.127	0.089	0.341	0.109	−0.239	0.098	0.169
4687291397189729536	SMC-RRLYR-2428	0.31633	3513	+137/−132	0.345	0.089	0.448	0.104	0.122	0.096	0.113
4692528057537147136	AM Tuc	0.40579	1811	+46/−40	0.220	0.059	0.374	0.078	−0.083	0.068	0.064
4705269305654137728	AG Tuc	0.60259	3216	+154/−139	0.278	0.108	0.491	0.137	−0.096	0.125	0.051
4709830423483623808	W Tuc	0.64225	1596	+33/−38	0.491	0.059	0.601	0.103	0.041	0.084	0.056
4710156463040888192	AE Tuc	0.41453	1650	+35/−35	1.209	0.056	1.441	0.074	0.784	0.079	0.039
4718233887776006400	IY Eri	0.37503	1312	+17/−18	0.382	0.034	0.486	0.049	0.122	0.041	0.075
4720955591371097984	RV Hor	0.57250	3349	+161/−158	0.607	0.118	0.783	0.156	0.272	0.136	0.088
4728532703955609728	⋯	0.51811	2616	+136/−100	0.854	0.111	1.058	0.145	0.521	0.126	0.042
4758746729436076544	⋯	0.44728	2529	+92/−78	1.168	0.088	1.330	0.131	0.797	0.108	0.192

Table 8
(Continued)

Gaia DR2 ID	Name	Period (days)	Distance (pc)	σD (pc)	M_G (mag)	σM_G (mag)	M_{BP} (mag)	σM_{BP} (mag)	M_{RP} (mag)	σM_{RP} (mag)	A_g (mag)
4760456779256739968	ASAS J052122-6221.4	0.64968	2010	+39/−38	0.604	0.048	0.826	0.065	0.207	0.056	0.136
4764459551334687744	NSV 1856	0.51610	2221	+82/−61	0.803	0.081	0.984	0.115	0.487	0.098	0.055
4902647036002699136	⋯	0.28784	2528	+78/−81	0.571	0.073	0.680	0.085	0.361	0.079	0.037
4917277962356593664	⋯	0.33696	2222	+67/−56	0.603	0.065	0.745	0.079	0.330	0.072	0.063
4918030715504071296	AO Tuc	0.33323	1288	+24/−21	0.520	0.044	0.617	0.061	0.257	0.052	0.033
4918121665731513728	UZ Tuc	0.62531	2629	+152/−120	0.951	0.124	1.169	0.156	0.606	0.139	0.037
4929368054776557184	DR Dor	0.46039	2340	+76/−73	0.786	0.079	0.963	0.105	0.500	0.092	0.037
4982010850448460160	CS Phe	0.48440	2970	+117/−105	0.866	0.091	1.054	0.116	0.518	0.104	0.033
4984655725669340544	TZ Phe	0.61560	2491	+108/−92	0.758	0.090	0.986	0.099	0.379	0.095	0.031
4985455998336183168	VW Scl	0.51091	1110	+51/−41	0.921	0.097	1.087	0.117	0.500	0.112	0.045
5211923198582228224	AV Men	0.55496	2860	+138/−142	0.627	0.121	0.776	0.162	0.330	0.140	0.459
5262046772597317376	ASAS J065818-7411.7	0.60109	3735	+145/−164	0.635	0.099	0.859	0.122	0.290	0.110	0.443
5271444195402177792	AL Vol	0.51721/0.38522	2407	+70/−64	0.396	0.067	0.543	0.085	0.131	0.075	0.388
5280964179391935616	⋯	0.28245	2914	+95/−85	0.623	0.074	0.717	0.094	0.416	0.083	0.389
5281881584407284352	NSV 3229	0.57240	2921	+120/−121	0.204	0.099	0.419	0.120	−0.105	0.108	0.235
5285349822037246464	⋯	0.32123	3736	+128/−141	0.301	0.086	0.422	0.106	0.083	0.096	0.215
5479480350950961536	⋯	0.52209	3521	+181/−162	0.788	0.117	0.991	0.149	0.464	0.132	0.463
5481339590753150208	ST Pic	0.48575	480	+3/−3	0.883	0.021	1.116	0.040	0.553	0.030	0.163
5482545510194122112	⋯	0.33788	2539	+82/−78	0.325	0.074	0.431	0.088	0.107	0.080	0.152
5495625579691991424	⋯	0.28605	3461	+122/−135	0.737	0.089	0.862	0.111	0.525	0.099	0.141
6353053196895087488	TT Oct	0.56772	2420	+85/−78	0.860	0.085	1.098	0.115	0.500	0.099	0.235
6378877082899249664	AR Oct	0.39403	2043	+73/−83	1.204	0.097	1.423	0.131	0.869	0.116	0.086
6379606226611647744	⋯	0.32635	2838	+105/−103	0.306	0.086	0.453	0.104	0.053	0.095	0.093
6380659528686603008	BK Tuc	0.55006	2764	+105/−129	0.578	0.101	0.848	0.115	0.143	0.121	0.081
6398671998754509056	NSV 14009	0.56393	2340	+72/−84	0.490	0.083	0.712	0.109	0.123	0.095	0.115
6409071321466282752	ASAS J215601-6129.2	0.61609	2388	+93/−81	0.781	0.089	1.009	0.113	0.453	0.101	0.111
6458861949615378688	DE Ind	0.48076	2228	+95/−96	0.858	0.106	1.060	0.137	0.527	0.123	0.108
6459713658809674880	CZ Ind	0.60517	3091	+180/−153	0.667	0.127	0.862	0.155	0.332	0.139	0.171
6483680332235888896	V Ind	0.47959	662	+7/−7	0.775	0.036	1.014	0.062	0.427	0.054	0.139
6491783148816832256	⋯	0.28643	1916	+52/−43	0.429	0.057	0.522	0.066	0.221	0.061	0.060
6492356127518044800	YY Tuc	0.63486	2071	+71/−65	0.478	0.080	0.698	0.102	0.053	0.099	0.053
6501050653153411712	EP Gru	0.36972	2742	+138/−105	0.475	0.102	0.626	0.117	0.204	0.109	0.035
6504972134389792128	EP Tuc	0.61499	2774	+98/−84	0.900	0.076	1.132	0.090	0.522	0.083	0.055
6508563379883711616	UW Gru	0.54820	2716	+105/−101	1.014	0.093	1.257	0.113	0.632	0.110	0.068
6508871277499009664	ASAS J221052-5508.0	0.88747	4211	+264/−246	−0.493	0.139	−0.264	0.158	−0.882	0.149	0.056
6511192827581914752	NSV 14088	0.58693	3631	+281/−201	0.342	0.157	0.543	0.191	−0.003	0.173	0.046
6511489936239739904	ASAS J221039-5049.8	0.33068	2977	+119/−152	0.227	0.109	0.349	0.130	−0.024	0.118	0.068
6519995861275291008	RW Gru	0.55032	2393	+121/−110	0.456	0.115	0.618	0.147	0.099	0.130	0.034
6521271603997336832	CZ Phe	0.56680/0.42250	2928	+118/−122	0.433	0.095	0.623	0.110	0.126	0.102	0.046
6523414998837956736	⋯	0.31954	1335	+45/−38	0.589	0.073	0.701	0.087	0.300	0.079	0.029
6526559499016401408	RV Phe	0.59642	1789	+79/−53	0.613	0.087	0.803	0.107	0.199	0.097	0.024
6526839462163012352	NSV 14530	0.55321	2400	+107/−105	0.555	0.106	0.750	0.133	0.179	0.119	0.018
6527714432898901248	ASAS J231412-4648.9	0.27090	3326	+194/−181	0.423	0.129	0.543	0.147	0.215	0.138	0.024
6529889228241771264	⋯	0.54230/0.40594	3168	+206/−217	0.356	0.152	0.550	0.170	0.051	0.161	0.030
6535970906228369024	AQ Gru	0.63691	3351	+371/−248	0.227	0.209	0.472	0.234	−0.173	0.231	0.056

Table 8
(Continued)

Gaia DR2 ID	Name	Period (days)	Distance (pc)	σD (pc)	M_G (mag)	σM_G (mag)	M_{BP} (mag)	σM_{BP} (mag)	M_{RP} (mag)	σM_{RP} (mag)	A_g (mag)
6537939405704263936	CN Scl	0.58582	3525	+302/−254	0.397	0.180	0.574	0.212	0.017	0.193	0.048
6541769554459131648	BO Gru	0.28111	2634	+196/−128	0.635	0.136	0.742	0.146	0.429	0.141	0.027
6553439603373054720	CV Scl	0.59348	2383	+92/−94	0.437	0.096	0.658	0.127	0.063	0.110	0.046
6558308790617955584	AO Ind	0.39812	2978	+187/−175	0.694	0.146	0.889	0.181	0.417	0.163	0.067
6562909314771450368	Z Gru	0.488017/0.363187	1946	+57/−54	0.760	0.073	0.915	0.098	0.461	0.084	0.075
6564274294034705664	RT Gru	0.51213	2338	+113/−134	0.879	0.125	1.089	0.151	0.565	0.139	0.047
6565527904791301504	RR Gru	0.55245	1960	+54/−62	0.886	0.073	1.122	0.095	0.505	0.083	0.070
6566136523133385344	EG Gru	0.61542	4180	+480/−400	−0.201	0.240	0.021	0.272	−0.534	0.255	0.046
6570158089992425984	NSV 14073	0.69609	3287	+237/−175	0.337	0.143	0.567	0.165	−0.023	0.153	0.035
6585414123064537344	ASAS J213826-3945.0	0.41070	4266	+251/−265	0.024	0.139	0.165	0.157	−0.268	0.146	0.063
6591208755501548672	NSV 13885	0.61543	2290	+93/−70	0.459	0.089	0.632	0.123	0.104	0.104	0.086
6611282775511288832	V354 Aqr	0.52956	3651	+310/−286	0.429	0.192	0.605	0.233	0.084	0.212	0.056
6611919706276933376	…	0.29132	2708	+107/−104	0.652	0.091	0.785	0.107	0.436	0.098	0.060
6616811807170380928	AD PsA	0.75680	2567	+161/−121	0.664	0.126	0.890	0.146	0.316	0.136	0.084
6625215584995450624	AE PsA	0.54674	2091	+87/−83	0.662	0.113	0.826	0.184	0.258	0.146	0.000
6774717933372604544	XZ Mic	0.44918	1863	+127/−121	1.546	0.162	1.736	0.204	1.216	0.184	0.120
6775336855339787008	ASAS J210032-3708.3	0.59742	2619	+172/−122	0.919	0.133	1.158	0.157	0.577	0.146	0.209
6778621508888695296	ASAS J205705-3621.8	0.48348	1915	+46/−55	1.000	0.064	1.215	0.079	0.618	0.082	0.228
6780267993191790464	…	0.83263	2610	+193/−155	0.655	0.149	0.907	0.161	0.272	0.155	0.248
6784648718097899520	ASAS J212331-3025.0	0.36744	1980	+82/−91	0.658	0.103	0.805	0.125	0.375	0.113	0.281
6785264788206270336	SX PsA	0.56279	5050	+662/−440	−0.498	0.242	−0.322	0.267	−0.813	0.254	0.169
6787617919184986496	Z Mic	0.73189	1220	+33/−33	0.759	0.067	0.993	0.089	0.383	0.079	0.338
6788454544456587520	…	0.54043	1578	+89/−76	0.476	0.120	0.676	0.137	0.089	0.128	0.338
6788756669633846016	…	0.46078	2960	+238/−210	0.593	0.180	0.819	0.221	0.245	0.202	0.253
6800126375781155072	ASAS J204034-2540.5	0.65361	2903	+192/−189	0.735	0.155	0.892	0.190	0.355	0.181	0.225
6800564393726439552	…	0.30141	2088	+71/−77	0.801	0.083	0.951	0.098	0.547	0.089	0.281
6805869292514475264	ASAS J205048-2436.4	0.66189	2306	+114/−104	0.619	0.114	0.833	0.147	0.279	0.129	0.197
6811546934337150464	YZ PsA	0.31685	1593	+89/−96	0.502	0.133	0.633	0.151	0.205	0.141	0.056
6817857748827529344	DL Cap	0.64019	1933	+77/−81	0.610	0.097	0.822	0.119	0.224	0.107	0.113
6820039248616386688	BV Aqr	0.36371	1116	+24/−30	0.576	0.061	0.707	0.083	0.297	0.072	0.056

(This table is available in machine-readable form.)

Table 9
The U, V, and W Velocity Components and Radial Velocities

Gaia DR2 ID	Name	U (km s^{-1})	σU	V (km s^{-1})	σV	W (km s^{-1})	σW	Source	RV (km s^{-1})	σRV
2329707050101123712	UZ Scl	−208	18	109	10	16.9	9.6	Layden	−4	10
2336550174250087936	RU Scl	−144	4	−131	4	−76.9	7.9	Layden	38	8
2438710609949867776	BR Aqr	−61	5	−28	1	−62.3	9.1	Layden	29	10
4628067852624828672	⋯	−253	59	−157	22	11.7	42	GALAH	150	75
4631934555845355136	RW Hyi	−462	51	252	30	13.2	47.3	GALAH	405	75
4633341282190404864	SX Hyi	−131	51	329	29	−1.6	46.7	GALAH	212	75
4643476198121275648	BB Hyi	−268	51	236	23	−97.9	49.2	GALAH	319	75
4643606391466365824	TW Hyi	−364	12	41	3	46.2	11.1	Layden	227	9
4652488727438230144	SZ Men	−396	61	−281	28	−17.2	43.9	GALAH	258	75
4660942838001474304	RT Dor	−294	17	−353	31	−172.8	10.7	Layden	320	20
4661506200297885184	LMC-RRLYR-3497	−216	33	−138	14	−345.7	25.6	Layden	358	40
4662259606266850944	SX Dor	−180	35	113	13	86	28.9	Layden	105	40
4669338159011904768	NSV 1432	−218	55	−64	10	−10	49.2	RAVE	159	75
4672142016741937152	X Ret	−266	10	−288	8	1.3	9.5	Layden	144	13
4685757887726594816	SMC-RRLYR-770	−352	46	41	30	19.2	51.7	GALAH	216	75
4692528057537147136	AM Tuc	−370	44	−11	24	103.2	56.9	RAVE	131	75
4709830423483623808	W Tuc	−169	4	43	1	43.9	3.3	Layden	63	3
4710156463040888192	AE Tuc	−47	5	−30	3	−76.5	8.2	Layden	76	10
4760456779256739968	ASAS J052122-6221.4	−313	62	−109	3	−95.4	42.2	RAVE	311	75
4764459551334687744	NSV 1856	−263	60	−231	9	−139.3	44.5	GALAH	312	75
4902647036002699136	⋯	−45	35	325	27	146.2	61.8	GALAH	−2	75
4918030715504071296	AO Tuc	−382	30	117	28	−68.5	61.7	RAVE	254	75
4918121665731513728	UZ Tuc	−281	33	−11	27	−10	63.7	GALAH	118	75
4929368054776557184	DR Dor	−298	31	−292	14	−40.4	69	RAVE	118	75
4982010850448460160	CS Phe	−295	24	−314	20	−198.8	72.1	RAVE	237	75
4984655725669340544	TZ Phe	−141	5	−158	7	−73.8	2.9	Layden	92	3
5481339590753150208	ST Pic	−54	66	−78	1	−55.5	35.1	RAVE	72	75
6353053196895087488	TT Oct	−238	48	−158	36	−11.2	46.2	GALAH	83	75
6378877082899249664	AR Oct	−20	23	−52	20	5.3	25.9	Layden	−18	40
6379606226611647744	⋯	−443	46	−332	39	−103.4	51.1	GALAH	172	75
6380659528686603008	BK Tuc	−399	19	−236	17	−22.2	10	Layden	121	14
6409071321466282752	ASAS J215601-6129.2	−279	28	65	47	−55.1	53.5	GALAH	174	75
6458861949615378688	DE Ind	−81	21	68	49	68.4	53.6	GALAH	19	75
6483680332235888896	V Ind	−287	4	298	3	46.4	3.2	Layden	202	3
6519995861275291008	RW Gru	−464	30	61	6	79.7	10.1	Layden	0	10
6521271603997336832	CZ Phe	−182	25	84	28	65.1	67.2	RAVE	28	75
6562909314771450368	Z Gru	−204	12	175	51	160	54.6	GALAH	29	75
6564274294034705664	RT Gru	−322	19	−352	19	−171	15	Layden	−67	10
6565527904791301504	RR Gru	−26	1	59	9	5.5	10.5	Layden	37	14
6625215584995450624	AE PsA	−338	26	−14	39	99.9	61.8	RAVE	−176	75
6785264788206270336	SX PsA	−379	103	322	98	178.8	74.2	GALAH	5	75
6787617919184986496	Z Mic	−57	2	−97	7	−30.6	7.2	Layden	−58	10
6820039248616386688	BV Aqr	−188	25	−91	40	178.3	59.4	RAVE	−249	75
2414817603803476864	UU Cet	−228	21	−290	13	41.2	72.9	Gaia	−118	75
6526839462163012352	NSV 14530	−324	21	−263	34	−80.2	67.4	Gaia	15	75
6398671998754509056	NSV 14009	−3	32	8	45	−108.3	51.8	Gaia	79	75
2334529752915355520	TX Scl	−153	12	−27	14	−107.7	73	Gaia	81	75
6778621508888695296	ASAS J205705-3621.8	−169	9	148	58	−55.7	48.8	Gaia	134	75
4662161543577035136	ASAS J045426-6626.2	−154	60	31	8	−43.6	44.2	Gaia	152	75
6566136523133385344	EG Gru	−442	58	498	69	181.2	72.3	Gaia	198	75
				Gaia–Enceladus members						
4705269305654137728	AG Tuc	−371	15	−149	12	−61.1	8.5	Layden	196	9
6508563379883711616	UW Gru	−223	14	268	24	163.3	30.8	Layden	81	36
4985455998336183168	VW Scl	−263	20	23	3	−35	72.8	Gaia	94	75
6774717933372604544	XZ Mic	−197	15	40	11	61.6	9.9	Layden	−19	14
6492356127518044800	YY Tuc	−268	10	10	4	47	8.2	Layden	56	9
				Non-RR Lyrae stars						
4998159961839894656	UY Scl	−5	8	−10	16	−20.6	72.5	RAVE	19	75
6459704308665358848	⋯	−13	19	−21	51	−8.8	50.4	RAVE	−6	75

Note. The "Source" column refers the following RV data sources: Gaia, Gaia Collaboration et al. (2018a); GALAH, Buder et al. (2021); Layden, Layden (1994); RAVE, Steinmetz et al. (2020).

(This table is available in machine-readable form.)

Table 10
Periods and Relative Fourier Parameters

Gaia DR2 ID	Name	Period (days)	R_{21}	σR_{21}	R_{31}	σR_{31}	ϕ_{21}	$\sigma\phi_{21}$	ϕ_{31}	$\sigma\phi_{31}$
			RR Lyrae stars							
2309225008197193856	WW Scl	0.78483	0.4683	0.0032	0.2747	0.0052	3.0314	0.0029	6.2151	0.0051
2313783205448950784	TW Scl	0.61681	0.4856	0.0040	0.2899	0.0062	2.9645	0.0039	6.0443	0.0065
2329707050101123712	UZ Scl	0.44914	0.5306	0.0014	0.3750	0.0017	2.5310	0.0014	5.3794	0.0017
2334529752915355520	TX Scl	0.72777	0.4792	0.0028	0.2905	0.0043	3.0279	0.0028	6.2117	0.0043
2336550174250087936	RU Scl	0.49336	0.5010	0.0041	0.3695	0.0055	2.5344	0.0043	5.3652	0.0054
2385090584663565696	V356 Aqr	0.55471	0.4957	0.0093	0.324	0.012	2.6914	0.0086	5.718	0.012
2394631356295692032	NSVS 14632323	0.35525	0.110	0.013	0.065	0.022	3.376	0.014	0.842	0.022
2394898640700233600	OW Aqr	0.65490	0.5259	0.0083	0.353	0.012	2.6946	0.0086	5.474	0.013
2399010298791985280	ASAS J231209-1855.4	0.30793	0.108	0.012	0.014	0.099	2.252	0.013	4.511	0.094
2408425936552330880	V360 Aqr	0.62358	0.166	0.072	0.069	0.176	2.867	0.075	4.639	0.191
2409376704872793344	HQ Aqr	0.51890	0.5254	0.0012	0.3636	0.0015	2.5662	0.0012	5.4371	0.0015
2414817603803476864	UU Cet	0.60607	0.4662	0.0032	0.2938	0.0049	2.8423	0.0035	5.9592	0.0050
2438710609949867776	BR Aqr	0.48186	0.5529	0.0014	0.3580	0.0019	2.6764	0.0014	5.6475	0.0021
4628067852624828672	⋯	0.31610	0.1635	0.0055	0.0545	0.0167	3.0632	0.0058	5.826	0.017
4630819719774282624	SU Hyi	0.34840	0.5170	0.0056	0.2528	0.0104	2.7873	0.0056	5.543	0.010
4631934555845355136	RW Hyi	0.55556	0.465	0.012	0.271	0.019	2.833	0.012	5.774	0.019
4633341282190404864	SX Hyi	0.31068	0.1418	0.0087	0.084	0.014	3.1842	0.0089	0.236	0.015
4643476198121275648	BB Hyi	0.28713	0.1819	0.0033	0.0755	0.0072	3.2589	0.0031	6.1433	0.0069
4643606391466365824	TW Hyi	0.67537	0.5255	0.0023	0.3298	0.0032	2.8662	0.0022	5.8760	0.0034
4650753560652926976	LMC-RRLYR-23457	0.55867	0.4506	0.0083	0.289	0.013	2.6713	0.0089	5.387	0.013
4651573315306993920	T Men	0.40982	0.5133	0.0063	0.2783	0.0101	2.3949	0.0061	5.318	0.010
4652488727438230144	SZ Men	0.53712	0.4222	0.0060	0.3005	0.0082	2.5105	0.0065	5.1534	0.0080
4655243519513497728	BRIGHT-LMC-RRLYR-3	0.73595	0.291	0.012	0.100	0.034	3.191	0.011	0.485	0.034
4655249601190389632	XX Dor	0.32894	0.094	0.016	0.064	0.024	3.341	0.017	0.910	0.025
4656309186747326336	LMC-RRLYR-854	0.51624	0.5216	0.0036	0.3745	0.0043	2.5770	0.0034	5.4474	0.0043
4659096066472534272	ASAS J055122-6812.7	0.32178	0.1139	0.0047	0.0681	0.0086	3.4859	0.0051	0.7048	0.0088
4660942838001474304	RT Dor	0.48284	0.4502	0.0028	0.2875	0.0045	2.5085	0.0030	5.3319	0.0044
4661506200297885184	LMC-RRLYR-3497	0.52485	0.469	0.014	0.317	0.021	2.577	0.014	5.342	0.021
4662161543577035136	ASAS J045426-6626.2	0.60885	0.4461	0.0037	0.2536	0.0057	2.9923	0.0036	6.2060	0.0063
4662259606266850944	SX Dor	0.63150	0.4917	0.0085	0.310	0.012	2.6878	0.0082	5.542	0.012
4668759884616161536	TU Ret	0.45885	0.4670	0.0014	0.3517	0.0018	2.4202	0.0014	5.0005	0.0019
4669338159011904768	NSV 1432	0.36062	0.045	0.025	0.063	0.017	3.442	0.025	1.777	0.018
4672142016741937152	X Ret	0.49212	0.4689	0.0075	0.304	0.011	2.4665	0.0074	4.986	0.012
4675881215270421376	⋯	0.76712	0.2680	0.0046	0.0802	0.0165	3.2401	0.0053	0.584	0.016
4685757887726594816	SMC-RRLYR-770	0.73292	0.4230	0.0036	0.2663	0.0056	2.8472	0.0034	5.9634	0.0053
4687291397189729536	SMC-RRLYR-2428	0.31637	0.078	0.051	0.026	0.165	3.301	0.051	0.690	0.174
4692528057537147136	AM Tuc	0.40577	0.086	0.018	0.069	0.023	3.945	0.017	1.379	0.021
4705269305654137728	AG Tuc	0.60259	0.4574	0.0018	0.3664	0.0022	2.5251	0.0019	5.2519	0.0022
4709830423483623808	W Tuc	0.64224	0.5486	0.0008	0.3376	0.0013	2.7269	0.0009	5.5973	0.0012
4710156463040888192	AE Tuc	0.41453	0.5343	0.0007	0.3791	0.0009	2.5033	0.0007	5.3466	0.0009
4718233887776006400	IY Eri	0.37500	0.048	0.013	0.044	0.014	3.659	0.013	1.204	0.014
4720955591371097984	RV Hor	0.57163	0.498	0.014	0.272	0.023	2.792	0.013	5.864	0.024
4728532703955609728	⋯	0.51810	0.5225	0.0020	0.3638	0.0029	2.5941	0.0021	5.5041	0.0028
4758746729436076544	⋯	0.44104	0.5605	0.0011	0.3379	0.0017	2.8257	0.0011	5.8531	0.0017
4760456779256739968	ASAS J052122-6221.4	0.64970	0.3795	0.0021	0.1829	0.0045	3.0665	0.0021	0.1098	0.0053
4764459551334687744	NSV 1856	0.51604	0.4166	0.0065	0.2293	0.0119	2.5379	0.0067	4.841	0.012
4902647036002699136	⋯	0.28783	0.1508	0.0057	0.0204	0.0420	2.7874	0.0053	5.737	0.036
4917277962356593664	⋯	0.33695	0.093	0.021	0.066	0.030	3.369	0.022	0.944	0.029
4918030715504071296	AO Tuc	0.33322	0.112	0.010	0.060	0.021	3.445	0.011	0.749	0.020
4918121665731513728	UZ Tuc	0.62533	0.4619	0.0018	0.3699	0.0023	2.4850	0.0018	5.1708	0.0022
4929368054776557184	DR Dor	0.45913	0.373	0.029	0.176	0.061	2.403	0.031	4.833	0.064
4982010850448460160	CS Phe	0.48471	0.441	0.023	0.210	0.042	2.637	0.023	5.290	0.045
4984655725669340544	TZ Phe	0.61560	0.3750	0.0021	0.1762	0.0040	3.0348	0.0021	0.0726	0.0042
4985455998336183168	VW Scl	0.51091	0.5130	0.0012	0.3311	0.0018	2.4778	0.0013	5.2970	0.0018
5211923198582228224	AV Men	0.55497	0.4816	0.0025	0.2494	0.0047	2.5941	0.0027	5.3133	0.0046
5262046772597317376	ASAS J065818-7411.7	0.60112	0.4682	0.0023	0.3063	0.0031	2.8158	0.0022	5.9142	0.0033
5280964179391935616	⋯	0.28246	0.1520	0.0062	0.0883	0.0118	3.0875	0.0066	6.276	0.012
5281881584407284352	NSV 3229	0.57241	0.5197	0.0018	0.3484	0.0027	2.6911	0.0019	5.6682	0.0027
5285349822037246464	⋯	0.32122	0.279	0.014	0.072	0.051	2.921	0.013	5.644	0.054
5479480350950961536	⋯	0.52209	0.5061	0.0064	0.3576	0.0089	2.6186	0.0069	5.5671	0.0088
5481339590753150208	ST Pic	0.48569	0.4176	0.0006	0.1940	0.0012	3.1228	0.0006	0.1699	0.0012
5482545510194122112	⋯	0.33787	0.099	0.010	0.032	0.029	3.329	0.010	0.179	0.030
5495625579691991424	⋯	0.28606	0.177	0.015	0.074	0.040	3.327	0.017	6.257	0.039

Table 10
(Continued)

Gaia DR2 ID	Name	Period (days)	R_{21}	σR_{21}	R_{31}	σR_{31}	ϕ_{21}	$\sigma\phi_{21}$	ϕ_{31}	$\sigma\phi_{31}$
6353053196895087488	TT Oct	0.56774	0.4989	0.0026	0.3123	0.0038	2.8601	0.0027	5.9645	0.0038
6378877082899249664	AR Oct	0.39403	0.5866	0.0057	0.3432	0.0087	2.6535	0.0061	5.4873	0.0085
6379606226611647744	⋯	0.32635	0.1432	0.0084	0.074	0.016	3.1678	0.0082	0.128	0.016
6380659528686603008	BK Tuc	0.55007	0.4658	0.0035	0.3707	0.0048	2.5165	0.0036	5.2482	0.0046
6398671998754509056	NSV 14009	0.56400	0.4891	0.0093	0.324	0.014	2.7178	0.0090	5.722	0.014
6409071321466282752	ASAS J215601-6129.2	0.61610	0.5435	0.0023	0.3447	0.0033	2.6934	0.0022	5.5924	0.0033
6458861949615378688	DE Ind	0.48079	0.4538	0.0053	0.2536	0.0096	2.5129	0.0054	5.3436	0.0092
6459713658809674880	CZ Ind	0.60507	0.376	0.018	0.268	0.022	2.492	0.018	5.418	0.026
6483680332235888896	V Ind	0.47961	0.4496	0.0011	0.3334	0.0017	2.5411	0.0012	5.3485	0.0016
6491783148816832256	⋯	0.28644	0.0803	0.0058	0.0229	0.0203	3.1937	0.0058	0.221	0.021
6492356127518044800	YY Tuc	0.63489	0.5376	0.0016	0.3388	0.0022	2.6437	0.0017	5.5141	0.0022
6501050653153411712	EP Gru	0.36973	0.113	0.012	0.074	0.019	3.337	0.012	0.723	0.019
6504972134389792128	EP Tuc	0.61442	0.404	0.013	0.233	0.022	2.759	0.013	5.763	0.021
6508563379883711616	UW Gru	0.54822	0.4725	0.0025	0.3645	0.0030	2.5214	0.0024	5.2991	0.0028
6511192827581914752	NSV 14088	0.63991	0.5063	0.0027	0.3619	0.0036	2.6617	0.0028	5.4429	0.0036
6511489936239739904	ASAS J221039-5049.8	0.33068	0.265	0.018	0.080	0.055	2.992	0.018	5.639	0.058
6519995861275291008	RW Gru	0.55007	0.445	0.012	0.281	0.019	2.487	0.013	5.220	0.019
6523414998837956736	⋯	0.31954	0.101	0.015	0.073	0.021	3.271	0.014	0.807	0.020
6526559499016401408	RV Phe	0.59639	0.4731	0.0031	0.3044	0.0045	2.7865	0.0032	5.8620	0.0049
6526839462163012352	NSV 14530	0.55322	0.5040	0.0018	0.3618	0.0023	2.5973	0.0018	5.5036	0.0025
6527714432898901248	ASAS J231412-4648.9	0.27087	0.179	0.028	0.069	0.075	3.149	0.029	6.045	0.079
6535970906228369024	AQ Gru	0.63694	0.4938	0.0018	0.3575	0.0025	2.5959	0.0017	5.4832	0.0023
6537939405704263936	CN Scl	0.58573	0.4865	0.0029	0.3373	0.0042	2.6923	0.0031	5.6943	0.0042
6541769554459131648	BO Gru	0.28086	0.068	0.324	0.019	1.125	3.276	0.321	0.350	1.080
6553439603373054720	CV Scl	0.59349	0.4671	0.0023	0.2847	0.0036	2.9195	0.0022	6.0872	0.0036
6558308790617955584	AO Ind	0.39790	0.444	0.016	0.220	0.029	2.504	0.015	5.106	0.028
6564274294034705664	RT Gru	0.51271	0.442	0.016	0.269	0.027	2.577	0.018	5.657	0.027
6565527904791301504	RR Gru	0.55247	0.4824	0.0025	0.2771	0.0040	3.0595	0.0024	0.0464	0.0041
6566136523133385344	EG Gru	0.61542	0.5043	0.0015	0.3588	0.0022	2.5805	0.0017	5.4562	0.0022
6570158089992425984	NSV 14073	0.69612	0.4460	0.0030	0.3095	0.0038	2.7474	0.0030	5.7763	0.0041
6585414123064537344	ASAS J213826-3945.0	0.41113	0.080	0.022	0.063	0.026	3.866	0.023	1.204	0.026
6591208755501548672	NSV 13885	0.61584	0.5103	0.0067	0.3489	0.0090	2.6091	0.0067	5.4965	0.0094
6611282775511288832	V354 Aqr	0.52885	0.365	0.017	0.226	0.027	2.403	0.018	4.965	0.026
6611919706276933376	⋯	0.29130	0.141	0.011	0.087	0.018	3.141	0.011	0.240	0.019
6616811807170380928	AD PsA	0.75682	0.4400	0.0043	0.2478	0.0073	3.0560	0.0044	6.2637	0.0070
6625215584995450624	AE PsA	0.54672	0.535	0.013	0.339	0.020	2.526	0.014	5.363	0.020
6774717933372604544	XZ Mic	0.44910	0.4755	0.0039	0.3314	0.0053	2.4069	0.0036	4.9466	0.0052
6775336855339787008	ASAS J210032-3708.3	0.59742	0.5429	0.0033	0.3451	0.0047	2.8067	0.0036	5.7866	0.0050
6778621508888695296	ASAS J205705-3621.8	0.48351	0.4962	0.0018	0.3741	0.0025	2.4960	0.0018	5.2646	0.0024
6780267993191790464	⋯	0.83270	0.3435	0.0047	0.1329	0.0108	3.3143	0.0043	0.599	0.011
6784648718097899520	ASAS J212331-3025.0	0.36744	0.065	0.047	0.064	0.050	3.839	0.048	1.501	0.049
6787617919184986496	Z Mic	0.58695	0.4737	0.0032	0.2850	0.0048	2.9136	0.0032	6.0747	0.0047
6788454544456587520	⋯	0.73188	0.4370	0.0052	0.2265	0.0096	3.1929	0.0049	0.2898	0.0087
6788756669633846016	⋯	0.54043	0.4721	0.0056	0.3688	0.0066	2.5027	0.0053	5.2429	0.0067
6800126375781155072	ASAS J204034-2540.5	0.46080	0.4647	0.0049	0.3461	0.0066	2.4008	0.0049	4.9467	0.0069
6800564393726439552	⋯	0.30139	0.116	0.018	0.072	0.028	3.145	0.017	0.550	0.028
6805869292514475264	ASAS J205048-2436.4	0.65356	0.5070	0.0072	0.320	0.010	2.9073	0.0069	5.9315	0.0099
6811546934337150464	YZ PsA	0.31686	0.099	0.018	0.069	0.028	3.244	0.017	0.859	0.026
6817857748827529344	DL Cap	0.66191	0.4357	0.0029	0.2366	0.0050	3.0898	0.0029	0.0876	0.0051
6820039248616386688	BV Aqr	0.36383	0.066	0.034	0.064	0.036	3.528	0.034	1.418	0.035
			ACEP candidate stars							
6508871277499009664	ASAS J221052-5508.0	0.88743	0.3287	0.0019	0.2429	0.0023	2.5526	0.0019	5.0499	0.0025
6785264788206270336	SX PsA	0.56159	0.468	0.020	0.268	0.035	2.695	0.022	5.516	0.036
			Non-pulsating stars							
6459704308665358848	⋯	0.36792	0.159	0.028	0.024	0.190	0.304	0.030	4.925	0.196
6609938008366400256	ASAS J225559-2709.9	0.31037	0.214	0.027	0.069	0.079	3.040	0.026	3.836	0.077

(This table is available in machine-readable form.)

Table 11
Simplified Identification of Extra Mode Signals, Focusing on the Region between the Dominant Pulsation Frequency and Its First Harmonic

Name	FM freq. (day^{-1})	FM amp. (mag)	O1 freq. (day^{-1})	O1 amp. (mag)	Signal freq. (day^{-1})	Signal Amp. (mag)	Label
			RRab stars				
AD PsA	1.32132	0.15943	⋯	⋯	0.61258	0.00021	PD?
AE PsA	1.82904	0.22569	⋯	⋯	2.49730	0.00126	f_1
AO Ind	2.51195	0.23661	⋯	⋯	3.70060	0.00126	PD?
AO Ind	2.51195	0.23661	⋯	⋯	3.77605	0.00164	PD
AO Ind	2.51195	0.23661	⋯	⋯	4.24491	0.00110	f_2
AO Ind	2.51195	0.23661	⋯	⋯	4.32216	0.00166	f_2
AQ Gru	1.57001	0.18950	⋯	⋯	1.07763	0.00077	$f_2 - f_0$?
AQ Gru	1.57001	0.18950	⋯	⋯	2.67763	0.00034	f_2
AR Oct	2.53786	0.24263	⋯	⋯	1.73353	0.00031	$f_2 - f_0$?
AR Oct	2.53786	0.24263	⋯	⋯	4.27725	0.00024	f_2
AV Men	1.80191	0.23567	⋯	⋯	3.11128	0.00017	f_2
CS Phe	2.06538	0.18871	⋯	⋯	2.72329	0.00165	f_1?
CS Phe	2.06538	0.18871	⋯	⋯	2.75434	0.00219	f_1
CS Phe	2.06538	0.18871	⋯	⋯	2.78539	0.00171	f_1
CS Phe	2.06538	0.18871	⋯	⋯	3.05753	0.00363	PD?
CS Phe	2.06538	0.18871	⋯	⋯	3.09406	0.00193	PD
CZ Ind	1.65270	0.14444	⋯	⋯	2.26707	0.00859	f_1?
DE Ind	2.07991	0.25047	⋯	⋯	2.96407	0.00118	?
DE Ind	2.07991	0.25047	⋯	⋯	3.01797	0.00125	?
DE Ind	2.07991	0.25047	⋯	⋯	3.55509	0.00083	f_2
DR Dor	2.17353	0.17119	⋯	⋯	2.78904	0.00136	?
DR Dor	2.17353	0.17119	⋯	⋯	3.04110	0.00154	?
DR Dor	2.17353	0.17119	⋯	⋯	3.16164	0.00369	?
DR Dor	2.17353	0.17119	⋯	⋯	3.21096	0.00138	PD?
DR Dor	2.17353	0.17119	⋯	⋯	3.32785	0.00174	PD
DR Dor	2.17353	0.17119	⋯	⋯	3.68219	0.00129	f_2
EG Gru	1.62492	0.23617	⋯	⋯	1.11018	0.00046	$f_2 - f_0$?
GDR2 4728532703955609728	1.93011	0.20786	⋯	⋯	2.12785	0.00045	?
LMC-RRLYR-23457	1.78899	0.26386	⋯	⋯	2.68192	0.00117	PD
LMC-RRLYR-3497	1.90555	0.21344	⋯	⋯	2.50958	0.00194	f_1?
LMC-RRLYR-3497	1.90555	0.21344	⋯	⋯	2.57605	0.00270	f_1
LMC-RRLYR-3497	1.90555	0.21344	⋯	⋯	2.75210	0.00163	?
LMC-RRLYR-3497	1.90555	0.21344	⋯	⋯	2.80240	0.00147	?
LMC-RRLYR-3497	1.90555	0.21344	⋯	⋯	2.83653	0.00169	PD
LMC-RRLYR-854	1.93710	0.17902	⋯	⋯	6.48174	0.00068	?
NSV 14088	1.56273	0.23446	⋯	⋯	2.30838	0.00089	PD?
NSV 14088	1.56273	0.23446	⋯	⋯	2.66587	0.00063	f_2
NSV 1856	1.93779	0.27463	⋯	⋯	1.37092	0.00172	$f_2 - f_0$?
NSV 1856	1.93779	0.27463	⋯	⋯	2.49970	0.00079	?
NSV 1856	1.93779	0.27463	⋯	⋯	2.88694	0.00177	PD
NSV 1856	1.93779	0.27463	⋯	⋯	4.82671	0.00223	PD
OW Aqr	1.52694	0.21755	⋯	⋯	2.18082	0.00082	?
RT Gru	1.95202	0.23195	⋯	⋯	2.81677	0.00064	?
RT Gru	1.95202	0.23195	⋯	⋯	2.85270	0.00065	?
RT Gru	1.95202	0.23195	⋯	⋯	3.28024	0.00066	f_2
RU Scl	2.02693	0.22146	⋯	⋯	5.41918	0.00019	?
SX PsA	1.77805	0.19113	⋯	⋯	2.62461	0.00318	PD?
SX PsA	1.77805	0.19113	⋯	⋯	2.65813	0.00246	PD
SX PsA	1.77805	0.19113	⋯	⋯	3.03297	0.00184	f_2
SZ men	1.86169	0.23483	⋯	⋯	3.14778	0.00037	f_2
SZ men	1.86169	0.23483	⋯	⋯	3.16291	0.00075	f_2
T Men	2.44004	0.20422	⋯	⋯	3.26706	0.00129	f_1
T Men	2.44004	0.20422	⋯	⋯	3.34985	0.00152	f_1?
T Men	2.44004	0.20422	⋯	⋯	3.55549	0.00571	?
T Men	2.44004	0.20422	⋯	⋯	3.57151	0.00394	?
T Men	2.44004	0.20422	⋯	⋯	3.62582	0.00212	PD?
T Men	2.44004	0.20422	⋯	⋯	3.76914	0.00166	PD?
UZ Scl	2.22648	0.24195	⋯	⋯	5.70046	0.00034	PD?
V354 Aqr	1.89088	0.19434	⋯	⋯	2.54286	0.00321	f_1
V354 Aqr	1.89088	0.19434	⋯	⋯	2.73017	0.00255	?
V354 Aqr	1.89088	0.19434	⋯	⋯	2.82667	0.00332	PD
V360 Aqr	1.60365	0.08866	⋯	⋯	2.14795	0.00061	f_1
V360 Aqr	1.60365	0.08866	⋯	⋯	2.36164	0.00067	PD?
W Tuc	1.55705	0.24128	⋯	⋯	1.06558	0.00043	$f_2 - f_0$?
W Tuc	1.55705	0.24128	⋯	⋯	2.62263	0.00025	f_2
X Ret	2.03226	0.18005	⋯	⋯	2.62522	0.00124	?
X Ret	2.03226	0.18005	⋯	⋯	3.49584	0.00236	f_2
			RRc stars				
AM Tuc	⋯	⋯	2.46442	0.11116	3.89377	0.00142	f_X
AM Tuc	⋯	⋯	2.46442	0.11116	3.97923	0.00220	f_X

Table 11
(Continued)

Name	FM freq. (day^{-1})	FM amp. (mag)	O1 freq. (day^{-1})	O1 amp. (mag)	Signal freq. (day^{-1})	Signal Amp. (mag)	Label
AM Tuc	⋯	⋯	2.46442	0.11116	4.00416	0.00144	f_X
AO Tuc	⋯	⋯	3.00099	0.12680	1.98323	0.00082	?
AO Tuc	⋯	⋯	3.00099	0.12680	2.05689	0.00321	$f_{0.68}$
AO Tuc	⋯	⋯	3.00099	0.12680	3.07186	0.00266	?
ASAS J212331-3025.0	⋯	⋯	2.72156	0.12751	1.90220	0.00174	$f_{0.68}$
ASAS J212331-3025.0	⋯	⋯	2.72156	0.12751	2.42515	0.00324	?
ASAS J212331-3025.0	⋯	⋯	2.72156	0.12751	4.32037	0.00217	f_X
ASAS J212331-3025.0	⋯	⋯	2.72156	0.12751	4.36579	0.00145	f_X
ASAS J212331-3025.0	⋯	⋯	2.72156	0.12751	4.41121	0.00231	f_X
ASAS J213826-3945.0	⋯	⋯	2.43234	0.13015	1.67066	0.00296	$f_{0.68}$
ASAS J213826-3945.0	⋯	⋯	2.43234	0.13015	2.02096	0.00136	$f_X/2$
ASAS J213826-3945.0	⋯	⋯	2.43234	0.13015	3.89461	0.00168	f_X
ASAS J213826-3945.0	⋯	⋯	2.43234	0.13015	3.96108	0.00179	f_X
ASAS J221039-5049.8	⋯	⋯	3.02411	0.16632	2.91198	0.00189	?
ASAS J221039-5049.8	⋯	⋯	3.02411	0.16632	4.95090	0.00058	f_X
ASAS J221039-5049.8	⋯	⋯	3.02411	0.16632	5.02815	0.00052	f_X
ASAS J231412-4648.9	⋯	⋯	3.69174	0.13416	2.90594	0.00075	$f_X/2$?
ASAS J231412-4648.9	⋯	⋯	3.69174	0.13416	3.24932	0.00099	?
ASAS J231412-4648.9	⋯	⋯	3.69174	0.13416	3.29863	0.00064	?
ASAS J231412-4648.9	⋯	⋯	3.69174	0.13416	6.18265	0.00097	f_X
BB Hyi	⋯	⋯	3.48311	0.14277	2.77078	0.00032	$f_X/2$?
BB Hyi	⋯	⋯	3.48311	0.14277	3.10320	0.00035	?
BB Hyi	⋯	⋯	3.48311	0.14277	3.20913	0.00120	?
BB Hyi	⋯	⋯	3.48311	0.14277	3.26210	0.00089	?
BB Hyi	⋯	⋯	3.48311	0.14277	3.29680	0.00044	?
BB Hyi	⋯	⋯	3.48311	0.14277	5.82831	0.00118	f_X
BV Aqr	⋯	⋯	2.74850	0.11754	1.94910	0.00196	?
BV Aqr	⋯	⋯	2.74850	0.11754	2.03533	0.00193	f_0?
BV Aqr	⋯	⋯	2.74850	0.11754	2.32455	0.00103	?
BV Aqr	⋯	⋯	2.74850	0.11754	2.39820	0.00101	?
BV Aqr	⋯	⋯	2.74850	0.11754	4.30599	0.00088	f_X
BV Aqr	⋯	⋯	2.74850	0.11754	4.36707	0.00331	f_X
BV Aqr	⋯	⋯	2.74850	0.11754	4.46407	0.00122	f_X
BV Aqr	⋯	⋯	2.74850	0.11754	4.50539	0.00174	f_X
EP Gru	⋯	⋯	2.70471	0.14067	2.15389	0.00088	$f_X/2$?
EP Gru	⋯	⋯	2.70471	0.14067	2.25090	0.00110	$f_X/2$?
EP Gru	⋯	⋯	2.70471	0.14067	4.38862	0.00307	f_X
EP Gru	⋯	⋯	2.70471	0.14067	4.39401	0.00333	f_X
GDR2 4917277962356593664	⋯	⋯	2.96780	0.12152	4.70307	0.00142	f_X
GDR2 4917277962356593664	⋯	⋯	2.96780	0.12152	4.79225	0.00154	f_X
GDR2 4917277962356593664	⋯	⋯	2.96780	0.12152	4.83102	0.00256	f_X
GDR2 5280964179391935616	⋯	⋯	3.54036	0.14022	5.74705	0.00088	f_X
GDR2 5280964179391935616	⋯	⋯	3.54036	0.14022	5.76676	0.00221	f_X
GDR2 5280964179391935616	⋯	⋯	3.54036	0.14022	5.78647	0.00098	f_X
GDR2 5495625579691991424	⋯	⋯	3.49572	0.14445	2.86914	0.00072	$f_X/2$
GDR2 5495625579691991424	⋯	⋯	3.49572	0.14445	5.85134	0.00096	f_X
GDR2 6379606226611647744	⋯	⋯	3.06420	0.18536	2.34970	0.00057	?
GDR2 6379606226611647744	⋯	⋯	3.06420	0.18536	2.39641	0.00113	$f_X/2$?
GDR2 6379606226611647744	⋯	⋯	3.06420	0.18536	2.60120	0.00059	?
GDR2 6379606226611647744	⋯	⋯	3.06420	0.18536	4.94012	0.00141	f_X
GDR2 6379606226611647744	⋯	⋯	3.06420	0.18536	4.98144	0.00062	f_X
GDR2 6379606226611647744	⋯	⋯	3.06420	0.18536	5.00479	0.00258	f_X
GDR2 6523414998837956736	⋯	⋯	3.12950	0.12727	4.95988	0.00094	f_X
GDR2 6523414998837956736	⋯	⋯	3.12950	0.12727	5.02994	0.00151	f_X
GDR2 6523414998837956736	⋯	⋯	3.12950	0.12727	5.10898	0.00358	f_X
GDR2 6523414998837956736	⋯	⋯	3.12950	0.12727	5.17904	0.00148	f_X
GDR2 6611919706276933376	⋯	⋯	3.43294	0.13651	5.57785	0.00230	f_X
GDR2 6611919706276933376	⋯	⋯	3.43294	0.13651	5.61557	0.00310	f_X
GDR2 6611919706276933376	⋯	⋯	3.43294	0.13651	5.64252	0.00142	f_X
GDR2 6800564393726439552	⋯	⋯	3.31770	0.12836	5.36228	0.00184	f_X
GDR2 6800564393726439552	⋯	⋯	3.31770	0.12836	5.43773	0.00449	f_X
GDR2 6800564393726439552	⋯	⋯	3.31770	0.12836	5.84372	0.00462	?
IY Eri	⋯	⋯	2.66667	0.06993	1.75525	0.00012	$f_{0.68}$
IY Eri	⋯	⋯	2.66667	0.06993	1.82648	0.00036	$f_{0.68}$
IY Eri	⋯	⋯	2.66667	0.06993	4.43288	0.00008	f_X
NSV 1432	⋯	⋯	2.77260	0.09149	2.05297	0.00054	f_0?
NSV 1432	⋯	⋯	2.77260	0.09149	2.31781	0.00045	$f_X/2$?
NSV 1432	⋯	⋯	2.77260	0.09149	2.43470	0.00037	?
NSV 1432	⋯	⋯	2.77260	0.09149	4.42740	0.00039	f_X
NSV 1432	⋯	⋯	2.77260	0.09149	4.47306	0.00135	f_X
NSV 1432	⋯	⋯	2.77260	0.09149	4.51872	0.00073	f_X

Table 11
(Continued)

Name	FM freq. (day^{-1})	FM amp. (mag)	O1 freq. (day^{-1})	O1 amp. (mag)	Signal freq. (day^{-1})	Signal Amp. (mag)	Label
NSV 1432	⋯	⋯	2.77260	0.09149	4.58813	0.00126	f_X
NSVS 14632323	⋯	⋯	2.81490	0.13243	1.91781	0.00194	$f_{0.68}$
NSVS 14632323	⋯	⋯	2.81490	0.13243	4.46575	0.00081	f_X
NSVS 14632323	⋯	⋯	2.81490	0.13243	4.54429	0.00113	f_X
NSVS 14632323	⋯	⋯	2.81490	0.13243	4.57352	0.00177	f_X
NSVS 14632323	⋯	⋯	2.81490	0.13243	4.59726	0.00069	f_X
NSVS 14632323	⋯	⋯	2.81490	0.13243	4.69772	0.00223	f_X
SX Hyi	⋯	⋯	3.21870	0.14832	2.48803	0.00066	$f_X/2$?
SX Hyi	⋯	⋯	3.21870	0.14832	5.18803	0.00122	f_X
SX Hyi	⋯	⋯	3.21870	0.14832	5.22216	0.00378	f_X
SX Hyi	⋯	⋯	3.21870	0.14832	5.26348	0.00197	f_X
SX Hyi	⋯	⋯	3.21870	0.14832	11.03533	0.00120	?
SX Hyi	⋯	⋯	3.21870	0.14832	11.08563	0.00117	?
XX Dor	⋯	⋯	3.04006	0.11268	2.39110	0.00215	$f_X/2$?
XX Dor	⋯	⋯	3.04006	0.11268	2.41246	0.00137	$f_X/2$
XX Dor	⋯	⋯	3.04006	0.11268	2.47745	0.00073	$f_X/2$
XX Dor	⋯	⋯	3.04006	0.11268	2.96617	0.00092	?
XX Dor	⋯	⋯	3.04006	0.11268	3.11573	0.00216	?
XX Dor	⋯	⋯	3.04006	0.11268	4.81246	0.00167	f_X
XX Dor	⋯	⋯	3.04006	0.11268	4.88101	0.00166	f_X
XX Dor	⋯	⋯	3.04006	0.11268	4.95490	0.00531	f_X
XX Dor	⋯	⋯	3.04006	0.11268	4.96736	0.00205	f_X
YZ PsA	⋯	⋯	3.15629	0.11783	4.99940	0.00239	f_X
YZ PsA	⋯	⋯	3.15629	0.11783	5.07665	0.00179	f_X
YZ PsA	⋯	⋯	3.15629	0.11783	5.12515	0.00147	f_X
YZ PsA	⋯	⋯	3.15629	0.11783	5.16647	0.00327	f_X
YZ PsA	⋯	⋯	3.15629	0.11783	5.21318	0.00085	f_X
			RRd stars				
Al Vol	1.93337	0.08256	2.59592	0.12304	4.17240	0.00067	f_X
Al Vol	1.93337	0.08256	2.59592	0.12304	4.22137	0.00182	f_X
CZ Phe	1.76430	0.05464	2.36689	0.11390	3.80208	0.00131	f_X
CZ Phe	1.76430	0.05464	2.36689	0.11390	3.83591	0.00128	f_X
CZ Phe	1.76430	0.05464	2.36689	0.11390	3.86528	0.00140	f_X
GDR2 6529889228241771264	1.84400	0.03362	2.46336	0.08812	3.94272	0.00191	f_X
GDR2 6529889228241771264	1.84400	0.03362	2.46336	0.08812	4.00548	0.00172	f_X
SW Ret	2.09822	0.04560	2.81840	0.10513	4.55519	0.00184	f_X
SW Ret	2.09822	0.04560	2.81840	0.10513	4.57211	0.00591	f_X
SW Ret	2.09822	0.04560	2.81840	0.10513	4.58991	0.00084	f_X
Z Gru	2.04911	0.10360	2.75337	0.11974	4.46407	0.00125	f_X

Note. Labels refer to the type of frequency groups identified in the text.

(This table is available in machine-readable form.)

ORCID iDs

L. Molnár https://orcid.org/0000-0002-8159-1599
A. Bódi https://orcid.org/0000-0002-8585-4544
A. Pál https://orcid.org/0000-0001-5449-2467
A. Bhardwaj https://orcid.org/0000-0001-6147-3360
J. M. Benkő https://orcid.org/0000-0003-3851-6603
A. Derekas https://orcid.org/0000-0002-6526-9444
M. Joyce https://orcid.org/0000-0002-8717-127X
A. Hasanzadeh https://orcid.org/0000-0002-7286-1438
K. Kolenberg https://orcid.org/0000-0001-5181-5072
M. B. Lund https://orcid.org/0000-0003-2527-1598
J. M. Nemec https://orcid.org/0000-0003-1281-5525
H. Netzel https://orcid.org/0000-0001-5608-0028
C. –C. Ngeow https://orcid.org/0000-0001-8771-7554
J. Pepper https://orcid.org/0000-0002-3827-8417
E. Plachy https://orcid.org/0000-0002-5481-3352
Z. Prudil https://orcid.org/0000-0001-5497-5805
R. J. Siverd https://orcid.org/0000-0001-5016-3359
M. Skarka https://orcid.org/0000-0002-7602-0046
R. Smolec https://orcid.org/0000-0001-7217-4884
Á. Sódor https://orcid.org/0000-0001-7806-2883
P. Szabó https://orcid.org/0000-0002-5781-1926
R. Szabó https://orcid.org/0000-0002-3258-1909
H. Kjeldsen https://orcid.org/0000-0002-9037-0018
J. Christensen-Dalsgaard https://orcid.org/0000-0001-5137-0966
G. R. Ricker https://orcid.org/0000-0003-2058-6662

References

Alcock, C., Alves, D. R., Becker, A., et al. 2003, ApJ, 598, 597
Astropy Collaboration, Robitaille, T. P., Tollerud, E. J., et al. 2013, A&A, 558, A33
Astropy Collaboration, Price-Whelan, A. M., SipHocz, B. M., et al. 2018, AJ, 156, 123
Bailer-Jones, C. A. L., Rybizki, J., Fouesneau, M., Demleitner, M., & Andrae, R. 2021, AJ, 161, 147
Bailer-Jones, C. A. L., Rybizki, J., Fouesneau, M., Mantelet, G., & Andrae, R. 2018, AJ, 156, 58
Bailey, S. I. 1902, AnHar, 38, 1

Barentsen, G., Hedges, C., Vinícius, Z., et al. 2019, KeplerGO/lightkurve: Lightkurve v1.0b29, Zenodo, doi:10.5281/zenodo.2565212
Barnes, T. G., III, Guggenberger, E., & Kolenberg, K. 2021, AJ, 162, 117
Beaton, R. L., Freedman, W. L., Madore, B. F., et al. 2016, ApJ, 832, 210
Bedding, T. R., & Kjeldsen, H. 2010, CoAst, 161, 3
Bellinger, E. P., Kanbur, S. M., Bhardwaj, A., & Marconi, M. 2020, MNRAS, 491, 4752
Benkő, J. M., Jurcsik, J., & Derekas, A. 2019, MNRAS, 485, 5897
Benkő, J. M., Plachy, E., Szabó, R., Molnár, L., & Kolláth, Z. 2014, ApJS, 213, 31
Benkő, J. M., & Szabó, R. 2015, ApJL, 809, L19
Benkő, J. M., Szabó, R., Derekas, A., & Sódor, Á. 2016, MNRAS, 463, 1769
Benkő, J. M., Szabó, R., & Paparó, M. 2011, MNRAS, 417, 974
Benkő, J. M., Kolenberg, K., Szabó, R., et al. 2010, MNRAS, 409, 1585
Bennett, M., & Bovy, J. 2019, MNRAS, 482, 1417
Bensby, T., Feltzing, S., & Lundström, I. 2003, A&A, 410, 527
Bernhard, K., & Wils, P. 2006, IBVS, 5698, 1
Bhardwaj, A., Kanbur, S. M., Marconi, M., et al. 2017, MNRAS, 466, 2805
Bhardwaj, A., Kanbur, S. M., Singh, H. P., Macri, L. M., & Ngeow, C.-C. 2015, MNRAS, 447, 3342
Bhardwaj, A., Rejkuba, M., de Grijs, R., et al. 2021, ApJ, 909, 200
Blažko, S. 1907, AN, 175, 325
Bono, G., & Stellingwerf, R. F. 1994, ApJS, 93, 233
Borkovits, T., Rappaport, S. A., Tan, T. G., et al. 2020, MNRAS, 496, 4624
Borucki, W. J. 2016, RPPh, 79, 036901
Bovy, J. 2015, ApJS, 216, 29
Bovy, J., Rix, H.-W., Green, G. M., Schlafly, E. F., & Finkbeiner, D. P. 2016, ApJ, 818, 130
Braga, V. F., Bono, G., Fiorentino, G., et al. 2020, A&A, 644, A95
Braga, V. F., Crestani, J., Fabrizio, M., et al. 2021, ApJ, 919, 85
Brown, D. C. 1971, PgE, 37, 855, https://www.asprs.org/wp-content/uploads/pers/1971journal/aug/1971_aug_855-866.pdf
Buchler, J. R., & Kolláth, Z. 2011, ApJ, 731, 24
Buder, S., Lind, K., Ness, M. K., et al. 2019, A&A, 624, A19
Buder, S., Sharma, S., Kos, J., et al. 2021, MNRAS, 506, 150
Butters, O. W., West, R. G., Anderson, D. R., et al. 2010, A&A, 520, L10
Cacciari, C., Corwin, T. M., & Carney, B. W. 2005, AJ, 129, 267
Carrell, K., Wilhelm, R., Olsen, F., et al. 2021, ApJL, 916, L12
Catelan, M., Pritzl, B. J., & Smith, H. A. 2004, ApJS, 154, 633
Chadid, M., Benkő, J. M., Szabó, R., et al. 2010, A&A, 510, A39
Clementini, G., Ripepi, V., Molinaro, R., et al. 2019, A&A, 622, A60
Coppola, G., Marconi, M., Stetson, P. B., et al. 2015, ApJ, 814, 71
Cox, A. N., King, D. S., & Hodson, S. W. 1980, ApJ, 236, 219
Crestani, J., Braga, V. F., Fabrizio, M., et al. 2021a, ApJ, 914, 10
Crestani, J., Fabrizio, M., Braga, V. F., et al. 2021b, ApJ, 908, 20
Das, S., Bhardwaj, A., Kanbur, S. M., Singh, H. P., & Marconi, M. 2018, MNRAS, 481, 2000
Drake, A. J., Djorgovski, S. G., Catelan, M., et al. 2017, MNRAS, 469, 3688
Duan, X.-W., Chen, X., Sun, W., et al. 2021a, ApJ, 918, 3
Duan, X.-W., Chen, X.-D., Deng, L.-C., et al. 2021b, ApJ, 909, 25
Dziembowski, W. A. 2016, CoKon, 105, 23
Dziembowski, W. A., & Cassisi, S. 1999, AcA, 49, 371
Fabrizio, M., Bono, G., Braga, V. F., et al. 2019, ApJ, 882, 169
Feinstein, A. D., Montet, B. T., Foreman-Mackey, D., et al. 2019, PASP, 131, 094502
Gaia Collaboration, Prusti, T., de Bruijne, J. H. J., et al. 2016, A&A, 595, A1
Gaia Collaboration, Brown, A. G. A., Vallenari, A., et al. 2018a, A&A, 616, A1
Gaia Collaboration, Babusiaux, C., van Leeuwen, F., et al. 2018b, A&A, 616, A10
Gaia Collaboration, Brown, A. G., Vallenari, A., et al. 2021, A&A, 649, A1
Gilligan, C. K., Chaboyer, B., Marengo, M., et al. 2021, MNRAS, 503, 4719
Goldberg, J. A., Bildsten, L., & Paxton, B. 2020, ApJ, 891, 15
Gravity Collaboration, Abuter, R., Amorim, A., et al. 2018, A&A, 615, L15
Gruberbauer, M., Kolenberg, K., Rowe, J. F., et al. 2007, MNRAS, 379, 1498
Guggenberger, E., Kolenberg, K., Chapellier, E., et al. 2011, MNRAS, 415, 1577
Guggenberger, E., Kolenberg, K., Nemec, J. M., et al. 2012, MNRAS, 424, 649
Hajdu, G., Catelan, M., Jurcsik, J., et al. 2015, MNRAS, 449, L113
Hajdu, G., Pietrzyński, G., Jurcsik, J., et al. 2021, ApJ, 915, 50
Hambsch, F. J. 2012, JAVSO, 40, 1003
Helmi, A., Babusiaux, C., Koppelman, H. H., et al. 2018, Natur, 563, 85
Hernitschek, N., Sesar, B., Rix, H.-W., et al. 2017, ApJ, 850, 96
Hernitschek, N., Cohen, J. G., Rix, H.-W., et al. 2019, ApJ, 871, 49
Holl, B., Audard, M., Nienartowicz, K., et al. 2018, A&A, 618, A30
Howell, S. B., Sobeck, C., Haas, M., et al. 2014, PASP, 126, 398
Iorio, G., & Belokurov, V. 2019, MNRAS, 482, 3868
Jerzykiewicz, M. 1995, in ASP Conf. Ser. 78, Astrophysical Applications of Powerful New Databases, ed. S. J. Adelman & W. L. Wiese (San Francisco, CA: ASP), 265
Jordi, C., Gebran, M., Carrasco, J. M., et al. 2010, A&A, 523, A48
Joyce, M. 2021, mjoyceGR/echelle_toggler: echelle toggling program for asteroseismic applications, vv1.0.0, Zenodo, doi:10.5281/zenodo.4427688
Joyce, M., Leung, S.-C., Molnár, L., et al. 2020, ApJ, 902, 63
Jurcsik, J., Smitola, P., Hajdu, G., & Nuspl, J. 2014, ApJL, 797, L3
Jurcsik, J., Sódor, Á., Szeidl, B., et al. 2009, MNRAS, 400, 1006
Jurcsik, J., Smitola, P., Hajdu, G., et al. 2015, ApJS, 219, 25
Kapteyn, J. C. 1890, AN, 125, 165
Karczmarek, P., Wiktorowicz, G., Iłkiewicz, K., et al. 2017, MNRAS, 466, 2842
Kervella, P., Gallenne, A., Evans, N. R., et al. 2019a, A&A, 623, A117
Kervella, P., Gallenne, A., Remage Evans, N., et al. 2019b, A&A, 623, A116
Kolláth, Z. 2018, in The RR Lyrae 2017 Conf. Revival of the Classical Pulsators: from Galactic Structure to Stellar Interior Diagnostics, ed. R. Smolec, K. Kinemuchi, & R. I. Anderson (Niepolomice: Polish Astronomical Society), 137
Kolláth, Z., Buchler, J. R., Szabó, R., & Csubry, Z. 2002, A&A, 385, 932
Kolláth, Z., Molnár, L., & Szabó, R. 2011, MNRAS, 414, 1111
Kovács, G. 2018, A&A, 614, L4
Kurtz, D. W., Bowman, D. M., Ebo, S. J., et al. 2016, MNRAS, 455, 1237
Layden, A. C. 1994, AJ, 108, 1016
Layden, A. C., Tiede, G. P., Chaboyer, B., Bunner, C., & Smitka, M. T. 2019, AJ, 158, 105
Lenz, P., & Breger, M. 2005, CoAst, 146, 53
Li, L. J., Qian, S. B., & Zhu, L. Y. 2018, ApJ, 863, 151
Lindegren, L., Klioner, S. A., Hernández, J., et al. 2021a, A&A, 649, A2
Lindegren, L., Bastian, U., Biermann, M., et al. 2021b, A&A, 649, A4
Liu, G. C., Huang, Y., Zhang, H. W., et al. 2020, ApJS, 247, 68
Liu, T. 1991, PASP, 103, 205
Liška, J., Skarka, M., Mikulášek, Z., Zejda, M., & Chrastina, M. 2016, A&A, 589, A94
Marconi, M., Coppola, G., Bono, G., et al. 2015, ApJ, 808, 50
Marengo, M., Mullen, J. P., Neeley, J. R., et al. 2020, in ASP Conf. Ser. 529, RR Lyrae/Cepheid 2019: Frontiers of Classical Pulsators, ed. K. Kinemuchi et al. (San Francisco, CA: ASP), 139
Merc, J., Kalup, C., Rathour, R. S., Sánchez Arias, J. P., & Beck, P. G. 2021, CoSka, 51, 45
Minniti, D., Alcock, C., Allsman, R. A., et al. 1999, in ASP Conf. Ser. 165, The Third Stromlo Symposium: The Galactic Halo, ed. B. K. Gibson, R. S. Axelrod, & M. E. Putman (San Francisco, CA: ASP), 284
Molnár, L., Joyce, M., & Kiss, L. L. 2019, ApJ, 879, 62
Molnár, L., Kolláth, Z., & Szabó, R. 2012a, MNRAS, 424, 31
Molnár, L., Kolláth, Z., Szabó, R., et al. 2012b, ApJL, 757, L13
Molnár, L., Pál, A., Plachy, E., et al. 2015a, ApJ, 812, 2
Molnár, L., Plachy, E., Juhász, Á. L., & Rimoldini, L. 2018, A&A, 620, A127
Molnár, L., & Szabados, L. 2014, MNRAS, 442, 3222
Molnár, L., Szabó, R., Moskalik, P. A., et al. 2015b, MNRAS, 452, 4283
Molnár, L., Plachy, E., Klagyivik, P., et al. 2017, EPJWC, 160, 04008
Moretti, M. I., Clementini, G., Muraveva, T., et al. 2014, MNRAS, 437, 2702
Moskalik, P., & Kołaczkowski, Z. 2009, MNRAS, 394, 1649
Moskalik, P., Smolec, R., Kolenberg, K., et al. 2015, MNRAS, 447, 2348
Mullen, J. P., Marengo, M., Martínez-Vázquez, C. E., et al. 2021, ApJ, 912, 144
Nagy, Z., Szegedi-Elek, E., Ábrahám, P., et al. 2021, MNRAS, 504, 185
Neeley, J. R., Marengo, M., Freedman, W. L., et al. 2019, MNRAS, 490, 4254
Nemec, J. M., Cohen, J. G., Ripepi, V., et al. 2013, ApJ, 773, 181
Nemec, J. M., & Moskalik, P. 2021, MNRAS, 507, 781
Netzel, H., & Smolec, R. 2019, MNRAS, 487, 5584
Netzel, H., Smolec, R., & Dziembowski, W. 2015a, MNRAS, 451, L25
Netzel, H., Smolec, R., & Moskalik, P. 2015b, MNRAS, 453, 2022
Netzel, H., Smolec, R., Soszyński, I., & Udalski, A. 2018, MNRAS, 480, 1229
Oosterhoff, P. T. 1939, Obs, 62, 104
Pál, A. 2009, PhD thesis, Department of Astronomy, Eötvös Loránd Univ., http://teo.elte.hu/minosites/ertekezes2009/pal_a.pdf
Pál, A. 2012, MNRAS, 421, 1825
Pál, A., Molnár, L., & Kiss, C. 2018, PASP, 130, 114503
Pál, A., Szakáts, R., Kiss, C., et al. 2020, ApJS, 247, 26
Paunzen, E., Kuba, M., West, R. G., & Zejda, M. 2014, IBVS, 6090, 1

Pepper, J., Kuhn, R. B., Siverd, R., James, D., & Stassun, K. 2012, PASP, 124, 230
Pepper, J., Pogge, R. W., DePoy, D. L., et al. 2007, PASP, 119, 923
Pickering, E. C. 1881, Obs, 4, 225
Pickering, E. C. 1901, HarCi, 54, 1
Pietrukowicz, P., Udalski, A., Soszyński, I., et al. 2012, ApJ, 750, 169
Pietrzyński, G., Thompson, I. B., Gieren, W., et al. 2012, Natur, 484, 75
Plachy, E. 2020, in Stars and their Variability Observed from Space, ed. C. Neiner, W. W. Weiss, D. Baade, R. E. Griffin, & C. C. Lovekin (Vienna: University of Vienna), 465
Plachy, E., Klagyivik, P., Molnár, L., Sódor, Á., & Szabó, R. 2017a, EPJWC, 160, 04009
Plachy, E., Klagyivik, P., Molnár, L., & Szabó, R. 2017b, EPJWC, 160, 04010
Plachy, E., Molnár, L., Jurkovic, M. I., et al. 2017c, MNRAS, 465, 173
Plachy, E., Molnár, L., Bódi, A., et al. 2019, ApJS, 244, 32
Plachy, E., Pál, A., Bódi, A., et al. 2021, ApJS, 253, 11
Preston, G. W. 1964, ARA&A, 2, 23
Prudil, Z., Dékány, I., Catelan, M., et al. 2019, MNRAS, 484, 4833
Prudil, Z., Dékány, I., Grebel, E. K., & Kunder, A. 2020, MNRAS, 492, 3408
Prudil, Z., Smolec, R., Skarka, M., & Netzel, H. 2017, MNRAS, 465, 4074
Prudil, Z., Hanke, M., Lemasle, B., et al. 2021, A&A, 648, A78
Ricker, G. R., Winn, J. N., Vanderspek, R., et al. 2015, JATIS, 1, 014003
Riello, M., De Angeli, F., Evans, D. W., et al. 2021, A&A, 649, A3
Ripepi, V., Catanzaro, G., Molnár, L., et al. 2021, A&A, 647, A111
Schlafly, E. F., & Finkbeiner, D. P. 2011, ApJ, 737, 103
Schönrich, R. 2012, MNRAS, 427, 274
Schönrich, R., Binney, J., & Dehnen, W. 2010, MNRAS, 403, 1829
Sesar, B. 2012, AJ, 144, 114
Sesar, B., Hernitschek, N., Mitrović, S., et al. 2017, AJ, 153, 204
Simon, N. R., & Teays, T. J. 1982, ApJ, 261, 586
Skarka, M. 2014, A&A, 562, A90
Skarka, M., Liška, J., Dřevěný, R., et al. 2018, MNRAS, 474, 824
Skarka, M., Prudil, Z., & Jurcsik, J. 2020, MNRAS, 494, 1237
Skowron, D. M., Soszyński, I., Udalski, A., et al. 2016, AcA, 66, 269
Smith, H. J. 1955, AJ, 60, 179
Smolec, R., & Moskalik, P. 2008, AcA, 58, 233
Smolec, R., & Moskalik, P. 2012, MNRAS, 426, 108
Smolec, R., Moskalik, P., Kałużny, J., et al. 2017, MNRAS, 467, 2349
Smolec, R., Prudil, Z., Skarka, M., & Bakowska, K. 2016, MNRAS, 461, 2934
Smolec, R., Soszyński, I., Udalski, A., et al. 2015, MNRAS, 447, 3756
Sneden, C., Preston, G. W., Kollmeier, J. A., et al. 2018, AJ, 155, 45
Sódor, Á., Skarka, M., Liška, J., & Bognár, Z. 2017, MNRAS, 465, L1
Sódor, Á., Jurcsik, J., Szeidl, B., et al. 2011, MNRAS, 411, 1585
Sollima, A., Cassisi, S., Fiorentino, G., & Gratton, R. G. 2014, MNRAS, 444, 1862
Soszynski, I., Udalski, A., Szymanski, M., et al. 2003, AcA, 53, 93
Soszyński, I., Udalski, A., Szymański, M. K., et al. 2015, AcA, 65, 233
Soszyński, I., Smolec, R., Dziembowski, W. A., et al. 2016, MNRAS, 463, 1332
Soszyński, I., Udalski, A., Wrona, M., et al. 2019, AcA, 69, 321
Soszyński, I., Udalski, A., Szymański, M. K., et al. 2020, AcA, 70, 101
Soubiran, C., Jasniewicz, G., Chemin, L., et al. 2018, A&A, 616, A7
Steinmetz, M., Matijevič, G., Enke, H., et al. 2020, AJ, 160, 82
Szabó, R., Kolláth, Z., & Buchler, J. R. 2004, A&A, 425, 627
Szabó, R., Kolláth, Z., Molnár, L., et al. 2010, MNRAS, 409, 1244
Szabó, R., Benkő, J. M., Paparó, M., et al. 2014, A&A, 570, A100
Szabó, Z. M., Kóspál, Á., Ábrahám, P., et al. 2021, ApJ, 917, 80
Szczygieł, D. M., & Fabrycky, D. C. 2007a, MNRAS, 377, 1263
Szczygieł, D. M., & Fabrycky, D. C. 2007b, MNRAS, 377, 1263
Szegedi-Elek, E., Ábrahám, P., Wyrzykowski, Ł., et al. 2020, ApJ, 899, 130
Ulaczyk, K., Szymański, M. K., Udalski, A., et al. 2013, AcA, 63, 159
Wallace, J. J., Hartman, J. D., Bakos, G. Á., & Bhatti, W. 2019 ApJL, 870, L7
Wenger, M., Ochsenbein, F., Egret, D., et al. 2000, A&AS, 143, 9
Wils, P. 2006, IBVS, 5685, 1
Wils, P., & Otero, S. A. 2005, IBVS, 5593, 1
Woltjer, L. 1956, BAN, 13, 62
Zhou, Y., Nordlander, T., Casagrande, L., et al. 2021, MNRAS, 503, 13